

# **EFFECT OF $\text{Eu}^{3+}$ IONS CONTENT ON PHYSICAL PROPERTIES OF NANOCRYSTALLINE $\text{ZnO}$ AND $\text{Gd}_2\text{O}_3$**

by

**Segundo Rosalí Jáuregui Rosas**

A thesis submitted in partial fulfillment of the requirements for the degree of

MASTER OF SCIENCE

in

Physics

UNIVERSITY OF PUERTO RICO

MAYAGÜEZ CAMPUS

2008

Approved by:

\_\_\_\_\_  
Héctor Jiménez González, PhD  
Member, Graduate Committee

\_\_\_\_\_  
Date

\_\_\_\_\_  
Henri Radovan, PhD  
Member, Graduate Committee

\_\_\_\_\_  
Date

\_\_\_\_\_  
Maharaj S. Tomar, PhD  
Member, Graduate Committee

\_\_\_\_\_  
Date

\_\_\_\_\_  
Oscar J. Perales Pérez, PhD  
President, Graduate Committee

\_\_\_\_\_  
Date

\_\_\_\_\_  
Paul A. Sundaram, PhD  
Representative of Graduate Studies

\_\_\_\_\_  
Date

\_\_\_\_\_  
Héctor Jiménez González, PhD  
Chairperson of the Department

\_\_\_\_\_  
Date

## ABSTRACT

*This work reports a systematic investigation on the effect of  $\text{Eu}^{3+}$  ions on structural and physical properties of nanocrystalline ZnO (nanopowders-NPs and nanocrystals-NCs) and  $\text{Gd}_2\text{O}_3$  (NPs and thin films), which were obtained from starting solutions containing Eu(III) species. NPs were synthesized by Sol-Gel method, using 2-ethylhexanoic acid as solvent; NCs were produced through a modified ethanol-based approach at room temperature, whereas thin films were grown by Sol-Gel method and spin coating process, with acetic acid as solvent. No chelating agent was used. In ZnO NPs, XRD and infrared analysis verified the development of the wurtzite structure without any secondary phase. No significant change in the lattice parameters, as could be expected from  $\text{Eu}^{3+}$  incorporation, was observed. Main differences between NPs and NCs ZnO came out from their Photoluminescence (PL) behavior. NPs showed a weak red emission (which could be attributed to a direct excitation of the  $\text{Eu}^{3+}$  ions, but not to energy transference from the ZnO), but not visible emission under high energy excitation above the band-gap energy of ZnO (which would indicate that free-defects structures were obtained). In turn, both visible broad band and UV emission were observed for NCs. For the same NCs, in addition to an inhibiting growth effect and a blue shift of band gap, an enhancement of the visible/UV emission ratio with the increase in the content of  $\text{Eu}^{3+}$  ions in starting solutions was observed. The generation of defects on the surface of NCs could explain this behavior. Moreover, several lines from  $\text{Eu}^{3+}$  were detected in the PL spectra of NCs only when the excitation energy was between that broad band for ZnO and that intra-4f transition energy of  $\text{Eu}^{3+}$  ions. This feature would suggest no energy transfer from ZnO host to  $\text{Eu}^{3+}$  ions, which would be adsorbed at the surface of NCs instead. In  $\text{Gd}_2\text{O}_3$  NPs, the effects of the annealing temperature have also been systematically investigated. XRD analysis showed that pure and highly crystalline cubic- $\text{Gd}_2\text{O}_3$  host structure was obtained when the precursors, bearing different contents of  $\text{Eu}^{3+}$  species (from 0.01 to 0.30) were annealed at different temperatures in air. The average crystallite size ranged between 29nm and 41nm when the annealing temperature varied from 750°C to 950°C, respectively. The levels of  $\text{Eu}^{3+}$  concentration in the host did not affect the corresponding crystallite sizes. PL spectra of  $\text{Eu}^{3+}$ -doped  $\text{Gd}_2\text{O}_3$  NPs showed all transitions of  $\text{Eu}^{3+}$ , being the  ${}^5\text{D}_0 \rightarrow {}^7\text{F}_2$  transition the most intense. On a common sample-weight basis, it was found that the PL intensity was strongly dependent on both, the annealing temperature and the  $\text{Eu}^{3+}$  content. The highest PL intensity was obtained in NPs annealed at 950°C with 'x' = 0.15 (7.5% w/w of Eu). Unlike to ZnO case, the energy transfer from  $\text{Gd}_2\text{O}_3$  host to  $\text{Eu}^{3+}$  was clearly verified for all evaluated 'x' values, which confirm the actual incorporation of  $\text{Eu}^{3+}$  into the  $\text{Gd}_2\text{O}_3$  lattice. From M-H measurements a paramagnetic behavior between -5000 and 5000Oe at room temperature was observed for  $\text{Eu}^{3+}$ -doped  $\text{Gd}_2\text{O}_3$  NPs, whose magnetic susceptibility decreases as the  $\text{Eu}^{3+}$  content increases. In turn, XRD showed that  $\text{Gd}_{2-x}\text{Eu}_x\text{O}_3$ , thin films with preferential orientation along (400) plane of cubic phase, were obtained. Thin films showed high transparency in the visible region, and their band gap practically was not affected for the  $\text{Eu}^{3+}$  content. Also, unlike to NPs, the more efficient excitation to obtain red luminescence was that corresponding to the absorption band of the host  $\text{Gd}_2\text{O}_3$  (229nm) for all  $\text{Eu}^{3+}$  contents.*

## RESUMEN

*Este trabajo reporta la investigación sistemática del efecto de iones  $\text{Eu}^{3+}$  en las propiedades estructurales y físicas de  $\text{ZnO}$  (nanopolvos-NPs y nanocristales-NCs) y  $\text{Gd}_2\text{O}_3$  (NPs y películas delgadas), obtenidos a partir de soluciones precursoras con diferentes contenidos de  $\text{Eu(III)}$ . Los NPs fueron sintetizados por Sol-Gel, usando 2-ethylhexanoic como solvente, los NCs fueron producidos a través del método modificado Sol-Gel basado en etanol, a temperatura ambiente, mientras que las películas delgadas fueron sintetizados por el método Sol-Gel/spin coating. No se usó agentes gelantes. En nanopulvos de  $\text{ZnO}$ , XRD y análisis de infrarrojo verificaron el desarrollo de la estructura wurtzita sin fases secundarias. No observándose cambio significativo en los parámetros de red, como podría esperarse debido a la incorporación del  $\text{Eu}^{3+}$ . Las diferencias principales entre NPs y NCs de  $\text{ZnO}$  están en su comportamiento en fotoluminiscencia (PL). Los NPs, bajo excitación de alta energía, mayor a la de la banda prohibida de  $\text{ZnO}$ , mostraron una emisión roja débil (que podría ser atribuida a una excitación directa de los iones  $\text{Eu}^{3+}$ , pero no a la transferencia de energía desde el  $\text{ZnO}$ ), pero no emisión visible, lo cual indicaría que las estructuras obtenidas son libres de defectos. A su vez, tanto la emisión visible y la emisión UV fueron observadas en los NCs. Para los mismos NCs, además de un efecto inhibitor de crecimiento y un corrimiento al azul de la banda prohibida, se observó un aumento de la razón emisión visible/UV con el incremento en el contenido de iones  $\text{Eu}^{3+}$  en las soluciones iniciales. La generación de defectos en la superficie de NCs podría explicar este comportamiento. Además, varias líneas de  $\text{Eu}^{3+}$  fueron detectadas en los espectros PL de NCs sólo cuando la energía de excitación estaba entre la correspondiente a banda visible del  $\text{ZnO}$  y la de transición intra-4f de iones  $\text{Eu}^{3+}$ . Esto sugeriría la no transferencia de energía desde el  $\text{ZnO}$  a los iones  $\text{Eu}^{3+}$ , los cuales estarían adsorbidos en la superficie de los NCs.*

*En los nanopulvos de  $\text{Gd}_{2-x}\text{Eu}_x\text{O}_3$ , además del efecto de la concentración de  $\text{Eu}^{3+}$ , también fue investigado el efecto de la temperatura de recocido. Mediante XRD se demostró que los NPs presentan estructura cúbica pura, y altamente cristalina correspondiente al  $\text{Gd}_2\text{O}_3$ , cuando los precursores, con diferentes contenidos de  $\text{Eu}^{3+}$  (desde 0.01 hasta 0.30), fueron recocidos a diferentes temperaturas en aire. El tamaño promedio del cristalito osciló entre 29nm y 41nm cuando la temperatura de recocido varió desde 750°C hasta 950°C, respectivamente. No se apreció un efecto del contenido de  $\text{Eu}^{3+}$ . Los espectros PL de los NPs de  $\text{Gd}_{2-x}\text{Eu}_x\text{O}_3$  mostraron todas las transiciones de  $\text{Eu}^{3+}$ , siendo la transición  ${}^5\text{D}_0 \rightarrow {}^7\text{F}_2$  la más intensa. Se observó que la intensidad PL es fuertemente dependiente de la temperatura de recocido y el contenido  $\text{Eu}^{3+}$ . La intensidad más alta fue obtenida en NPs recocidos a 950°C con  $x = 0.15$  (7.5%w/w de Eu). A diferencia de lo obtenido en  $\text{ZnO}$ , la transferencia de energía del  $\text{Gd}_2\text{O}_3$  al  $\text{Eu}^{3+}$  fue claramente verificado para todo 'x' evaluado, lo cual confirma la incorporación de  $\text{Eu}^{3+}$  en la red del  $\text{Gd}_2\text{O}_3$ . A partir de medidas M-H, entre -5000 y 5000Oe, a temperatura ambiente, se observó un comportamiento paramagnético de los NPs de  $\text{Gd}_{2-x}\text{Eu}_x\text{O}_3$ , cuya susceptibilidad magnética disminuyó cuando aumentó el contenido de  $\text{Eu}^{3+}$ . A su vez, XRD mostró que las películas delgadas de  $\text{Gd}_{2-x}\text{Eu}_x\text{O}_3$  presentan orientación preferencial a lo largo del plano (400) de la fase cúbica. Las películas mostraron alta transparencia en la región visible, y su banda prohibida prácticamente no fue afectada por el contenido de  $\text{Eu}^{3+}$ . Asimismo, a diferencia de los NPs, la excitación más eficiente para obtener luminiscencia roja fue la correspondiente a la banda de absorción del  $\text{Gd}_2\text{O}_3$  (229nm) para todos los contenidos de  $\text{Eu}^{3+}$ .*

**Copyright © 2008**  
**By**  
**Segundo R. Jáuregui Rosas**

## DEDICATORY

*To God, for his infinite love and protection.*

*To my parents Maria and Leoncio, and my  
brothers Domitila, Dolores, Antonio, Benito and  
Dalila, and all my “Tribu” for their unconditional  
support, sacrifice, inspiration and love.*

*To Yoli, for all that she signify*

## ACKNOWLEDGEMENTS

Many persons and institutions collaborated directly and indirectly with my research. Without their support it would be impossible for me to finish my work. I would like to express my sincere gratitude to:

- Dr. Oscar Perales for his scientific advice, guidance and friendship.
- Dr. Henri Radovan, for the opportunity to initiate my work in his laboratory. Also I am grateful for his interesting comments and suggestions.
- Dr. Hector Jiménez, for his valuable teachings, transmitted knowledge for the completion of my work.
- Dr. Maharaj Tomar, for his important comments and suggestions, the transmitted knowledge for the completion of my work and the opportunity to work in his laboratory and his constant worry for the development of this work.
- Mr. Omar Vázquez, who help me with Photoluminescence measurements, his constant technical support in the laboratory, and his valuable friendship.
- Dr. Weiyi Jia, for his support, guidance, transmitted knowledge and his interesting comments about Luminescence phenomena.
- Dr. Samuel Hernández and MS. Leonardo Pacheco (Chemistry Department), for their valuable help with Raman measurements.
- Dr. Ricardo Melgarejo (UPR-Rio Piedras Campus) for his important help with Profilometry measurements and valuable suggestions about experimental process.
- Dr. Esteban Fachini (UPR-Rio Piedras Campus) for his important help with SEM-EDS measurements.
- Miss Yarilin Cedeño, for her valuable help with M-H measurements.
- Mr. Alfredo Moreu, for his valuable and opportune technical support, as well as his sincere friendship.
- Mrs. Waleska Cruz, Mrs. Vanessa Gonzalez, Mrs. Liliam Lorenzo, and Mrs. Virginia Figueroa, administrative personal of Physics Department, for their constant and valuable support and friendship.
- All graduate students of Physics Department, for their friendship and constant support.
- All my friends of the Departamento de Física of the Universidad Nacional de Trujillo-Perú, for their permanent and valuable support during my studies.
- Finally, but no less important I'd like thanks to NSF-PREM: Synergistic Research and Education on Functional Nanostructured Materials and The NANOMaterials Processing Laboratory Department of Engineering Science and Materials, UPRM

Definitely, I can't finish my program without them!! This thesis is dedicated to them.

# Table of Contents

<b>Content</b>	<b>Page</b>
<b>ABSTRACT</b>	ii
<b>RESUMEN</b>	iii
<b>DEDICATORY</b>	v
<b>ACKNOWLEDGEMENTS</b>	vi
<b>TABLE OF CONTENTS</b>	vii
<b>TABLE LIST</b>	x
<b>FIGURE LIST</b>	xi
<b>CHAPTER I: INTRODUCTION</b>	1
1.1 Motivation	1
1.2 Aim of study	5
1.2.1 Main objective	5
1.2.2 Specific objectives	5
1.3 Summary of following chapters	7
<b>CHAPTER II: THEORETICAL BACKGROUND</b>	8
2.1 Luminescence and phosphor materials	8
2.1.1 Mechanisms	9
2.1.2 Hosts and activators	9
2.2 Zinc Oxide Properties	10
2.2.1 Crystal structure of Zinc Oxide	11
2.2.2 Electronic band structure of ZnO	13
2.2.3 Luminescence of ZnO	14
2.3 Triply-ionized Rare Earths	21
2.3.1 General properties	21
2.3.2 Incorporation of Rare Earth ions into solid lattices	24
2.3.3 Rare Earth ions as optical dopants	26
2.3.4 Luminescence of Rare Earth ions in host solid compounds	27
2.3.5 Energy transfer	29

2.3.6 Concentration quenching	30
2.3.7 Charge transfer band (CTB)	31
2.4 Gd <sub>2</sub> O <sub>3</sub> Properties	33
2.4.1 Crystal structure	34
2.4.2 Quantum effects in Rare Earth-doped nanostructures	36
<b>CHAPTER III: PREVIOUS RELATED WORKS</b>	<b>37</b>
3.1 Introduction	37
3.2 The Eu <sup>3+</sup> - ZnO System	39
3.2 The Eu <sup>3+</sup> - Gd <sub>2</sub> O <sub>3</sub> System	46
<b>CHAPTER IV: EXPERIMENTAL DETAILS</b>	<b>54</b>
4.1 Synthesis of nanocrystalline ZnO in presence of Eu <sup>3+</sup> ions	54
4.1.1 The Sol-Gel approach	54
4.1.2 The Ethanol route	54
4.2 Synthesis of nanostructured Eu-doped Gd <sub>2</sub> O <sub>3</sub>	56
4.2.1 Synthesis of Eu-doped Gd <sub>2</sub> O <sub>3</sub> nanocrystalline powder	57
4.2.2 Growth of nanocrystalline Eu-doped Gd <sub>2</sub> O <sub>3</sub> Thin Films	58
4.3 Characterization of the nanostructures	60
4.3.1 X-Ray Diffraction	61
4.3.2 Absorption Spectroscopy	63
4.3.3 Photoluminescence Spectroscopy	65
4.3.3.1 Fundamentals	65
4.3.3.2 Optimization of measurements	67
<b>CHAPTER V: RESULTS AND DISCUSSION</b>	<b>70</b>
5.1 Eu <sup>3+</sup> -containing ZnO	70
5.1.1 Nanopowders	70
5.1.1.1 Thermal analysis of precursor salts	70
5.1.1.2 Structural characterization	71
5.1.1.3 Infrared analysis	76
5.1.1.4 Raman measurements	77
5.1.1.5 Photoluminescence measurements	79
5.1.2 Nanocrystals	85
5.1.2.1 Structural characterization	85
5.1.2.2 Infrared analysis	89
5.1.2.3 Raman measurements	90
5.1.2.4 UV-vis measurements	91
5.1.2.5 Photoluminescence measurements	96

5.2 Eu-doped Gd <sub>2</sub> O <sub>3</sub>	105
5.2.1 Nanopowders	105
5.2.1.1 Thermal analysis of precursors and intermediate	105
5.2.1.2 Structural characterization	106
5.2.1.3 Infrared analysis	110
5.2.1.4 Raman measurements	111
5.2.1.5 Elemental analysis	113
5.2.1.6 Photoluminescence measurements	114
5.2.1.7 Preliminary magnetic characterization	121
5.2.2 Properties of Eu-doped Gd <sub>2</sub> O <sub>3</sub> Thin Films	123
5.2.2.1 Structural and morphological characterization	124
5.2.2.2 Optical properties	126
5.2.2.3 Photoluminescence measurements	128
<b>CHAPTER VI: CONCLUSIONS AND SUGGESTIONS</b>	<b>132</b>
<b>REFERENCES</b>	<b>136</b>

## Table List

<b>Tables</b>	<b>Page</b>
Table 2.1 Filling of 4f shells of trivalent ions RE according to Hund's rules.	22
Table 5.1 Variation of lattice parameter of $\text{Eu}^{3+}$ -doped $\text{Gd}_2\text{O}_3$ nanoparticles, annealed at different temperatures.	113
Table 5.2 Mutual interaction constant ( $s$ ) for $\text{Gd}_{2-x}\text{Eu}_x\text{O}_3$ nanocrystalline powders annealed for 2 hours at different temperatures. The values were obtained from slope of plots shown in figure 5.47.	120
Table 5.3 Magnetic susceptibility, at room temperature, of $\text{Gd}_{2-x}\text{Eu}_x\text{O}_3$ powders, annealed at $950^\circ\text{C}$ .	127

## Figure List

<b>Figures</b>		<b>Page</b>
Figure 2.1	ZnO crystal structures: (a) rocksalt (B1), (b) zinc blende (B3) and (c) wurtzite (B4).	11
Figure 2.2	(a) Wurtzite crystal structure of ZnO with the regular hexagonal unit cell overlaid in orange. ZnO preferentially terminates on a polar face along the c-axis, O-polar termination is shown. (b) a single O atom surrounded by Zn atoms at the edges of a regular tetrahedron.	12
Figure 2.3	(a) Bulk band structure of ZnO for various high-symmetry lines in the irreducible part (see inset) of the bulk Brillouin zone and density of states. The full line shows the total density of states and the dotted line gives the cation contribution to the DOS; (b) Splitting of the VB in hexagonal ZnO under the influence of crystal field and spin-orbit coupling. (The figure is not drawn to scale).	13
Figure 2.4	Schematic electronic level diagram of ZnO. The non-radiative transitions (black arrows), possible red emission (red arrows), and green emission (green arrow) are shown.	16
Figure 2.5	EPR (a) and Photoluminescence (b) spectra measured at room temperature from ZnO structures using different methods. EPR spectra have been vertically shifted for clarity. The inset in (b) shows the PL from the sample fabricated by a chemical method at 4 K.	18
Figure 2.6	PL spectra for the as-received ZnO nanoparticles and those annealed in air, O <sub>2</sub> , and Ar atmospheres at 900°C for 1 h. The excitation wavelength was 325nm.	19
Figure 2.7	Variable temperature PL spectra (defect emission) of different ZnO nanostructures excited at 325 and 390 nm: (a), (b) shells, ((c), (d)) rods and ((e), (f)) needles.	20
Figure 2.8	Effective ionic radius ( $\text{\AA}$ ) for some common cations (CN: coordination number).	23

Figure 2.9	Interactions leading to the different electronic energy levels for the [Xe] 4f <sup>6</sup> 5d <sup>0</sup> configuration of Eu <sup>3+</sup> (six electrons in the 4f orbitals).	25
Figure 2.10	Energy level diagram of the optical transitions within Eu <sup>3+</sup> ions.	29
Figure 2.11	Schematic illustration of a configurational coordinate model. The two curves are modified by repulsion near the intersection (broken lines). The vertical broken lines A ↔ B and C ↔ D indicate the absorption and emission of light, respectively (left), and coordinate diagram with the <sup>7</sup> F <sub>J</sub> ground states (J = 1-6, levels with J = 2-5 are not shown), the <sup>5</sup> D <sub>J</sub> excited states (J = 0-2 are shown), and the charge transfer state of Eu <sup>3+</sup> (right)	32
Figure 2.12	Polyhedral representations of the cubic C-type (cubic), B-type (monoclinic) and A-type (hexagonal) structure of RE <sub>2</sub> O <sub>3</sub> . The large and small spheres stand for RE and O atoms, respectively.	34
Figure 2.13	Structure of RE <sub>2</sub> O <sub>3</sub> related to the atomic number and to the temperature, at room pressure. In general three structures can be stable at T < 800°C: A-hexagonal, B-monoclinic, C-cubic.	35
Figure 2.14	The two cation sites of cubic bixbyite. (a) 8b (S <sub>6</sub> or C <sub>3i</sub> symmetry) and (b) 24d (C <sub>2</sub> symmetry).	35
Figure 3.1	A schematic presentation of the RE <sup>3+</sup> coordination in the C <sub>2</sub> and S <sub>6</sub> sites of cubic (C-type) sesquioxide.	38
Figure 3.2	a) Excitation spectra of ZnO:Eu 0.1 and 3 at% monitored at 612 and 616 nm, respectively, and b) Photoluminescence spectra of ZnO:Eu 3at% obtained at different excitation wavelengths at room temperature.	40
Figure 3.3	XRD patterns of ZnO:Eu nanopowders with different Eu <sup>3+</sup> -doping concentrations. A It can be seen that the peaks in the pattern sample with 1mol% Eu <sup>3+</sup> shifts to large angle, compared to 0.5mol%.	42
Figure 3.4	Excitation spectra of ZnO:Eu nanopowders under monitoring wavelength at (a) 708nm and (b) 616nm	41
Figure 3.5	PL spectra of ZnO:Eu nanorods at 15K. In spectrum (a) the band around 650nm was assigned to ZnO emission, whereas in spectra (b) and (c) the sharp peaks due to 4f-transitions from Eu <sup>3+</sup> ions, were clearly observed.	43

Figure 3.6	(a) PL spectra of ZnO:Eu nanorods at different excitation wavelengths at 15 K. (b) Excitation energy dependence of the $\text{Eu}^{3+}$ -related PL intensity in ZnO:Eu nanorods.	43
Figure 3.7	Excitation spectra of $\text{Eu}^{3+}$ :ZnO nanocrystals by monitoring the ${}^5\text{D}_0 \rightarrow {}^7\text{F}_2$ emission at 10 K, with (a) $\lambda_{\text{mon}}=615.4$ nm for the as-grown sample, and (b) $\lambda_{\text{mon}}=616.6$ nm for the annealed sample.	45
Figure 3.8	Excitation (a) and emission (b) spectra of samples calcined at different temperatures.	49
Figure 3.9	(a) Emission (excitation at 254nm) and (b) excitation (monitoring 611nm) spectra of $\text{Gd}_2\text{O}_3:\text{Eu}^{3+}$ phosphors having different concentrations.	50
Figure 3.10	Excitation (a) and emission (b) spectra of $\text{Gd}_2\text{O}_3:\text{Eu}$ particles at different doping concentrations, prepared at 900°C.	53
Figure 4.1	Flow diagram of the sol-gel process for synthesis of $\text{Zn}_{1-x}\text{O}:\text{Eu}_x$ nanopowders.	55
Figure 4.2	Flow diagram of the modified sol-gel method (ethanol route) of $\text{Zn}_{1-x}\text{O}:\text{Eu}_x$ nanocrystals.	56
Figure 4.3	Experimental procedure for the synthesis of $\text{Gd}_{2-x}\text{Eu}_x\text{O}_3$ nanocrystalline powders.	58
Figure 4.4	Flow diagram of the sol-gel spin coating of $\text{Gd}_{2-x}\text{Eu}_x\text{O}_3$ thin films.	59
Figure 4.5	Schematic diagram of Bragg's diffraction from a set of parallel planes.	62
Figure 4.6	Simplify Structure of the Spectrofluorometer Fluoromax 2.	67
Figure 4.7	Detailed Emission spectrum of the 150mW continuous ozone-free Xe lamp, of the Spectrofluorometer FluoroMax-2, used for photoluminescence measurements. The whole spectrum is shown inset.	68
Figure 4.8	Effect of Slit and collect mode of the spectrometer on the excitation spectra at low wavelength region. A sample of $\text{Eu}^{3+}$ -doped $\text{Gd}_2\text{O}_3$ ( $x=0.05$ ) was used, but similar effects were observed for other cases.	69

Figure 5.1	TGA profiles for Zn(II) and Eu(III) acetate salts. Different transformation temperatures are shown.	70
Figure 5.2	XRD patterns of nanopowders of ZnO, synthesized by sol-gel method, with different contents of Eu <sup>3+</sup> ions.	72
Figure 5.3	Variation of lattice parameters of ZnO nanopowders with Eu <sup>3+</sup> ions content, 'x'. The solid line is only for visual guide.	72
Figure 5.4	Variation of the average crystallite size of Zn <sub>1-x</sub> O:Eu <sub>x</sub> nanopowders as function of Eu <sup>3+</sup> content. In general, the presence of Eu <sup>3+</sup> ions leads to larger crystallite than pure ZnO. The solid line is only for visual guide.	73
Figure 5.5	XRD patterns of Zn(II) and Eu(III) acetates, after dissolving and drying at the same conditions used for synthesis of nanopowders.	74
Figure 5.6	XRD patterns of nanopowders of ZnO containing Eu <sup>3+</sup> ions and annealed at different temperatures.	75
Figure 5.7	FT-IR spectra of ZnO pure and containing Eu <sup>3+</sup> ions.	76
Figure 5.8	FT-IR spectra of ZnO containing Eu <sup>3+</sup> ions (x=0.08) annealed at different temperatures.	77
Figure 5.9	Raman spectra of ZnO nanopowders as synthesized (A.S.) and annealed at 650°C for 1 hour in air. The enhancement of crystallinity after annealing is evident, confirming the XRD results.	78
Figure 5.10	Raman spectra of ZnO nanopowders (a) without Eu <sup>3+</sup> (as synthesized), (b) containing Eu <sup>3+</sup> (x=0.05) as synthesized and (c) the same of (b) but annealed at 450°C for 1 hour in air.	79
Figure 5.11	(a) Emission spectra, at room temperature, of bare and containing Eu <sup>3+</sup> ions ZnO nanopowders synthesized in this work. No visible emission, related to ZnO defects, was observed. (b) Emission from ZnO nanowires on a silicon substrate reported in [76].	80
Figure 5.12	Effect of washing and annealing on emission spectra, at room temperature, of ZnO nanopowders. Similar to in synthesized (A.S.), no visible emission related to ZnO defects, was observed.	81

Figure 5.13	Emission spectra, at room temperature, of ZnO powders synthesized with different contents of $\text{Eu}^{3+}$ .	82
Figure 5.14	Emission spectra of ZnO nanopowders, containing 0.08% $\text{Eu}^{3+}$ (w/w), as synthesized and annealed at different temperatures, and using different excitation wavelength: (a) 350nm, (b) 393nm and (c) 464nm.	83
Figure 5.15	XRD patterns of $\text{Zn}_{1-x}\text{O}:\text{Eu}_x$ nanocrystals, no aged, with different contents of $\text{Eu}^{3+}$ ions.	86
Figure 5.16	Effect of $\text{Eu}^{3+}$ ions content on the lattice parameters of ZnO nanocrystals no aged.	86
Figure 5.17	Effect of $\text{Eu}^{3+}$ ions content on average crystallite size of ZnO nanocrystals no aged.	87
Figure 5.18	XRD patterns of ZnO nanocrystals aged for different times.	88
Figure 5.19	XRD patterns of $\text{Eu}^{3+}$ -containing ZnO nanocrystals ( $x=0.30$ ) and aged for different times.	88
Figure 5.20	FT-IR spectra of $\text{Eu}^{3+}$ -containing ZnO nanocrystals, which were not aged.	89
Figure 5.21	FT-IR spectra of (a) bare and (b) with $\text{Eu}^{3+}$ ions ( $x=0.30$ ) ZnO nanocrystals aged for different times.	90
Figure 5.22	Raman spectra of bare and $\text{Eu}^{3+}$ -containing ZnO nanocrystals no aged.	91
Figure 5.23	Absorption spectra of suspensions of bare and with $\text{Eu}^{3+}$ ions ZnO nanocrystals no aged.	92
Figure 5.24	Absorption spectra of suspensions of bare and with $\text{Eu}^{3+}$ ions ZnO nanocrystals no aged. The variation of band-gap is shown inset.	93
Figure 5.25	(a) Energy gap of $\text{Zn}_{1-x}\text{O}:\text{Eu}_x$ nanocrystals no aged, as function on $\text{Eu}^{3+}$ ions content, and (b) their position as respect to that of bulk ZnO and $\text{Eu}_2\text{O}_3$ .	93
Figure 5.26	UV-vis absorption spectra of bare (top) and $\text{Eu}^{3+}$ -ions containing (center and below) ZnO aged for different times.	94

Figure 5.27	Effect of aging time and europium content on the band gap of ZnO nanocrystals.	95
Figure 5.28	Emission spectra, at room temperature, of ZnO nanocrystals with different contents of $\text{Eu}^{3+}$ ions.	97
Figure 5.29	Effect of $\text{Eu}^{3+}$ ions content on visible to UV emission ratio (vis/UV) and visible emission peak of $\text{Zn}_{1-x}\text{O}:\text{Eu}_x$ nanocrystals. Excitation radiation was 350nm.	97
Figure 5.30	Room temperature excitation spectra of no aged $\text{Zn}_{1-x}\text{O}:\text{Eu}_x$ ( $x=0.15$ ) nanocrystals.	99
Figure 5.31	Room temperature excitation spectra of no aged $\text{Zn}_{1-x}\text{O}:\text{Eu}_x$ ( $x=0.15$ ) nanocrystals, monitored under different wavelength excitation.	100
Figure 5.32	(a) Excitation and (b) emission spectra, at room temperature, of $\text{Zn}_{1-x}\text{O}:\text{Eu}_x$ ( $x=0.30$ ) ZnO nanocrystals no aged, under different wavelength excitation.	101
Figure 5.33	Emission spectra, at room temperature, of $\text{Zn}_{1-x}\text{O}:\text{Eu}_x$ ( $x=0.15$ ) nanocrystals no aged, using different wavelength excitation.	103
Figure 5.34	a) TGA profiles for Gd(III) and Eu(III) acetate salts; b) TGA-DTA profiles of $\text{Gd}_{2-x}\text{Eu}_x\text{O}_3$ ( $x=0.08$ ) intermediate.	106
Figure 5.35	XRD patterns of pure $\text{Gd}_2\text{O}_3$ and $\text{Gd}_{2-x}\text{Eu}_x\text{O}_3$ ( $x=0.05$ ) before (a) and after annealing at (b) $750^\circ\text{C}$ , (c) $850^\circ\text{C}$ , and (d) $950^\circ\text{C}$ for 2h. All peaks correspond to cubic $\text{Gd}_2\text{O}_3$ phase.	108
Figure 5.36	XRD patterns of $\text{Gd}_{2-x}\text{Eu}_x\text{O}_3$ powders synthesized at different atomic fractions of Eu ions, 'x'. The solids were crystallized after annealing in air at $750^\circ\text{C}$ for 2h. All peaks correspond to cubic $\text{Gd}_2\text{O}_3$ host structure.	108
Figure 5.37	Effect of annealing and $\text{Eu}^{3+}$ content, 'x', on the average crystallite size of $\text{Gd}_{2-x}\text{Eu}_x\text{O}_3$ nanocrystalline powders. The continuous lines only are as visual help.	109
Figure 5.38	Effect $\text{Eu}^{3+}$ ions content on lattice parameter of $\text{Gd}_{2-x}\text{Eu}_x\text{O}_3$ nanopowders annealed at different temperatures.	109

Figure 5.39	FT-IR spectra of Eu <sup>3+</sup> -doped Gd <sub>2</sub> O <sub>3</sub> precursor and annealed phosphor. Acetates group (1535cm <sup>-1</sup> and 1419cm <sup>-1</sup> ) and metal-O bond (540cm <sup>-1</sup> ) bands are clearly identified.	110
Figure 5.40	Raman spectra of bare and containing Eu <sup>3+</sup> ions (x = 0.15) Gd <sub>2</sub> O <sub>3</sub> annealed at 950°C. The shift of the F <sub>g</sub> band is shown inset.	112
Figure 5.41	Raman spectra of Gd <sub>2-x</sub> Eu <sub>x</sub> O <sub>3</sub> nanocrystalline powders, with x=0.15 annealed at different temperatures.	112
Figure 5.42	EDS spectrum for nanocrystalline Eu-doped Gd <sub>2</sub> O <sub>3</sub> powders, x=0.30, annealed at 950°C.	113
Figure 5.43	Excitation spectra of Gd <sub>2-x</sub> Eu <sub>x</sub> O <sub>3</sub> nanocrystalline powders, x=0.15, for different annealing temperatures. The spectra were taken monitoring the 611nm emission line.	114
Figure 5.44	Excitation spectra of Gd <sub>2-x</sub> Eu <sub>x</sub> O <sub>3</sub> nanocrystalline powders annealed at 750°C for different Eu contents, 'x'. The spectra were taken monitoring the 611nm emission line.	115
Figure 5.45	Emission spectra at room temperature of Gd <sub>2-x</sub> Eu <sub>x</sub> O <sub>3</sub> nanocrystalline powders (x=0.15), annealed at different temperatures. The spectra were obtained by using a 250nm UV as excitation light. Similar behavior was observed for all Eu <sup>3+</sup> contents.	116
Figure 5.46	RT-Emission spectra Gd <sub>2-x</sub> Eu <sub>x</sub> O <sub>3</sub> nanopowders with different 'x' values annealed at different temperatures for 2 hours. Detail of the <sup>5</sup> D <sub>0</sub> - <sup>7</sup> F <sub>2</sub> transition, are shown on the right for each case.	117
Figure 5.47	Relation luminescence at 611nm and Eu <sup>3+</sup> concentration (a), and relationship between Log(I/x) and Log(x) in Eu <sup>3+</sup> -doped Gd <sub>2</sub> O <sub>3</sub> nanoparticles annealed at 750°C (b), 850°C (b) and 950°C (c).	120
Figure 5.48	Magnetization as function of applied field, at 300K, of Eu <sup>3+</sup> -doped Gd <sub>2</sub> O <sub>3</sub> nanopowders annealed at 950°C. A typical paramagnetic behavior is observed.	122
Figure 5.49	Magnetic susceptibility, at room temperature, of Gd <sub>2-x</sub> Eu <sub>x</sub> O <sub>3</sub> nanopowders, annealed at 950°C, as function Eu <sup>3+</sup> content. Solid line is only for visual help.	123

Figure 5.50	XRD patterns of the $\text{Eu}^{3+}$ -doped $\text{Gd}_2\text{O}_3$ thin films. Preferential orientation along (400) direction of cubic structure is observed for all 'x' values.	125
Figure 5.51	Lattice parameter and crystallite size as function of $\text{Eu}^{3+}$ ions content ('x') of highly oriented thin films.	125
Figure 5.52	Optical micrographs of (a) $\text{Gd}_2\text{O}_3$ and (b) $\text{Gd}_{2-x}\text{Eu}_x\text{O}_3$ ( $x=0.08$ ) thin films grown onto fused quartz by sol-gel and spin coating, and annealed at $750^\circ\text{C}$ for 1h.	126
Figure 5.53	Absorption (a) and transmission (b) spectra of $\text{Eu}^{3+}$ -doped $\text{Gd}_2\text{O}_3$ thin films with different contents of $\text{Eu}^{3+}$ , synthesized onto fused quartz.	127
Figure 5.54	Absorption spectra, showing the band gap of $\text{Eu}^{3+}$ -doped $\text{Gd}_2\text{O}_3$ thin films. No appreciable effect of $\text{Eu}^{3+}$ content is observed.	127
Figure 5.55	Excitation spectra of $\text{Gd}_{2-x}\text{Eu}_x\text{O}_3$ highly oriented thin films, with different content of $\text{Eu}^{3+}$ ions, and annealed at $750^\circ\text{C}$ . The spectra were taken monitoring the 611nm emission line.	129
Figure 5.56	Effect of excitation wavelength on intensity of luminescence from $^5\text{D}_0 \rightarrow ^7\text{F}_2$ transition of $\text{Gd}_{2-x}\text{Eu}_x\text{O}_3$ thin films.	130
Figure 5.57	Emission spectra, at room temperature, of $\text{Gd}_{2-x}\text{Eu}_x\text{O}_3$ highly oriented thin films, with different content of $\text{Eu}^{3+}$ ions, and annealed at $750^\circ\text{C}$ . The spectra were collected by using the 229 nm (a) and 250nm (b) excitation lines.	130
Figure 5.58	Relation of luminescence at 611nm and $\text{Eu}^{3+}$ concentration for $\text{Eu}^{3+}$ -doped $\text{Gd}_2\text{O}_3$ highly oriented thin films annealed at $750^\circ\text{C}$ .	131

# CHAPTER I: INTRODUCTION

## 1.1 Motivation

Nanosize materials have become the focus of intensive fundamental and applied research. The strong interest on these materials arises from the viability on designing and building structures that exhibit outstanding electrical, mechanical, chemical, optical and magnetic properties compared to the bulk materials. This feature of nanosize materials allows the achievement of unique properties enabling them to be considered for a wide range of markets, including medicine, plastics, energy, electronics, and aerospace. In addition, nanocrystals are increasingly used in various medical systems, such as drug targeting, magnetic fluid hyperthermia, and magnetic resonance imaging (MRI), among others. In this regard, nanosize rare earth (RE)-doped phosphors become a very promising type of material in terms of both their fundamental and potential applications including solid state lasers, lighting and immunoassays systems. In RE-doped nanoparticles, emission lifetime, luminescence quantum efficiency, and concentration quenching can be affected by particle size [1]

It is well established that phosphor luminescence depends on the type of host material and the dopant species (activator). A suitable host should exhibit a sufficiently large band-gap so that emission from the activator will not be absorbed, but not so large to waste the major fraction of the energy by excitations that require much greater energy than for relaxation. Under this perspective, ZnO has been proposed as a promising host material for optically active impurities such as RE ions.

Zinc Oxide is a II-VI compound that is receiving renewed interest based on the possibility to synthesize different types of nanostructures (single nanocrystals, thin films, nanocomposites) that exhibit enhanced properties when compared with the bulk counterpart. Nowadays, ZnO can be considered as one of most important multifunctional semiconducting materials. At ambient temperature the thermodynamically stable ZnO phase is wurtzite, which has a hexagonal structure. Due to its large binding energy, the corresponding exciton is stable at room temperature even in bulk crystals. This fact enables the use of ZnO for exciton-related optical devices, novel applications for future optoelectronic devices (such as light emitting diodes–LEDs and solar cells) and sensing (such as glucose sensor based on ZnO nanorods). In addition to spintronics applications, which is a new generation of microelectronics that utilizes both charge and spin degree of freedom of carriers, ZnO is bio-safe and biocompatible, hence can be used for biomedical applications [2]. Another notable property exhibited by ZnO is its large Zn-O bond energy, which allows a high damage threshold for laser irradiation [3]. In addition, the importance of both surface and confinement effects can be expected at the nanoscale. The main result of such effects will be the increase of the corresponding band gap energy in the nanosize crystals.

Regarding the potential use of ZnO as host structure for RE ions, there is still an unclarified controversy about the possible incorporation of RE species into the host oxide lattice. Although the actual incorporation of RE ions should not be a feasible process under equilibrium conditions (the ionic radii of RE ions are much larger than that for  $\text{Zn}^{2+}$ ) [4],

several reports stated the doping process to take place [5-7]. The actual incorporation of Eu species in the ZnO lattice would open new applications for this type of material due to the light emission efficiency, arising of the Eu-Zn interactions between atomic states associated with the dopant and the host lattice material is affected by the homogeneity in dispersion of ions and the quantum effects at the nanoscale. Accordingly, any effort to investigate the probable formation of Eu-doped ZnO and understand the interactions between dopant and host lattice will be justified.

On the other hand, it had been shown that the RE sesquioxides ( $\text{RE}_2\text{O}_3$ ), such as  $\text{Gd}_2\text{O}_3$ , can serve as host matrices for rare earth ions in the fabrication of nanophosphors. RE sesquioxides ( $\text{RE}_2\text{O}_3$ ), which exhibit three different structures at room temperature [8], are excellent host lattices for trivalent ions.  $\text{Gd}_2\text{O}_3$  is an inorganic insulator with a band gap of 5.4eV [9] and exhibits a cubic structure at room temperature (the phase transition of  $\text{Gd}_2\text{O}_3$  from cubic to monoclinic phase occurs at temperatures higher than 1250°C [8]). The well-known application of  $\text{Gd}^{3+}$  species as contrast agent for magnetic resonance imaging (MRI) opens interesting possibilities of using RE-doped  $\text{Gd}_2\text{O}_3$  nanophosphors as multifunctional fluorescence and MRI labels [10]. Among trivalent RE ions, europium is a well known red emitting species whose sharp photoluminescence (PL) peaks are associated to intra-4f shell transitions and whose spectral positions are independent of the embedding matrix but their intensities may vary [11,12]. Furthermore, due to crystal field effect, the individual levels (except  $^5\text{D}_0 \rightarrow ^7\text{F}_0$ ) are splitted up. The crystal-field splitting, appear as fine structure, and gives information about the symmetry of the rare-earth site and about the shape of the

coordination polyhedron. The intensities of spectral transitions reflect also the interaction between the RE ion and its environment [11].

Then, the properties expected in  $\text{Eu}^{3+}$ -doped  $\text{Gd}_2\text{O}_3$  nanostructures justify any effort to optimize the synthesis conditions of this material as well as its evaluation as phosphor and efficient biomarker. In addition,  $\text{Gd}^{3+}$  has a large spin-only magnetic moment, which makes it very suitable in biomedical applications [10,13,14].

Although RE-doped  $\text{Gd}_2\text{O}_3$  phosphors have been intensely studied in the past, there is still a lack of systematic studies on the synthesis and functional characterization of these materials as a function not only of composition but also crystal size at the nanoscale. The very small exciton Bohr radius (less than a few angstroms) for this type of materials suggests that strong quantum effects are either not expected [15], or that are quite weak [16,17]. Despite to unexpected quantum effects, it has been reported that smaller phosphors will enhance the resolution of displays. However, if the size of the particles is too small, the luminescence efficiency will be decreased for the re-absorption and scattering of the particles [18]; therefore, a suitable control of the crystal size should lead to higher packing density for phosphor layers and thus to a higher resolution in the corresponding display systems.

## **1.2 Aim of the present study**

### **1.2.1 Main objective**

The present research was focused on the systematic study of the effect of the atomic fraction of  $\text{Eu}^{3+}$  ions and crystal size on the structural, optical absorption, luminescence and magnetic properties of two nanocrystalline hosts: ZnO and  $\text{Gd}_2\text{O}_3$  (nanopowders, nanocrystals and thin films).

### **1.2.2 Specific objectives**

- i. To determine the optimum conditions for the synthesis of nanocrystalline ZnO doped with Europium.
- ii. To determine the optimum conditions for the preparation of nanopowders thin films and  $\text{Eu}^{3+}$ -doped  $\text{Gd}_2\text{O}_3$ .
- iii. To determine the structural and optical (UV-Vis and Photoluminescence) properties of produced nanostructures as a function of composition and crystal size at the nanoscale.
- iv. To undertake preliminary evaluation of the magnetic properties of Eu-doped Gd oxides as a function of the atomic fraction of the dopant species

It is known that, many methods, including hydrothermal [18], precipitation [19,20], combustion [21], spray pyrolysis [22], sol-lyophilization [23], and sol-gel [9,24], have been used to prepare nanocrystalline and thin films phosphors. The advantages of the sol-gel method include easier composition control, better homogeneity and a lower reaction temperature, which is better suited to synthesizing high purity, fine powders. However, the use of chelating agents to get a gel whose structure may greatly influence the final properties of the particles [23]. The gel solution is characterized by an interconnected and rigid network having sub-micrometer pores and polymeric chains with an average length in the micrometer range. Such a structure determines the size of the agglomerates obtained after drying. Furthermore, because the strong interaction between the nanometer sized particles of the agglomerates, particles coalescence can occur during further thermal annealing, which would lead to uncontrolled grain growth.

Therefore, in order to evaluate the possibility of doping for  $\text{Eu}^{3+}$ -containing ZnO, two methods of synthesis were used, through which were obtained two different nanostructures. First, using a simple Sol-Gel method without chelating agent, nanopowders (NPs) were obtained. Moreover, using a modified Sol-Gel method, ethanol-based, nanocrystals (NCs) were obtained. In both cases, the effect of the  $\text{Eu}^{3+}$  ions content was evaluated, and the annealing effect of NPs also was studied. For  $\text{Eu}^{3+}$ -doped  $\text{Gd}_2\text{O}_3$ , nanoparticles, the  $\text{Eu}^{3+}$  content and annealing temperature were evaluated, whereas the effect of  $\text{Eu}^{3+}$  content on properties of thin films was studied.

### **1.3 Summary of following chapters**

Chapter II will present the main characteristics and applications of phosphor materials semiconductor ZnO, and Gd<sub>2</sub>O<sub>3</sub>-based materials will be summarized. Special attention to their structural, optical, luminescent and magnetic properties will be given. In Chapter III an actualized review on previous related works on Eu<sup>3+</sup>-ZnO and Eu<sup>3+</sup>- Gd<sub>2</sub>O<sub>3</sub> systems will be offered. The details of the syntheses approaches and the characterization methods for produced nanostructures (nanocrystals, nanocrystalline powders and thin films) will be described in the Chapter IV. The results of the present research and the corresponding discussion will be presented in Chapter V. Finally, Chapter VI will summarize the main concluding remarks and suggested works.

## CHAPTER II: THEORETICAL BACKGROUND

### 2.1 Luminescence and phosphor materials

Luminescence is defined as a phenomenon in which the electronic state of a substance is excited by some kind of external energy and the excitation energy is given off as light, which includes not only electromagnetic radiation in the visible range (400-700nm), but also those in the neighboring regions on both ends [25]. Since luminescence is basically a non-equilibrium, it requires excitation by any type of energy, such as light, electron beams, current injection, etc., which generally act to create excess electrons, holes or both. The effects of electron-hole recombination give rise to luminescence. The material capable of converting the certain type of energy into electromagnetic radiation is called luminescent material or phosphor, which in general has three components: host lattice, activator and sensitizer.

According to the source of the excitation of energy, the luminescence can be classified, among others, as: **Photoluminescence**, which involves excitation by optical radiation that is usually UV radiation; **Cathodoluminescence**, when the excitation is by a beam of energetic electrons (or cathode rays); **Electroluminescence**, which occurs when the source of excitation is an electric field or currents; **Triboluminescence**, which is produced by mechanical energy such as grinding; **Chemiluminescence**, when the material is excited by the energy of a chemical reaction [25,26].

### **2.1.1 Mechanisms**

The mechanism of luminescence involves at least two steps: first the excitation of external energy and next the subsequent emission of photons. In the general mechanism of luminescence, the activator absorbs directly the exciting radiation, which then raises it to an excited state. This excited state then returns to the ground state by the emission of radiation: a photon. However, competing with this process are processes nonradiatives such as that occur when the energy of the excited state excites the lattice vibrations, or phonons, to heat the host lattice. These two forms of radiation are competitive. Therefore, in order to obtain an efficient phosphor, is necessary the suppression of all non-radiative processes.

On the other hand, it is also possible to excite the activator by indirect means. In this case a sensitizer is required. By this mechanism, the sensitizer absorbs the exciting radiation and then return to the ground state in three forms: by radiation, by the dissipation of the excitation energy in heat form, and by transfer of the energy to activator, which emits it. However, in many cases, the host lattice itself plays the part of sensitizer [26].

### **2.1.2 Hosts and activators**

Luminescent materials have a long story, and as was before indicated the efficiency of phosphor luminescence depends on the type of host material and the dopant species (activator). Therefore, many types of host and activator have been used in order to obtain phosphors more efficient. Recently, oxides-based host have gained growing interest, and

because of their unique properties, ZnO and Gd<sub>2</sub>O<sub>3</sub> are being intensively studied as host, particularly in order to obtain nanosized phosphors. Also, due to its characteristics sharp emission, the rare earth ions are used as activator. Particularly, Eu<sup>3+</sup> ions are being widely used. Just, both host ZnO and Gd<sub>2</sub>O<sub>3</sub>, and Eu<sup>3+</sup> as activator have been selected for this thesis work in order to obtain phosphors in the nanoscale level. Therefore, following a brief review of properties of these materials is given.

## **2.2 Zinc Oxide properties**

Zinc Oxide, an II-IV compound semiconductor with wide direct band gap (3.37eV, which is in the ultraviolet range) and large binding exciton energy (60meV) [27], has attracted renewed interest because of its relevance to a wide range of applications in many technological fields. Therefore, it should not be surprising that actually it is one of the most important functional semiconducting materials. Furthermore, due to its unique and tunable properties, intensive attention has been dedicated to study nanostructured ZnO, from both fundamental and technological view points. Currently, the strong interest in ZnO as a wide band gap semiconductor is based on their potential use in optoelectronic, spintronic and other electronic nanostructured devices, such as light emitting diodes (LEDs), solar cells, field emission display, etc. A summarized review on the structural and functional features of this material is presented as follows.

## 2.2.1 Crystal structure of Zinc Oxide

Most of the group II-IV binary compound semiconductors crystallize in either cubic zinc-blende or hexagonal wurtzite structure where each anion is surrounded by four cations at the corners of a tetrahedron, and vice versa, as shown in figure 2.1. Although this tetrahedral coordination is typical of  $sp^3$  covalent bonding, these materials exhibit a substantial ionic character. The ideal wurtzite structure has a hexagonal unit cell with two lattice parameters,  $a$  and  $c$ , in the ratio of  $c/a = \sqrt{8/3} = 1.633$ . This structure belongs to the space group of  $C_{6v}^4$  or  $P6_3mc$ . ZnO is an II-IV semiconductor whose ionicity ( $f_i = 0.616$  on the Philips ionicity scale [28]) resides exactly at the borderline between covalent and ionic semiconductors. Typical structures in ZnO are wurtzite, zinc-blende, and rocksalt, as schematically shown in figure 2.1. At ambient conditions, the thermodynamically stable phase is wurtzite, while the zinc-blende ZnO structure can be stabilized only by growth on cubic substrates. The rocksalt structure may be obtained at relatively high pressures [27].

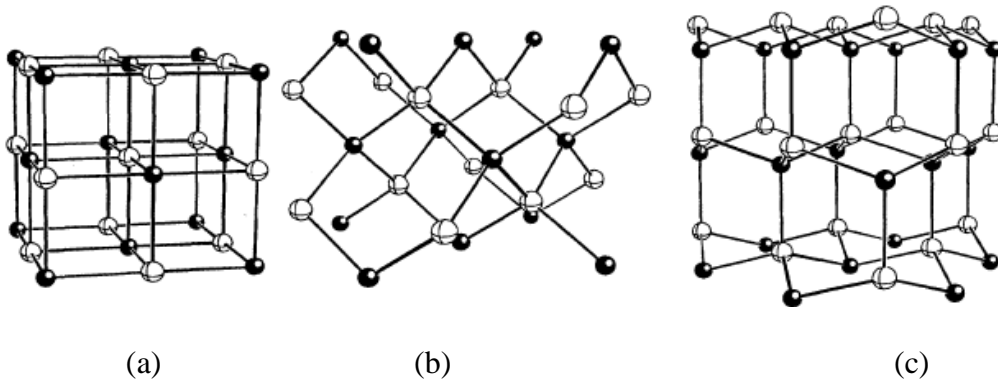


Figure 2.1 ZnO crystal structures: (a) rocksalt (B1), (b) zinc blende (B3) and (c) wurtzite (B4) [29].

The lattice constants for the bulk hexagonal ZnO are  $a=3.250 \text{ \AA}$  and  $c=5.206 \text{ \AA}$  (figure 2.2) [27]. Since ZnO is a two-element compound with different ion radii, the  $c/a$  ratio for ZnO hcp unit cell is 1.60, which is a little smaller than the ideal value of 1.633. Each O (or Zn) ion is tetrahedrally surrounded by four Zn (or O) ions in the wurtzite structure. Furthermore, each ion also has twelve next-nearest neighbors of the same type of ions. The O-Zn distance of the nearest neighbors is  $1.992 \text{ \AA}$  in the direction parallel to the  $c$ -axis of the hexagonal unit cell and  $1.973 \text{ \AA}$  in the other three directions of the tetrahedral arrangement. The tetrahedral arrangement between nearest neighbors indicates the covalent bond between the Zn and O atoms. The covalent radii of Zn and O were reported to be  $1.31 \text{ \AA}$  and  $0.66 \text{ \AA}$ , respectively [30].

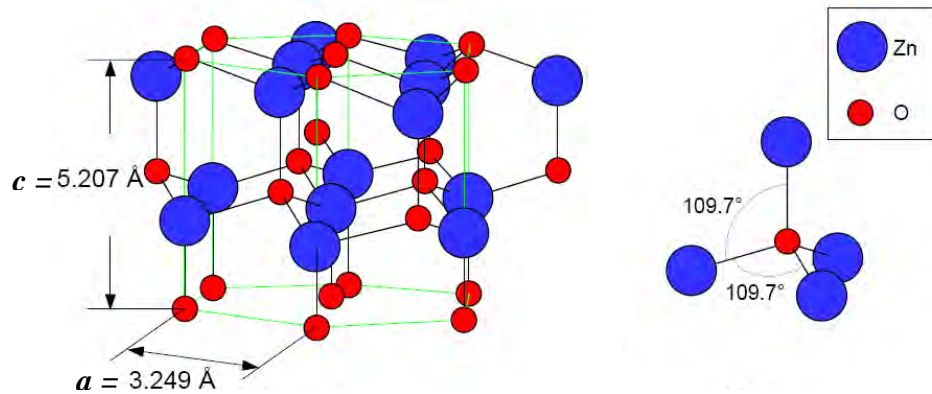


Figure 2.2 (a) Wurtzite crystal structure of ZnO with the regular hexagonal unit cell overlaid in orange. ZnO preferentially terminates on a polar face along the  $c$ -axis, O-polar termination is shown. (b) a single O atom surrounded by Zn atoms at the edges of a regular tetrahedron.

## 2.2.2 Electronic band structure of ZnO

For semiconductors, the energy of single free carrier is described by the band structure  $E(\mathbf{k})$ , which is a function of the quasi-momentum  $\mathbf{k}$  determined by the periodic boundary conditions. The properties of the band structure are determined by the symmetric properties of the semiconductor crystal and the chemical binding of the constituting elements. The crystal and electronic band structure of ZnO have been studied by various total-energy methods: Hartree-Fock, Local Density Approximation (linear muffin-tin orbital), Linear Combination of Atomic Orbitals (LCAO), pseudopotential and full-potential linearized augmented-plane-wave, self-interaction corrected pseudopotentials, and the GW approximation [31].

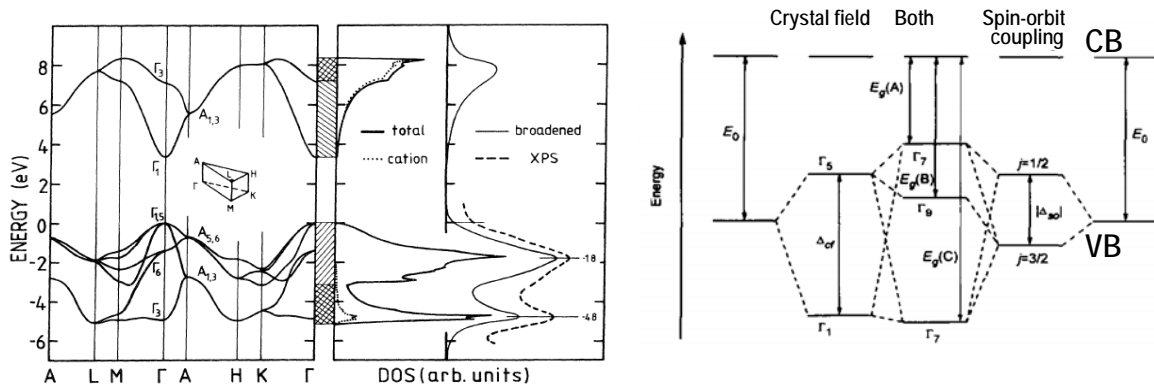


Figure 2.3 (a) Bulk band structure of ZnO for various high-symmetry lines in the irreducible part (see inset) of the bulk Brillouin zone and density of states. The full line shows the total density of states and the dotted line gives the cation contribution to the DOS. [28]; (b) Splitting of the VB in hexagonal ZnO under the influence of crystal field and spin-orbit coupling. (The figure is not drawn to scale) [32]

Figure 2.3 shows the band structure of bulk ZnO near the  $\Gamma$  point of the Brillouin zone. As was mentioned above, ZnO has rather ionic binding. Consequently, the conduction band (CB) arises essentially from  $\text{Zn}^{2+}$  4s orbitals, whereas the upper valence bands (VB)

from the  $O^{2-}$  2p states with an admixture of  $Zn^{2+}$  3d levels. The valence band is *p* like, splitting into three doubly degenerate bands due to hexagonal crystal field ( $\Delta_{cf}$ ) and spin-orbit ( $\Delta_{so}$ ) interactions labeled as A, B and C from higher to lower energies. Their ordering has been found to be  $\Gamma_{7(5)}$ ,  $\Gamma_{9(5)}$  and  $\Gamma_{7(1)}$  respectively, in which the number in parentheses indicates the parent state without spin-orbit coupling. This particular ordering results from the negative spin-orbit splitting, which in turn is due to the participation of the  $Zn^{2+}$  3d levels [33]. The possibility of a negative spin-orbit splitting was first suggested by Cardona [34]. However, the ordering of the valence bands, has been subject to extensive discussions [33-35] since the early investigations of the valence band maximum fine structure by Thomas in 1960 [36], who suggested that the symmetry of the valence bands from the A, B, and C band is  $\Gamma_7$ ,  $\Gamma_9$  and  $\Gamma_7$  and therefore anomalous compared to the usual ordering in the other wurtzite II-IV materials like ZnSe and CdS.

### **2.2.3 Luminescence of ZnO**

Zinc Oxide is a well known luminescent material for one century and several works about its luminescent properties can be found in the literature. These works had been encouraged either by the fundamental research interests or by the industrial demands of optoelectronic devices. Typically, the room-temperature photoluminescence (PL) spectra of ZnO nanostructures shows one peak at UV region, just below the onset of absorption, and one or more peaks in the visible spectral range. Usually, the UV band is assigned as due to the radiative annihilation of excitons with a very short lifetime (several tens to

hundreds of picoseconds). The visible photoluminescence (PL) is commonly green, though other emission peaks such as red and yellow, have also been reported in the range from 450 to 730nm. In contrast to the exciton emission, the lifetime of the visible emission is much longer in the  $\mu\text{s}$  range. This is attributed to the presence of defects, non-stoichiometry and crystal imperfections. The most referred defects in ZnO are Zn interstitial ( $\text{Zn}_i$ ), oxygen vacancies ( $\text{V}_\text{O}$ ), Zn vacancies ( $\text{V}_{\text{Zn}}$ ), Zn anti-sites ( $\text{O}_{\text{Zn}}$ ), etc. (figure 2.4). The  $\text{V}_\text{O}$  and  $\text{Zn}_i$  defects contribute as shallow donor states whereas  $\text{V}_{\text{Zn}}$ ,  $\text{O}_i$  and  $\text{O}_{\text{Zn}}$  are considered deep level acceptor states in the band gap [37]. However, although the exact origin of the visible emission is still not well understood, and controversial hypotheses have been proposed to explain the different emissions, the green emission band is considered as the fundamental feature for ZnO to be used as a green emission phosphor for the planar display and short-decay cathode-luminescence screens. The origin of the yellow and orange-red emissions has been less controversial. It has been proposed that these two emissions may involve similar deep levels but different initial states (conduction band and shallow donors); they were also found to exhibit different dependences on the excitation wavelength. The yellow emission is commonly attributed to oxygen interstitial defects, although some impurities such as Lithium may also play a role [38]. In addition to this common hypothesis, the possible presence of  $\text{Zn}(\text{OH})_2$  at the surface was identified as a possible reason for the weak UV and the strong visible (broad yellow and green) emission. The orange-red emission centered around  $\sim 640 - 650 \text{ nm}$  is also commonly attributed to the presence of excess oxygen in the samples, such as

oxygen interstitial defects. Other hypotheses include surface dislocations and zinc interstitials [39].

As mentioned, the most commonly observed green defect emission is also the most controversial one; this origin has been the subject of many speculations: oxygen vacancies ( $V_0^+$ ) zinc interstitials transitions from Zn interstitials to Zn vacancies Zn-O anti-sites and extrinsic impurities. However, the characterization of native point defects itself in ZnO is still a question of debate. Using first principles methods, the electronic, structure, atomic geometry, and formation energy of native point defects in ZnO have been determined [31,40]. However, nevertheless the intense research carried out so far, there is not an agreement on the origin of the luminescence in the visible region, and this matter keeps as an issue of active investigation.

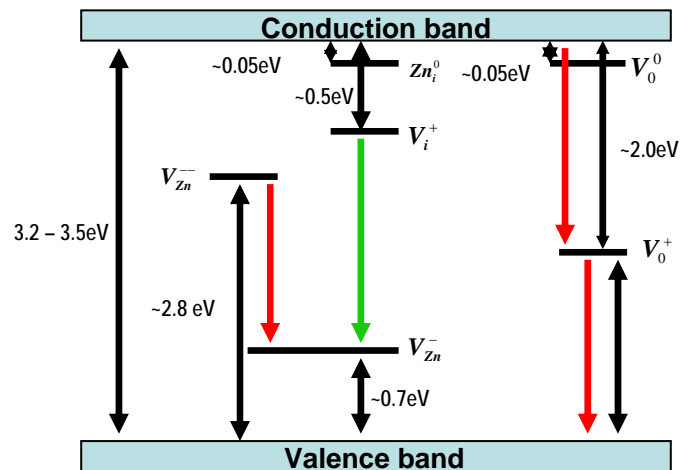


Figure 2.4 Schematic electronic level diagram of ZnO. The non-radiative transitions (black arrows), possible red emission (red arrows), and green emission (green arrow) are shown.

Also, it was proposed that green emission in ZnO originates from Cu impurities [41,42]. However, the dependence of the PL spectra on the fabrication environment [43] and annealing conditions [44] appears to be more consistent with an intrinsic defect than an extrinsic impurity. Vanheusden *et al.* [45] observed a correlation between the intensities of  $g < 1.96$  electron paramagnetic resonance (EPR) peak and green photoluminescence (PL). They proposed that green PL originates from a transition between singly charged oxygen vacancy and photoexcited hole. However, the assignment of  $g \approx 1.96$  signal to singly ionized oxygen vacancy is still debatable. This signal was also assigned to shallow donors [42] regardless of the shallow donor identity and free electrons, while  $g_{\perp} = 1.9945$  and  $g_{\parallel} = 1.9960$  signals were assigned to singly ionized oxygen vacancies  $V_0^{+3}$ . Furthermore, theoretical predictions indicate that the native shallow donor in ZnO is interstitial Zinc,  $Zn_i$ , while oxygen vacancy is a deep donor. Therefore, the hypothesis of correlation between green PL and presence of oxygen vacancies based on  $g \approx 1.96$  EPR signal could be not accepted. In addition, no relationship between green emission and  $g \sim 1.96$  EPR signal was found by D. Li et al. [38], in nanostructures of ZnO, while their samples with yellow emission exhibited strong EPR signal (Figure 2.5-a).

Other proposed mechanisms that would be involved with the PL behavior of ZnO include transition between the electron close to the conduction band and deeply trapped hole at  $V_0^{++}$  center (oxygen vacancy containing no electrons) [46,47], donor–acceptor and shallow donor–deep level transitions [48,49] zinc interstitials and antisite oxygen [50].

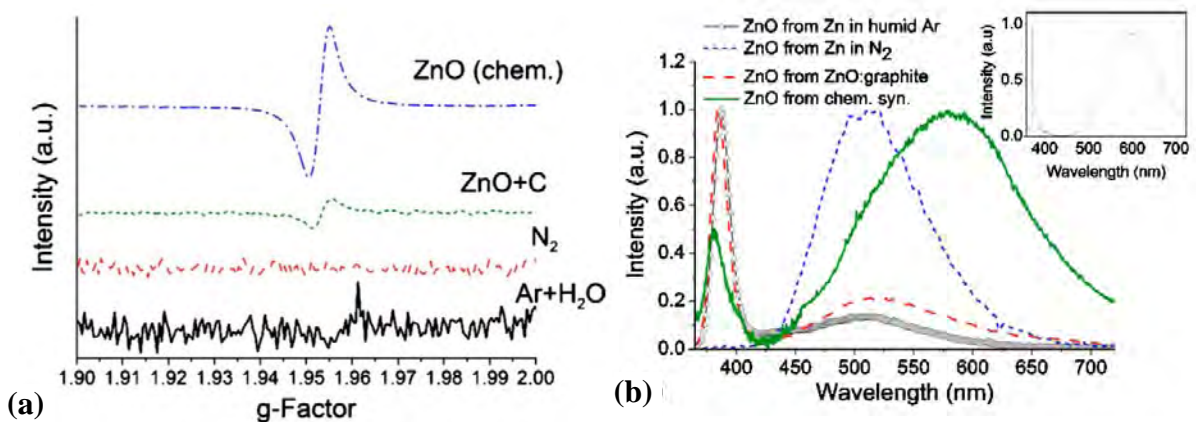


Figure 2.5 EPR (a) and Photoluminescence (b) spectra measured at room temperature from ZnO structures using different methods. EPR spectra have been vertically shifted for clarity. The inset in (b) shows the PL from the sample fabricated by a chemical method at 4 K. [38]

It is possible that visible luminescence in ZnO has different origins in different samples. For example, single crystals and phosphor powders may be more likely to exhibit impurity related emission, while nanostructures and epitaxial thin films are more likely to exhibit emission due to intrinsic defects [38].

The close relationship between the luminescence properties of the nanocrystalline ZnO, the synthesis method and post annealing conditions have been evidenced in various experimental works. For instance, D. Li *et al.* [38], have found that the luminescence peak in the visible region has different positions in samples prepared by chemical and evaporation methods. The samples fabricated by evaporation exhibited green luminescence due to surface centers, whereas the samples fabricated by chemical methods exhibited a yellow luminescence that was not affected by the surface

modification (Figure 2.5-b). Z. G. Wang et al., [51] investigated the luminescence properties of ZnO nanoparticles (20nm) annealed in air, Ar and O<sub>2</sub> atmosphere. They observed green emissions centered at 490, 515 and 520nm after annealing in Ar, O<sub>2</sub> and air atmosphere at 900°C for 1h, respectively, as shown in figure 2.6. The corresponding XPS analyses evidenced the presence of oxygen vacancies on the surface of the ZnO annealed in Ar, while there is little oxygen vacancy on the surface of the ZnO annealed in O<sub>2</sub>. Thus, the appearance of green emission at about 490nm was attributed to the formation of oxygen vacancy defects. In turn, the emission at 520nm could be consequence of the anti-site defects (O<sub>Zn</sub>).

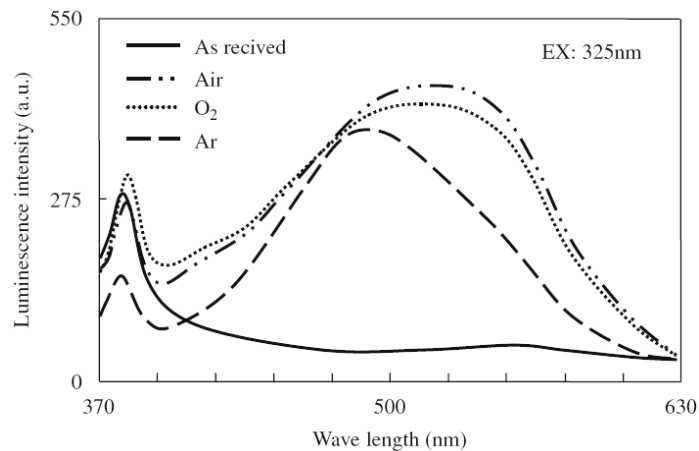


Figure 2.6 PL spectra for the as-received ZnO nanoparticles and those annealed in air, O<sub>2</sub>, and Ar atmospheres at 900°C for 1 h. The excitation wavelength was 325nm. [51]

A.B. Djurišić et al., [39], have been studied the defects in three different types of ZnO nanostructures, with and without annealing under different conditions. ZnO were synthesized as rods through a hydrothermal method, and hollow shells prepared by thermal evaporation in a tube furnace. They found that the emissions from the defect

exhibited a strong dependence on the temperature and excitation wavelength; some defect emissions were observable only at low temperatures and certain wavelengths, as shown in figure 2.7.

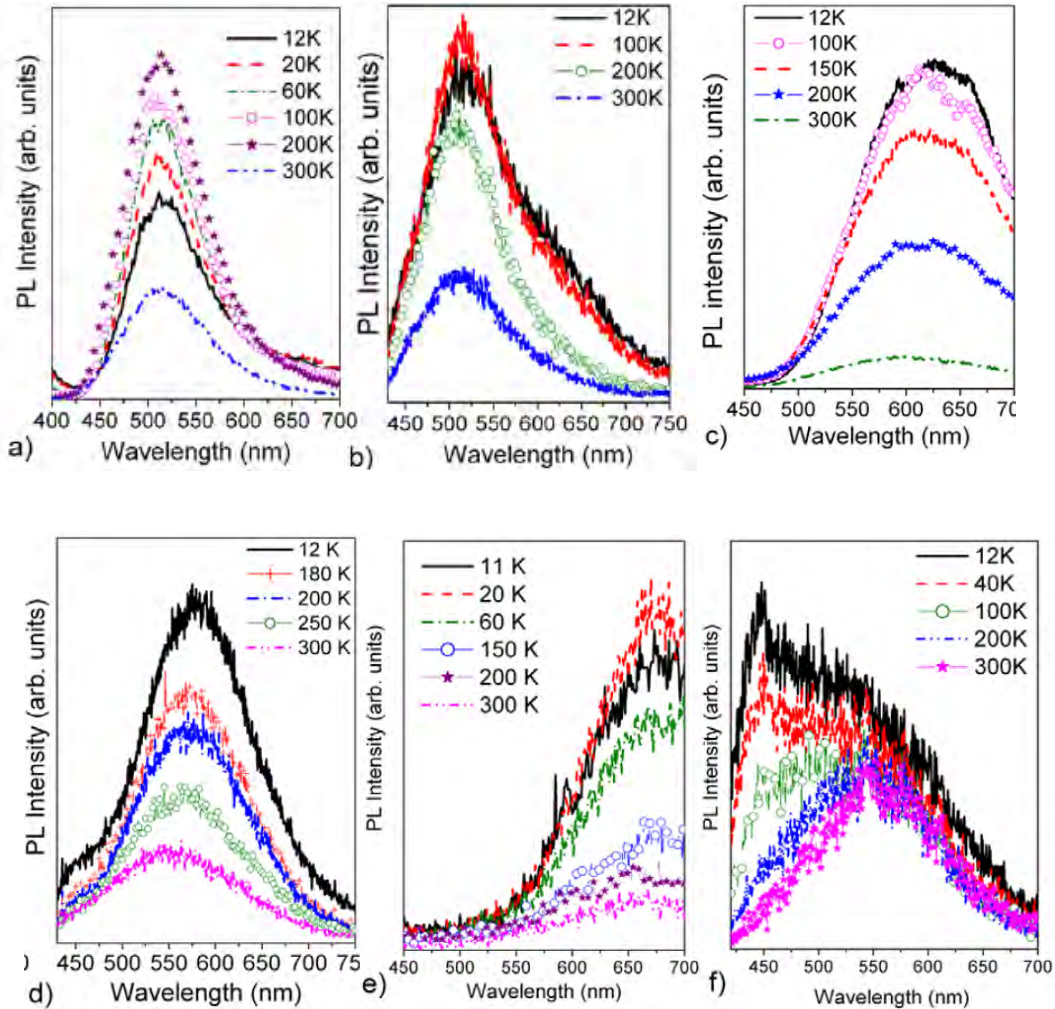


Figure 2.7 Variable temperature PL spectra (defect emission) of different ZnO nanostructures excited at 325 and 390 nm: (a), (b) shells, ((c) and (d)) rods and ((e), (f)) needles [39].

## 2.3 Triply-ionized Rare Earths

Because of their very special optical properties, many rare earths have been used in lasers and amplifiers within almost all spectral regions in the region between ~450 nm and ~2900 nm. In crystalline hosts, high cross sections (and therefore high gain) can be achieved, making these systems great candidates for lasers. In glassy environments, the ability of obtaining amplification across a wider range of frequencies (for a large variety of chemical compositions) and the attainment of high optical quality transmission make these materials more suitable for optical amplifiers.

### 2.3.1 General properties

Rare earths (RE) form a group of chemically similar elements which have in common an open 4f shell. In neutral state, these elements possess the electron configuration  $4f^n 6s^2$ , except for Gadolinium, which shows the configuration  $4f^n 5d 6s^2$ , where the number of f electrons 'n' ranges from 2 for Cerium to 14 for Ytterbium. Unlike the corresponding 3d transition series, the 4f electrons of the RE generally remain highly localized in the solid, and they have almost no contribution to the chemical valence, therefore the atom can easily lose the 6s and 5d electrons and also one electron from the 4f shell, so they are most stable as trivalent ions, although 2+ or 4+ are frequently found in some compounds. The series is conveniently divided at the point of a half-filled 4f shell into light (La-Eu) and heavy (Gd-Lu) groups.

Table 2.1 Filling of 4f shells of trivalent ions RE according to Hund's rules [52].

	$m_l$	-3	-2	-1	0	1	2	3	$S^{(a)}$	$L^{(b)}$	$J^{(c)}$	$^{2S+1}L_J$
$Ce^{3+}$	$4f^1$	↓							1/2	3	5/2	$^2F_{5/2}$
$Pr^{3+}$	$4f^2$	↓	↓						1	5	4	$^3H_4$
$Nd^{3+}$	$4f^3$	↓	↓	↓					3/2	6	9/2	$^4I_{9/2}$
$Pm^{3+}$	$4f^4$	↓	↓	↓	↓				2	6	4	$^5I_4$
$Sm^{3+}$	$4f^5$	↓	↓	↓	↓	↓			5/2	5	5/2	$^6H_{5/2}$
$Eu^{3+}$	$4f^6$	↓	↓	↓	↓	↓	↓		3	3	0	$^7F_0$
$Gd^{3+}$	$4f^7$	↓	↓	↓	↓	↓	↓	↓	7/2	0	7/2	$^8S_{7/2}$
$Tb^{3+}$	$4f^8$	↓↑	↓	↓	↓	↓	↓	↓	3	3	6	$^7F_6$
$Dy^{3+}$	$4f^9$	↓↑	↓↑	↓	↓	↓	↓	↓	5/2	5	15/2	$^6H_{15/2}$
$Ho^{3+}$	$4f^{10}$	↓↑	↓↑	↓↑	↓	↓	↓	↓	2	6	8	$^5I_8$
$Er^{3+}$	$4f^{11}$	↓↑	↓↑	↓↑	↓↑	↓	↓	↓	3/2	6	15/2	$^4I_{15/2}$
$Tm^{3+}$	$4f^{12}$	↓↑	↓↑	↓↑	↓↑	↓↑	↓	↓	1	5	6	$^3H_6$
$Yb^{3+}$	$4f^{13}$	↓↑	↓↑	↓↑	↓↑	↓↑	↓↑	↓	1/2	3	7/2	$^2F_{7/2}$

(a)  $S = |\sum m_s|$  with  $=+1/2(\uparrow)$  or  $-1/2(\downarrow)$

(b)  $S = |\sum m_l|$

(c)  $J = |L - S|$  (less than half-filled shell),  $J = L + S$  (otherwise)

(d) Predicted ground state according to Hunds' rules

The filling of the of the 4f shell can be explained by Hund's rules [52], which predict that the term with the highest quantum number S has the lowest energy and if there are several terms with the same S, the one with the highest angular momentum quantum number L has the lowest energy. Furthermore, due to spin-orbit coupling, the terms  $2S+L$  are split into levels  $J=L+S, L+S-1, \dots, |L-S|$ , where for less than half-filled shells, the term with the smallest J has the lowest energy. In this way one can predict the ground state of the ions, as shown in table 3.1. The optical and magnetic properties of the RE

ions are determined by the 4f electrons, which are well shielded from the environment by the outer 5s and 5p electrons.

On the other hand, the general tendency toward trivalent state is clearly related to the increasing localization of the *f* electrons with atomic number. The highly directional *f*-orbitals are only partially able to screen each other from the attractive force of the nucleus, which leads to the well-known lanthanide contraction. This interesting property of the lanthanide series consist in the decrease in both the ionic and covalent radii (figure 2.8) and the increase in Pauling's electronegativity by increasing nuclear charge. This effect is the main reason for differences found in compounds throughout the lanthanide series.

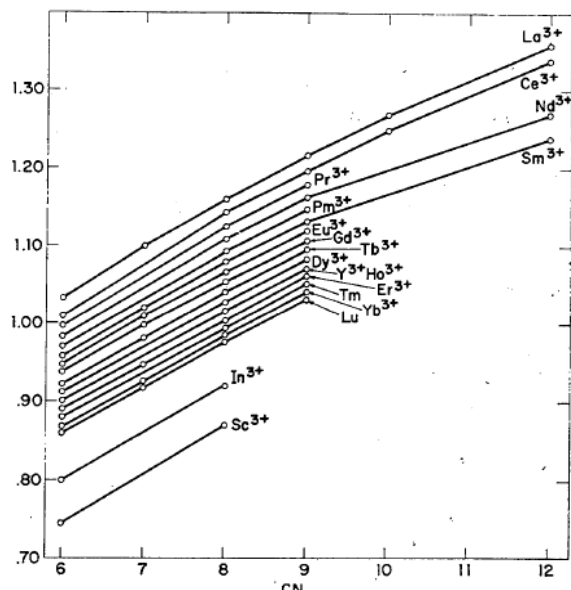


Figure 2.8 Effective ionic radius ( $\text{\AA}$ ) for some common cations (CN: coordination number) [4].

### 2.3.2 Incorporation of Rare Earth ions into solid lattices

When a RE ion is incorporated in a solid, it will interact with the ions in the host structure; and this interaction can be expressed by the Hamiltonian for the ion-host combination and written as:

$$\mathbf{H} = \mathbf{H}_0 + \mathbf{H}_{el} + \mathbf{H}_{SO} + \mathbf{H}_{CF}$$

Or,

$$\mathbf{H}_0 = -\frac{\hbar^2}{2m} \sum_{i=1}^N \frac{\partial}{\partial \mathbf{r}_i} - \sum_{i=1}^N \frac{\mathbf{Z}^* e^2}{r_i} - e^2 \sum_i \sum_{j,j>1} \frac{1}{r_i - r_j} + \xi \sum_i s_i \cdot l_i - e \sum_j \frac{\mathbf{Z}_j}{\mathbf{R}_j - \mathbf{r}_i} \quad (2.1)$$

In this equation, the first term, from left to right, is the kinetic energy and the second term is the potential energy of the 4f electrons. These two terms represent the central field Hamiltonian ( $\mathbf{H}_0$ ) that represents the interaction between the electrons and nucleus. The sum runs over all 4f electrons.  $\mathbf{Z}^*$  represents the atomic potentials screened by the inner electrons. Both the term representing the kinetic energy of the electrons and the one representing the potential energy are spherically symmetric. The third term represents the electrostatic interaction,  $\mathbf{H}_{el}$ , between electrons (Coulombic interaction), and is explained in terms of Legendre polynomials and application of the spherical-harmonic addition theorem. The fourth term corresponds to the spin-orbit interaction,  $\mathbf{H}_{SO}$ . These first four terms represent the Hamiltonian of the free RE ion; the other one,  $\mathbf{H}_{CF}$ , describes the interaction between the ion and the crystal field of the environment. The total Hamiltonian should also include other interactions, such as the interaction with the lattice

phonons ( $V_{\text{phon}}$ ) and with the electromagnetic field ( $V_{\text{EM}}$ ). Since it has been demonstrated that the interaction of the 4f electrons with the surrounding ionic environment is very weak, the last term in equation (2.1) is treated as perturbation. [52]

The solution to the free ion Hamiltonian is described by a set of  $(2J + 1)$ -fold degenerate states labeled using the spectroscopic notation  $^{2S+1}L_J$ , where  $S$  is the total spin,  $L$  is total orbital angular momentum and  $J = S + L$  is total angular momentum due to all 4f electrons of the ion. The states with different  $L$  and  $S$  quantum numbers are mixed by the spin-orbit interaction (Russell-Saunders coupling), which lifts the degeneracy in the total angular momentum into  $J$  levels, separated by few thousand  $\text{cm}^{-1}$ . The mixed states represent the eigen-states of  $J$  but not of  $L$  or  $S$ . Then,  $L$  and  $S$  are not good quantum numbers for describing the state of the free ion. [52]

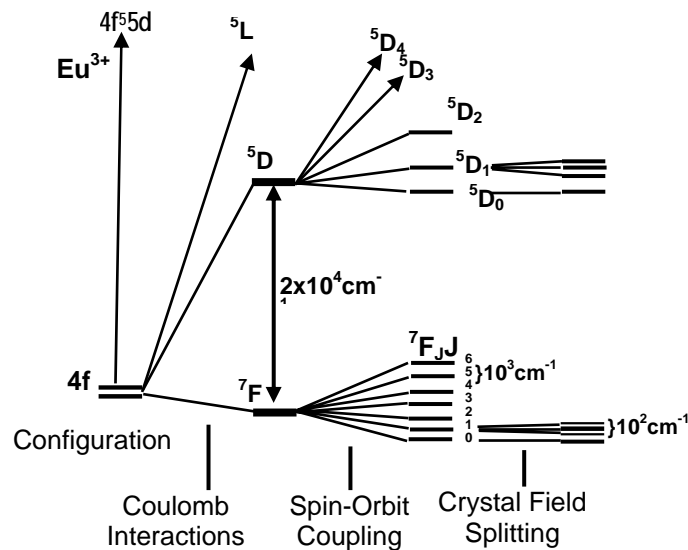


Figure 2.9 Interactions leading to the different electronic energy levels for the  $[\text{Xe}] 4f^6 5d^0$  configuration of  $\text{Eu}^{3+}$  (six electrons in the 4f orbitals). [12]

On the other hand, the crystal field splits each  $J$  level into  $(2J + 1)$  Stark components, which are separated by few hundred  $\text{cm}^{-1}$ . The effect of the above terms of the Hamiltonian on the energy splitting is shown in Figure (2.9) [12]. Consequently these splitting result in numerous energy levels, and the optical transitions occur between states belonging to the same  $4f^n$  ground state electronic configuration. The absorption or emission spectrum of a trivalent rare earth ion in a crystalline environment consists of many fine peaks. Also, as before mentioned, the importance of the fine structure is that it allow us obtain information about the symmetry of the rare-earth site, i.e. on the crystallintiy of the environment.

### **2.3.3 Rare Earth ions as optical dopants**

Due to their very distinct chemical and optical properties, RE-bearing compounds are extensively used in a large number of applications, such as superconductors, optical fibers, data storage, nuclear technology, high-power laser systems, magnetostrictive alloys, magnetic refrigeration, paint and coatings, permanent magnets, catalysts, etc. As before indicate, because of the identical configuration of the outermost ( $6s$ ) shell, all RE elements are chemically very similar. This strong chemical affinity makes any selective separation process between RE species a very difficult task; therefore, rare-earth compounds usually containing minor proportions of other RE species. Since the  $4f$  electrons of the RE are shielded from perturbations with the lattice by the outer  $5s$  and  $5p$  electrons, the  $4f$  orbitals retain their hydrogenic character, resulting in sharp transitions between the  $4f$  levels. Consequently, RE species will exhibit temperature stable and sharp

spectroscopic emission lines largely independently of the type of the host material [53]. This is a major advantage since the wavelength required for a specific application can be matched with the energy of transitions in the 4f-shell of the RE atoms to effectively select an appropriate emitter.

### 2.3.4 Luminescence of Rare Earth ions in host solid compounds

As was before indicated, Rare earths species exist as 3+, or occasionally 2+ ions when incorporated in a solid host. The trivalent ions exhibit intense narrow-band intra-4f luminescence in a wide variety of hosts, whereas the shielding provided by the 5s<sup>2</sup> and 5p<sup>6</sup> electrons causes that rare-earth radiative transitions in solid hosts resemble those of the free ions and, as a consequence, the electron–phonon coupling becomes weak.

In principle the rare earth ions can be classified in three groups [11,25] according to their strength of luminescence:

- a) Tb<sup>3+</sup>, Dy<sup>3+</sup>, Eu<sup>3+</sup> and Sm<sup>3+</sup> are the strongest emitters, which all have fluorescence in the visible region. (Tb<sup>3+</sup>: 545nm, D<sub>4</sub><sup>5</sup> → F<sub>4</sub><sup>7</sup>; Dy<sup>3+</sup>: 573nm, F<sub>9/2</sub><sup>4</sup> → H<sub>13/2</sub><sup>6</sup>; Eu<sup>3+</sup>: 611nm, D<sub>0</sub><sup>5</sup> → F<sub>2</sub><sup>7</sup>; Sm<sup>3+</sup>: 643nm, G<sub>5/2</sub><sup>4</sup> → H<sub>11/2</sub><sup>6</sup>).
- b) Er<sup>3+</sup>, Pr<sup>3+</sup>, Nd<sup>3+</sup>, Ho<sup>3+</sup>, Tm<sup>3+</sup> and Yb<sup>3+</sup> are weak emitters in the near infrared region.

The weakness of their luminescence is based on the fact that these ions have closely spaced energy levels, making the non-radiative transition easy. For the erbium ion

there are, besides some other very weak spin forbidden lines (e.g.  $4f^{n-1}5d \rightarrow 4f^n$ ), two characteristic transitions: one in the visible region at about 550 nm ( ${}^4S_{3/2} \rightarrow {}^4I_{15/2}$ ) and the other, the most important one for commercial use, at 1.55 $\mu$ m ( ${}^4I_{13/2} \rightarrow {}^4I_{15/2}$ ).

c)  $\text{La}^{3+}$ ,  $\text{Gd}^{3+}$  and  $\text{Lu}^{3+}$  exhibit no ion fluorescence because the lowest-lying resonance level lies far above the triplet level of any of the commonly used ligands.

Like other RE-ions, the luminescence attributed to trivalent Eu is characterized by sharp peaks attributed to the intra-4f shell transitions  ${}^5D_0 \rightarrow {}^7F_j$  (see figure 2.10) [11,53]. After excitation with energy of at least 2.18 eV the energy state  ${}^5D_0$  is populated and, by recombination to the  ${}^7F_j$  states, red light is emitted. The spectral positions are independent of the embedding matrix but their intensities may vary [11,12]. Moreover, due to crystal field, the individual j-levels (except  $j = 0$ ) are splitted up, and the crystal-field splitting appears as fine structure and provides information about the symmetry of the rare-earth site and the shape of the coordination polyhedron. The intensities of spectral transitions reflect also the interaction between the RE ion and its environment [11,12].

A number of excitation pathways are available for rare-earth luminescence in solid hosts, which can be broadly classified as either direct or indirect excitation mechanisms. For instance, in the  $\text{Eu}^{3+}$ -doped  $\text{Gd}_2\text{O}_3$  system the different sensitization processes of  $\text{Eu}^{3+}$  are the following: the host  $\text{Gd}_2\text{O}_3$  absorption, O-Eu charge transfer, the  $\text{Gd}^{3+}$  ion absorption and the  $\text{Eu}^{3+}$  ion self-excitation. After Ch. Liu, et al. [53] the excitations from the host

band and charge transfer band for the  ${}^5D_0 \rightarrow {}^5F_2$  transition of  $\text{Eu}^{3+}$  ions, in nanocrystalline, are almost equal for the bulk  $\text{Gd}_2\text{O}_3$ .

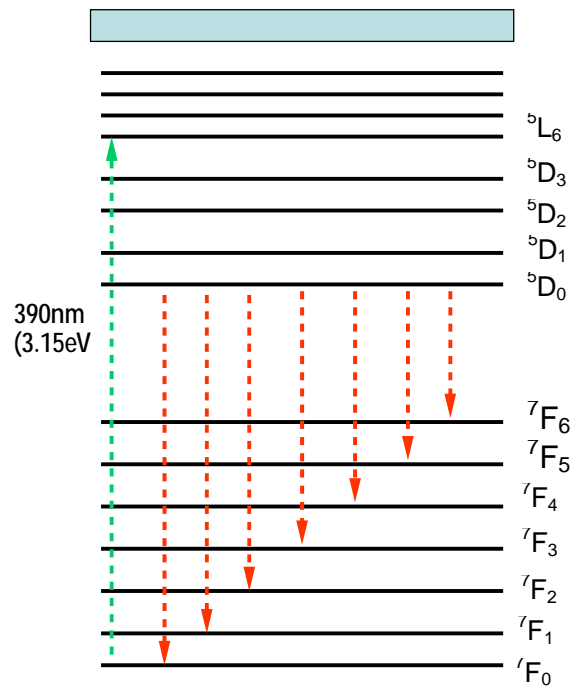


Figure 2.10 Energy level diagram of the optical transitions within  $\text{Eu}^{3+}$  ions.

### 2.3.5 Energy transfer

The excitation residing in an ion can migrate to another of the same species in the ground state as a result of resonant energy transfer promoted by the shortening of the inter-ionic distance. Energy migration processes increase the probability to optical excitation be trapped at defects or impurity sites, enhancing non-radiative relaxation. This non-radiative relaxation will be enhanced by increasing the concentration of the RE species leading to concentration quenching. Also, the energy transfer between different ion

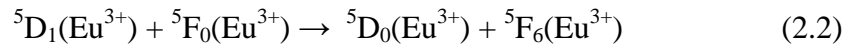
species can take place when they have closely matched energy levels. Then, the energy transfer from the host crystal to luminescent dopants leads to host-excited luminescence. Therefore, the energy transfer process will result either in the enhancement or in the quenching of emission.

In order to demonstrate the occurrence of energy transfer, various methods have been proposed [26]. One of them is based on the measurement of the excitation spectrum of the emission from the luminescent dopant. If the excitation spectrum of the dopant emission shows the excitation band of the host in addition to those of dopant, this indicates energy transfer from the host to luminescent dopant. This fact would indicate that the actual incorporation of dopant in the host structure was accomplishment, and therefore a phosphor material is obtained.

### **2.3.6 Concentration quenching**

It seems logic to think that a rise in the luminescent ion concentration would permit to obtain high emission intensity in the host solid. However, in many cases the emission efficiency decreases after the concentration of the luminescent ion exceeds a specific value known as the critical concentration. This effect, so-called *Concentration Quenching*, can be explained in several cases as follows. If the concentration of the luminescent dopant becomes so high that the probability of energy transfer exceeds that from emission, the excitation energy starts migrating through the lattice. However, the host lattice is no perfect since that contains all types of sites (surface, dislocations,

impurities, etc.) where the excitation energy may somehow be lost. In the case of  $\text{Eu}^{3+}$  ions, their luminescence spectra have strong dependence on the RE-ion concentration. This is because at higher concentrations, the higher emitting levels,  $^5\text{D}_1$  of  $\text{Eu}^{3+}$  transfer their energy to neighboring ions of the same species throughout cross-relaxations according to [25]:



As was initially cited, after B.M. Tissue [1], in RE-doped nanoparticles the particle size may affect the concentration quenching, and an increasing in concentration quenching as the particle size reduces has been proposed. This effect is attributed to a reduced energy transfer rate due to the interfaces, so less energy can migrate to quenching sites. The change in concentration quenching also suggests that the close proximity of the surface does not introduce a large number of quenching surface defects. However, the method and conditions of synthesis seems play a key role to determine the specific value.

### **2.3.7 Charge transfer band (CTB)**

An important excitation pathway in  $\text{RE}^{3+}$  doped inorganic materials is the charge transfer band (CTB). For example, in this mechanism  $\text{Eu}^{3+}$  is reduced to  $\text{Eu}^{2+}$  and the coordinating anions in the crystal are oxidized upon absorption of a photon with sufficient energy. When the energy of this charge transfer band is not too low, deactivation of the CTB to the  $^5\text{D}_j$  levels results in an excited  $\text{Eu}^{3+}$  ion (see Figure 2.11).

This excitation pathway is strongly dependent on the type of host materials, because the crystal matrix is oxidized. Variations in the matrix will shift the CTB in the coordinate diagram in Figure 2.11 vertically and/or horizontally.

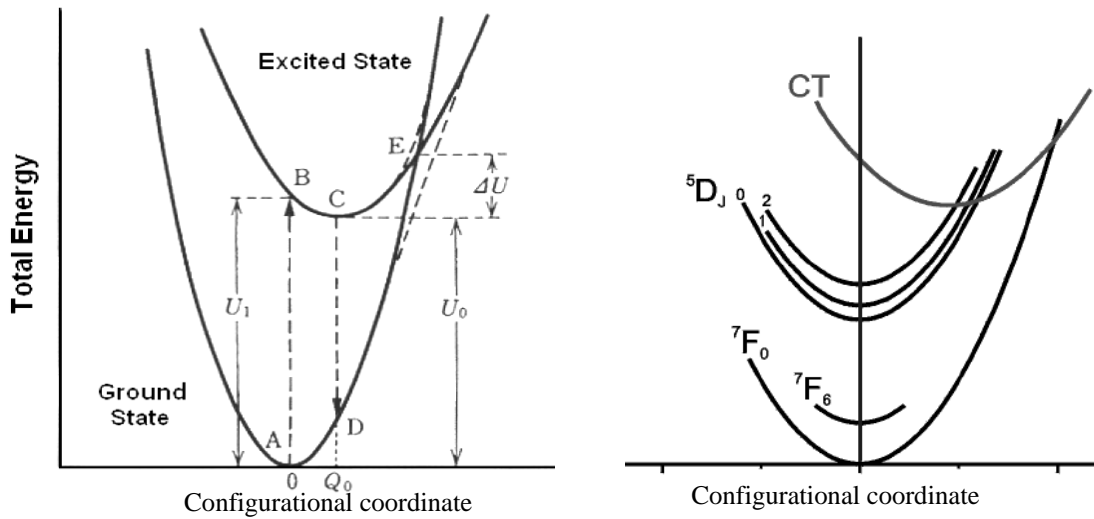


Figure 2.11 Schematic illustration of a configurational coordinate model. The two curves are modified by repulsion near the intersection (broken lines). The vertical broken lines  $A \leftrightarrow B$  and  $C \leftrightarrow D$  indicate the absorption and emission of light, respectively (left) [25], and coordinate diagram with the  ${}^7F_J$  ground states ( $J = 1-6$ , levels with  $J = 2-5$  are not shown), the  ${}^5D_J$  excited states ( $J = 0-2$  are shown), and the charge transfer state of  $\text{Eu}^{3+}$  (right) [26]

In the case of Eu-O interaction, the CTB can be estimated from the Jorgensen's relation [54]:

$$\sigma = [\chi(x) - \chi(M)](3 \times 10^4) (\text{cm}^{-1}) \quad (2.3)$$

Where  $\sigma$  denotes the position of the CTB (in  $\text{cm}^{-1}$ );  $\chi(x)$  and  $\chi(M)$  are the optical electronegativity of the anion and the central metal ion, respectively. For  $\chi(\text{O}) = 3.2$  and  $\chi(\text{Eu}) = 1.75$ , the Eu-O CTB position should be at  $42000 \text{cm}^{-1}$ , i. e. at about 238nm.

However, H.E. Hoefdraad [54] has shown that the position of CTB of  $\text{Eu}^{3+}$  in the absorption spectra is more or less fixed in octahedral VI coordination and that it varies in VIII and XII coordinations as a function of the effective ionic radius of the relevant lattice ion. The CTB position from actual PL measurements is centered at 250nm [55] A review on behavior of charge transfer energies in trivalent rare earths, is given in [56]

## 2.4 $\text{Gd}_2\text{O}_3$ Properties

Rare earths (RE) sesquioxides ( $\text{RE}_2\text{O}_3$ ) have been of great scientific and technological interest because of their attractive physical and chemical properties. Actually, these oxides are excellent host materials for powerful lasers or improved phosphors and, considering their high thermal stability and toughness, they can also be used as refractory or abrasive materials. These materials are also considered highly active catalysts for a large number of organic reactions, like the oxidation coupling of methane to form higher hydrocarbon products or the dehydration/dehydrogenation of alcohols. Moreover, some RE sesquioxides are becoming the focus of industrial attention due to their potential use as control rods for nuclear reactors [57]. In particular the  $\text{Gd}_2\text{O}_3$ , an insulator sesquioxide, when activated by  $\text{Eu}^{3+}$  or  $\text{Nd}^{3+}$ , is an effective crystal phosphor that presents cathode-luminescence and laser action, respectively. Moreover, it has been proposed as potential material for immunoassays and biosensing applications [14,].

## 2.4.1 Crystal structure

In general, RE-sesquioxides present polymorphic behavior. Three structures are commonly found: hexagonal, monoclinic and cubic, denoted as A, B and C, respectively (figure 2.12). The C-form structure, cubic bixbyite type, is known as the low-temperature form at ordinary pressures. Particularly, the polymorphic transition from cubic to monoclinic phase occurs at temperatures of 1250°C or higher (figure 2.12) [8].

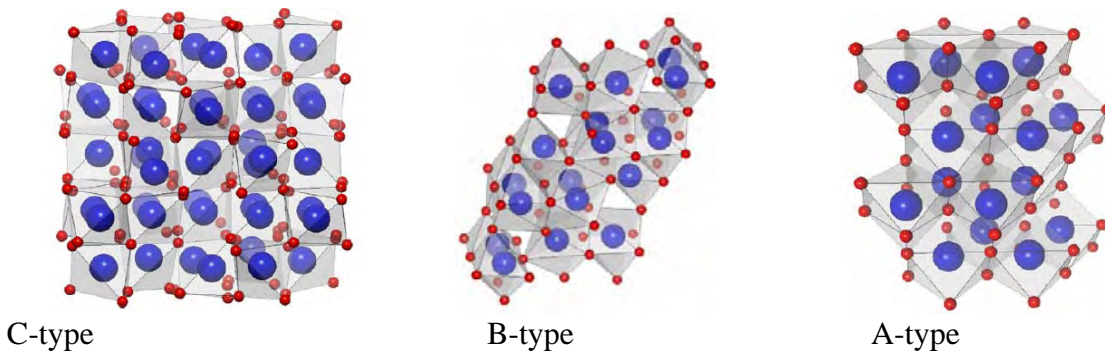


Figure 2.12 Polyhedral representations of the cubic C-type (cubic), B-type (monoclinic) and A-type (hexagonal) structure of  $\text{RE}_2\text{O}_3$ . The large and small spheres stand for RE and O atoms, respectively.

$\text{Gd}_2\text{O}_3$  has the bixbyite structure (space group  $Ia\bar{3}-T_h^7$ ) with a lattice constant of 10.813Å. [58] There are two unique cation ( $\text{Gd}^{3+}$ ) positions due to the ordered arrangement of the oxygen atoms. There are 3 times as many of the as called 24d sites, with twofold rotational symmetry ( $C_2$ ), as 8b sites, with threefold rotary inversion symmetry ( $S_6$  or  $C_{3i}$ ). [59] These sites are conveniently described by considering the cation surrounded by anions occupying six corners of a cube, as shown in figure 2. 14.

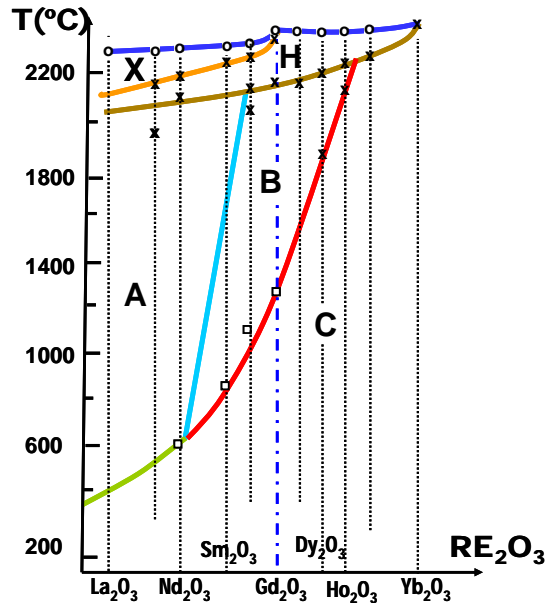


Figure 2.13 Structure of  $RE_2O_3$  related to the atomic number and to the temperature, at room pressure. In general three structures can be stable at  $T < 800^\circ C$ : A-hexagonal, B-monoclinic, C-cubic. [8]

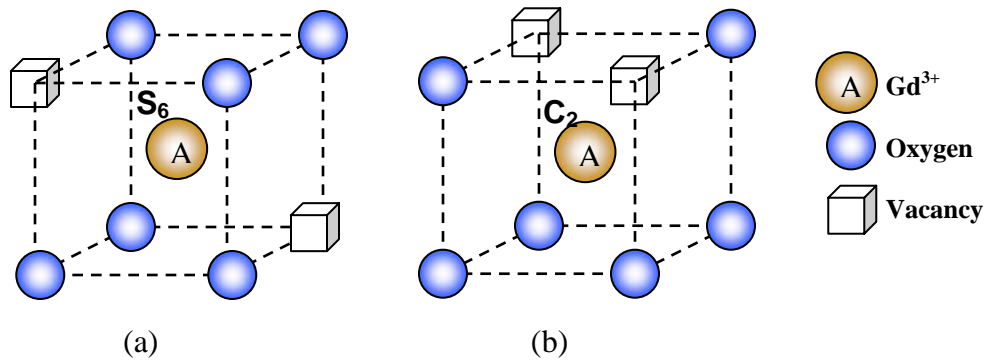


Figure 2.14 The two cation sites of cubic bixbyite. (a)  $8b$  ( $S_6$  or  $C_{3i}$  symmetry) and (b)  $24d$  ( $C_2$  symmetry).

For the  $24d$  site, the unoccupied positions are on opposite corners of one cube face, while for the  $8b$  site, the unoccupied positions are diagonally opposed. Furthermore, the  $24d$  coordination cube is distorted, with three distinct metal-oxygen distance pairs (conversely for the  $8b$  site, the six metal-oxygen distances are equal). The  $24d$  distortion originates

when the oxygen atoms beneath the unoccupied positions are displaced toward the vacant sites, thereby increasing the O-Gd-O angle so that it is the largest angle in the coordination cube [59].

#### **2.4.2 Quantum effects in RE-doped nanostructures**

Nanocrystals have attracted a lot of attention in the last 20 years [60], but only recently nanocrystals composed of wide band gap insulator materials have started to be studied [1]. At first some extraordinary results were pointed out (huge shortening of the lifetime, high increase of the photoluminescence yield, etc), but such results could not be reproduced. Since many interesting results have been obtained on semiconductors, was natural to try and see whether a similar behavior can be obtained for wide band gap insulators. Consequently, in the last years the attention has been focused on the evaluation of quantum confinement effects in such materials. However, since insulators are generally strongly ionic, confinement effects are expected to be low. Indeed has been showed that quantum confinement effects on the gap of a material such as  $Gd_2O_3$  can be observed but are quite weak [16,17]. In contrast, the exciton Bohr radius of II-VI semiconductors is larger resulting in pronounced quantum confinement effects for nanocrystals of about 2.5nm and smaller. Therefore, quantum size effects on the luminescence properties of RE ions should only be expected in II-VI host semiconductor nanocrystals [15].

## CHAPTER III: PREVIOUS RELATED WORKS

### 3.1 Introduction

In general, functional doping of a nanomaterial requires that the dopant ions substitute metal ions of the host lattice, i.e., that they occupy lattice sites of the host metal ions. Similar to electrical doping, the term optical doping is used to describe the incorporation of centers in a host material to enhance and/or tailor its optical properties. A well known example of optical doping is the phosphor technology that is used in a large number of lighting and display applications. Optical doping is also very important in optoelectronics, a technology that forms the basis for components such as semiconductor lasers, optical discs, image sensors, or optical fibers. With optical doping it is possible to enhance both the emission and absorption characteristics of a material.

As was above mentioned, in cubic  $\text{Eu}^{3+}$ -doped  $\text{Gd}_2\text{O}_3$ ,  $\text{Eu}^{3+}$  ions occupy two kinds of lattice sites after substituting the  $\text{Gd}^{3+}$  ions (Figure 3.1). These sites are sixfold-coordinated distinctly non equivalent with  $\text{C}_2$  and  $\text{S}_6$  point symmetry, and which differ from each other in the position of  $\text{RE}^{3+}$  ion relative to the vacancy oxygen, as was described above. It has been established [61] that the presence of inversion symmetry in the  $\text{RE}^{3+}$  site drastically affects the luminescence spectra of the  $\text{RE}^{3+}$ -doped materials.

On the other hand, due to nearly identical radii ions, 0.94Å for  $Gd^{3+}$  and 0.95Å for  $Eu^{3+}$ , the lattice distortion in  $Eu^{3+}$ -doped  $Gd_2O_3$  is insignificant [62] and, unlike in  $Y_2O_3$ , where pairs of neighboring  $Eu^{3+}$  ions leads to slight distortions in crystal field, in  $Gd_2O_3$  the mutual proximity of the  $Eu^{3+}$  ions has no effect [63], since  $Eu^{3+}$  and  $Gd^{3+}$  have nearly the same size [4], which allows an unambiguous analysis of the transfer process.

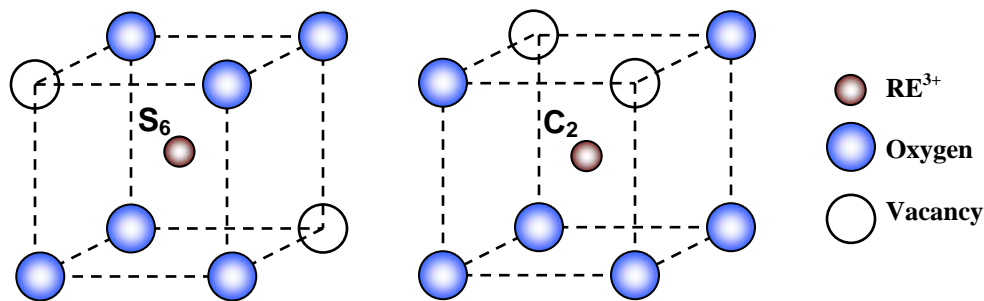


Figure 3.1 Schematic presentation of the  $RE^{3+}$  coordination in the  $S_6$  and  $C_2$  sites of cubic (C-type) sesquioxide.

As mentioned before, the large discrepancy between the size of host Zn species and dopant RE species makes the actual incorporation of RE ions into the ZnO lattice a controversial subject. If one assumes that the RE ion is incorporated on a  $Zn^{2+}$  lattice site, the ZnO host lattice has to deform locally. In addition, the 3+ charge of a RE ion on a 2+ site has to be compensated somehow in the host lattice. Finally, the differences in chemical properties between  $Zn^{2+}$  and  $RE^{3+}$  will not favor substitution of  $Zn^{2+}$  by  $RE^{3+}$  species [15,64].

In this chapter, some previous works on properties of  $Eu^{3+}$ -ZnO and  $Eu^{3+}$ - $Gd_2O_3$  nanostructures, which are matter of study in this thesis, are briefly reviewed.

### 3.2 The $\text{Eu}^{3+}$ - ZnO system

Using the Pechini's method and subsequent thermal treatment, Lima et al., [65] synthesized spherically shaped particles of ZnO with an average particle size of 500nm and determined the corresponding luminescence properties. According to the authors, the excitation spectra monitoring the emission of  $\text{Eu}^{3+}$  at 612nm (figure 3.2-a), presented one band at 376nm attributed to transition from valence band to conduction band ( $\text{VB} \rightarrow \text{CB}$ ), characteristic of ZnO, and two peaks at 395 and 464nm attributed to  ${}^5\text{D}_0 \rightarrow {}^7\text{F}_j$  and  ${}^7\text{F}_0 \rightarrow {}^5\text{D}_2$  transitions from the  $\text{Eu}^{3+}$  ion. For the excitation at 376nm, a wide band centered at 525nm and a lower intensity band in the red region were observed (Figure 3.2-b). The authors attributed this emission band to decay from electronic defects, which are present in the forbidden band, to the VB or between different levels into forbidden band. However, the assignment of this band is yet misleading in the literature. When this system was excited at 465nm, the emission spectrum (Figure 3.2-b) shown the  ${}^5\text{D}_0 \rightarrow {}^7\text{F}_j$  ( $J=0-4$ ) transitions, and after the authors, the feature and the high intensity of the hypersensitive transition  ${}^5\text{D}_0 \rightarrow {}^7\text{F}_2$  indicate that  $\text{Eu}^{3+}$  ion occupies a low symmetry site. Exciting at 395nm, both the contributions of ZnO transitions and the combined emission spectrum of ZnO and  $\text{Eu}^{3+}$  ions have been observed (Figure 3.2-b). From their PL results, the authors concluded that there is no energy transfer between ZnO and  $\text{Eu}^{3+}$  ion, which probably is due to the difference of energy levels. Moreover, based on PL measurements at 77K the same authors claimed that  $\text{Eu}^{3+}$  ions occupy at least three different sites in ZnO:Eu 3% samples. It was proposed that  $\text{Eu}^{3+}$  incorporated in the structure should have stabilized  $\text{Zn}^+$  through a charge compensation mechanism [6].

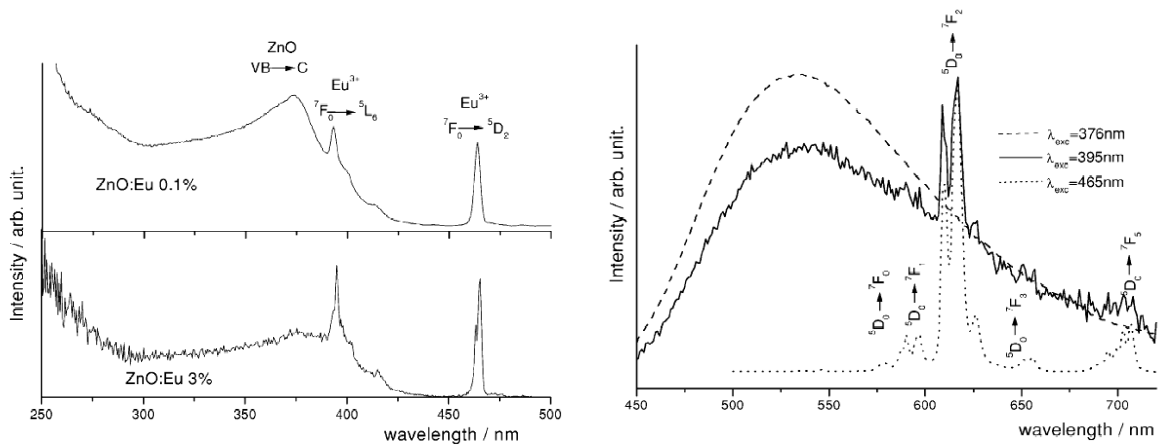


Figure 3.2 (a) Excitation spectra of ZnO:Eu 0.1 and 3 at% monitored at 612 and 616 nm, respectively, and (b) Photoluminescence spectra of ZnO:Eu 3at% obtained at different excitation wavelengths at room temperature [6].

Based on PL measurements, Zhang et al. [6] claimed the existence of energy transfer from the host Zn ions to  $\text{Eu}^{3+}$  in Eu-doped ZnO nanocrystalline powders synthesized by high temperature calcination method. In this work, the samples were prepared by mixing  $\text{Eu}_2\text{O}_3$  with  $\text{LiNO}_3$  and ZnO with a small amount of ethanol. The  $\text{Eu}^{3+}$  and  $\text{Li}^+$  concentrations in ZnO were between 0.1mol% and 1mol%. After drying, the mixture was grounded and sintered in air for four hours at  $900^\circ\text{C}$ . The XRD patterns reported by the authors (figure 3.3) shows that the peaks in the pattern sample with 1mol%  $\text{Eu}^{3+}$  shifts to large angle, compared to 0.5mol%, which would indicate a decreasing of lattice parameters, which in turn would indicate a decreasing of lattice parameter of host ZnO. However, this fact was not explained.

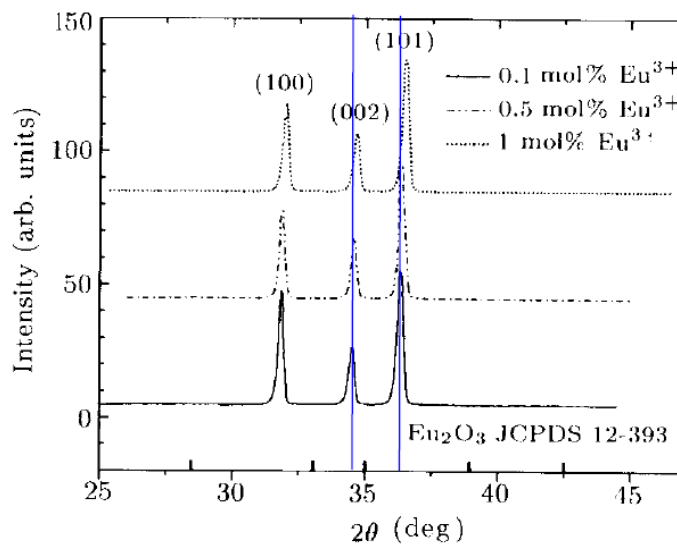


Figure 3.3 XRD patterns of ZnO:Eu nanopowders with different  $\text{Eu}^{3+}$ -doping concentrations. A It can be seen that the peaks in the pattern sample with 1mol%  $\text{Eu}^{3+}$  shifts to large angle, compared to 0.5mol%. [6]

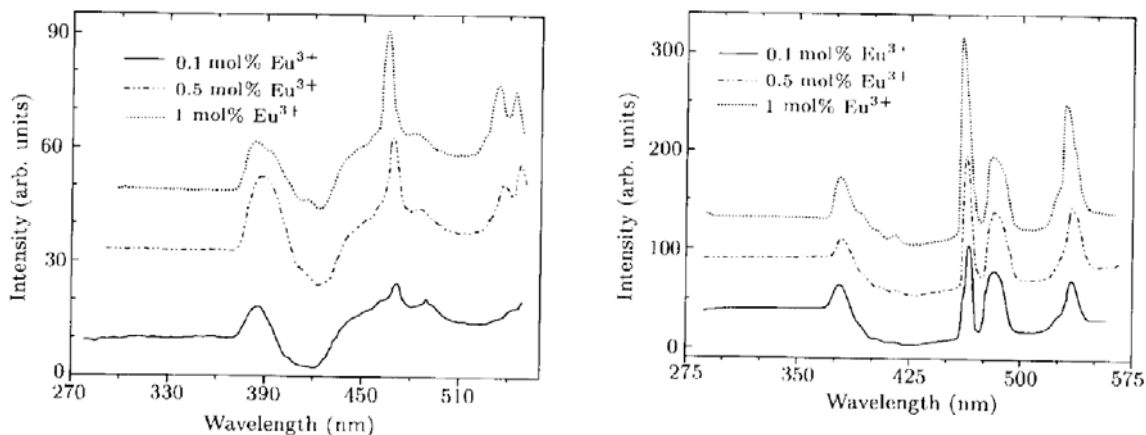


Figure 3.4 Excitation spectra of ZnO:Eu nanopowders under monitoring wavelength at (a) 708nm and (b) 616nm [6].

The excitation spectrum, under monitoring the  $\text{Eu}^{3+}$  ions luminescence at wavelengths of 708nm and 616nm, consisted of a strong band corresponding to ZnO host (385nm) and the characteristic excitation line spectrum of  $\text{Eu}^{3+}$  species (figure 3.4). Furthermore, only

$\text{Eu}^{3+}$  emissions, without the broad emission for ZnO, were observed under band-gap excitation at 385nm. Surprisingly, the red shift observed in the band-gap absorption was comparable to that of the ZnO bulk (~370 nm). This fact would be in contrast to the blue-shift that should be expected because of the quantum confinement effect in nanosize crystals. The same work reported a shift toward larger angles in the XRD peaks of the 'doped' solids, which would indicate the reduction in the host ZnO lattice parameter. No explanation on this fact was offered by the authors. In the same work, the luminescence intensity was increased by rising the  $\text{Eu}^{3+}$  concentration from 0.1mol% to 10.1mol%, no matter whether UV excitation or the characteristic excitation of  $\text{Eu}^{3+}$  was adopted.

More recently, Ishizumi and Kanemitsu [5] have studied the PL properties of  $\text{Eu}^{3+}$  doped ZnO nanorods fabricated by a microemulsion method. The average lengths of the long and short axes of nanorods were 500 and 50 nm, respectively. The PL of bound exciton recombination and the typical broad band were observed near 370nm and 650nm under 325nm light excitation; however, no emission of  $\text{Eu}^{3+}$  was detected (Figure 3.5). The broad band around 650nm, which is similar to that of  $\text{Eu}^{2+}$  due to the f-d transitions [25], was attributed to defects in ZnO nanorods. When the 405nm and 465.8 nm excitation lights were used, which almost coincide with the energies of the  ${}^7\text{F}_0\text{-}{}^5\text{D}_3$  (410nm) and  ${}^7\text{F}_0\text{-}{}^5\text{D}_2$  (464nm) respectively, the sharp peaks of the intra-4f transitions of  $\text{Eu}^{3+}$  ions were clearly observed. The broad PL band related to defects of ZnO nanorods was also observed.

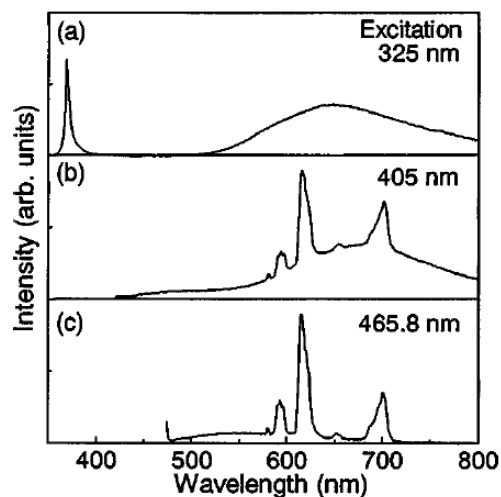


Figure 3.5 PL spectra of ZnO:Eu nanorods at 15K. In spectrum (a) the band around 650nm was assigned to ZnO emission, whereas in spectra (b) and (c) the sharp peaks due to 4f-transitions from  $\text{Eu}^{3+}$  ions were clearly observed [5].

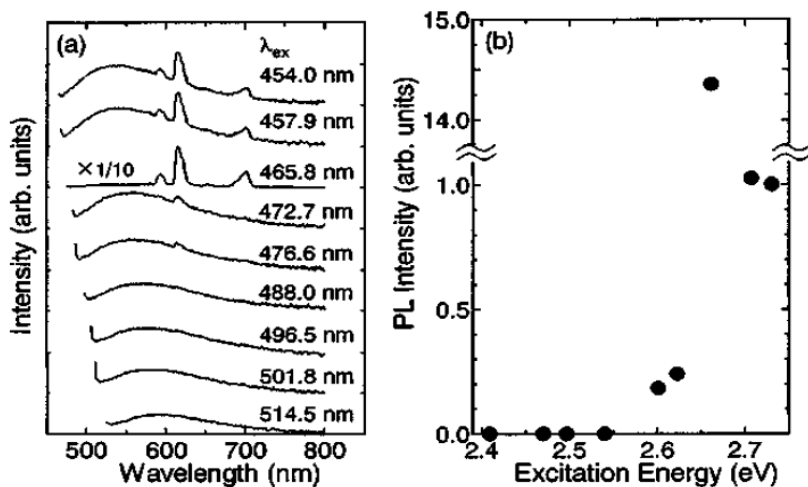


Figure 3.6 (a) PL spectra of ZnO:Eu nanorods at different excitation wavelengths at 15 K. (b) Excitation energy dependence of the  $\text{Eu}^{3+}$ -related PL intensity in ZnO:Eu nanorods [5].

Sharp PL peaks corresponding to the intra-4f transitions of  $\text{Eu}^{3+}$  ions were detected under non-resonant excitation below the band-gap energy value of ZnO (454nm and 457.9 nm). These peaks were observed in addition to the one corresponding to the direct excitation

$^5D_2$  (465.8 nm). According to the same authors, the observation of red emission under non-resonant 2.70 eV and 2.73eV excitation suggested that the excited state of  $\text{Eu}^{3+}$  ions was caused by energy transfer from the host ZnO nanorod to  $\text{Eu}^{3+}$  ions. However, the blue shift of broad band as changing wavelength excitation (figure 3.6-a) is not explained. Since the intensities of these excitation energies (figure 3.6-b) were lower than the band-gap energy of ZnO, the energy transfer from ZnO nanorods to  $\text{Eu}^{3+}$  ions was attributed to the defects in ZnO nanorods.

Liu et al. used a modified sol-gel method to synthesize hexagonal  $\text{Eu}^{3+}:\text{ZnO}$  nanocrystals [7]. In this approach, the precursor solution was hydrolyzed by the addition of LiOH. The obtained precipitates were annealed at 400°C in air for 1h to enhance their crystallinity and luminescence. Additionally the crystallite size was increased from 3nm to 9nm. Site-selective spectroscopy measurements at 10K, suggested the probable energy transfer from the host species to  $\text{Eu}^{3+}$ . Based on this result, the authors suggested the actual incorporation of  $\text{Eu}^{3+}$  ions into the ZnO crystal lattice. On this basis, two  $\text{Eu}^{3+}$  sites were identified. One site was ascribed to an inner site within an ordered and crystalline environment; the other site was associated to the distorted lattice sites near the surface (figure 3.7).

Recent studies also suggested that particle morphology would also exert a remarkable influence on the optical properties of  $\text{ZnO}:\text{Eu}^{3+}$  nanostructures [69]. Eu-doped ZnO (1.0% mol) was synthesized through three solution-based approaches: in presence of

starch, emulsion-mediated synthesis and hydrothermal methods. Spherical, hexagonal and nanorod shaped ZnO structures, respectively, were obtained. Based on PL measurements, the authors claimed that energy transfer from ZnO nanocrystals to the  $\text{Eu}^{3+}$  apparently took place only in hexagonal shaped nanocrystals.

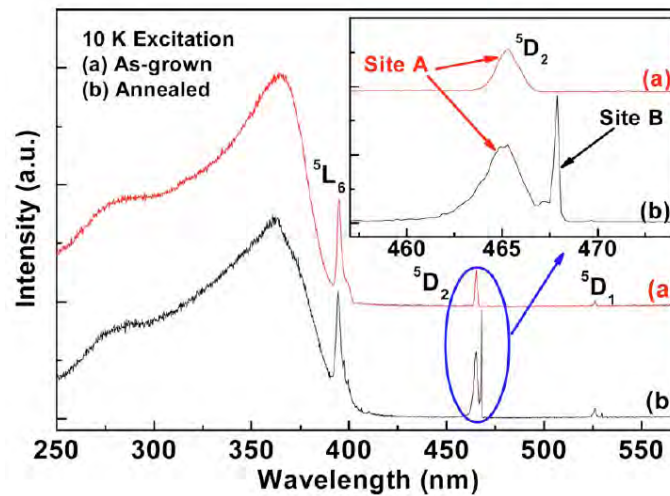


Figure 3.7 Excitation spectra of  $\text{Eu}^{3+}:\text{ZnO}$  nanocrystals by monitoring the  ${}^5\text{D}_0 \rightarrow {}^7\text{F}_2$  emission at 10 K, with (a)  $\lambda_{\text{mon}}=615.4\text{nm}$  for the as-grown sample, and (b)  $\lambda_{\text{mon}}=616.6\text{nm}$  for the annealed sample [7].

From the literature reviewed, it is obvious that conclusive evidence about the effective incorporation of the Eu in the ZnO still not exist. In the same way, the luminescent properties of ZnO pure, or containing Europium, are strongly dependent of the method and conditions synthesis. Therefore, in this work, the possible incorporation of  $\text{Eu}^{3+}$  ions, and its effect on structural, optical and luminescent properties of ZnO are investigated.

### 3.3 The $\text{Eu}^{3+}$ - $\text{Gd}_2\text{O}_3$ system

Using the sol-gel method, Lin *et al.* [24] prepared nanocrystalline powders of Eu-doped  $\text{Gd}_2\text{O}_3$  with concentrations of Eu in the 3-15 mol% range. From  $\text{GdCl}_3$  and  $\text{EuCl}_3$ , as precursor salts, while water D.I. and  $\text{NH}_4\text{OH}$  were used as solvent and chelating agent, respectively. The mixture of Gd and Eu hydroxides obtained was calcinated between  $800^\circ\text{C}$  and  $1100^\circ\text{C}$  for 2h. In this work, the effect of Eu/Gd composition ratio and calcination temperature on the structure and luminescent properties were investigated. From their XRD measurements the authors report that pure crystalline phase  $\text{Gd}_2\text{O}_3$  can be formed at temperatures above  $900^\circ\text{C}$ , while at  $800^\circ\text{C}$  both phases  $\text{GdO}_2$  and  $\text{Gd}_2\text{O}_3$  coexisted. The crystallite sizes were 12, 21, 34 and 24nm for calcinations temperatures of 800, 900, 1000 and  $1100^\circ\text{C}$ , respectively. TEM analyses revealed the following particle size distributions for different calcinations temperatures: 50-120nm ( $800^\circ\text{C}$ ), 80-140nm ( $900^\circ\text{C}$ ), 80-180nm ( $1000^\circ\text{C}$ ) and 90-200nm ( $1100^\circ\text{C}$ ). The discrepancy between estimated XRD crystallite sizes and TEM size was attributed to aggregation of particles. Regarding the luminescent properties, the authors found that, monitoring the emission at 612nm, and after calcining the intermediates at temperatures above  $800^\circ\text{C}$  the excitation spectra exhibited a wide band about 254nm, assigned to  $\text{O}^{2+} \rightarrow \text{Eu}^{3+}$  Charge Transfer Band (CTB). The intensity of the excitation peak was increased by increasing the calcination temperature up to  $1000^\circ\text{C}$ . A further increase in the temperature was conducive to the drop in the corresponding peak intensity. This fact was not discussed by the authors. Also, a weak and broad peak at 312nm, related to  $\text{Gd}^{3+}$  transitions, was observed. These transitions were caused by the  $\text{Gd}^{3+} \rightarrow \text{Eu}^{3+}$  energy transfer mechanism. In the emission

spectra, the maximum intensity was shown in those samples treated at 1000°C and was attributed to the enhanced crystallinity achieved at such temperature. The effect of the concentration of  $\text{Eu}^{3+}$  ion was investigated in powders calcined at 1000°C; the optimum doping level was determined as 7% w/w. The decreasing in the PL emission intensity, for higher concentrations, was attributed to the concentration quenching phenomena, which was described in the earlier section of this thesis.

M. Pires et al. [19] produced Eu-doped Gadolinium oxide by the precipitation method. The influence of  $\text{Eu}^{3+}$  concentration on optical and morphological properties was investigated. Non crystalline monohydrate gadolinium basic carbonate bare and doped with 1 to 5 at.% of europium were obtained as precursor. The precursors were annealed at 750°C for 4h, under argon continuous flow. Although the authors claimed the cubic phase was obtained, no evidence on crystallinity quality and lattice parameter values were discussed within the paper. SEM analyses revealed the presence of particles with an average diameter in the 110-150nm range, irrespective of the concentration of the dopant species. The same reference proposed that doping species should have been located on the particle surface inhibiting particle growth after nucleation. Luminescence spectroscopy measurements showed a pronounced CTB centered around 250nm was observed. The intensity of this CTB was found to increase by rising the  $\text{Eu}^{3+}$  concentration. It was also observed weak peaks up to 330nm, related to internal  $\text{Gd}^{3+}$  f-f transitions. These peaks became noticeable because of the  $\text{Gd}^{3+} \rightarrow \text{Eu}^{3+}$  energy transfer. Similar trend on the luminescence intensity was observed at higher fractions of Eu,

indicating the absence of concentration quenching at least for the considered interval of concentrations, which was explained for the authors, considering that the doping ion distribution in the surface of oxide samples does not achieved the minimum distance necessary to cause energy transfer between emission centers.

G. Liu, et al., [18], prepared spherical and submicrometer-sized hollow  $\text{Gd}_2\text{O}_3:\text{Eu}^{3+}$  phosphors by homogeneous precipitation and hydrothermal crystallization techniques. The report considered the variation of dopant concentration and modification of the synthesis conditions as follows: in the precipitation step, spherical nucleus were formed and allowed to grow. In the subsequent hydrothermal step, large particles were crystallized.  $\text{Gd}_2\text{O}_3:\text{Eu}^{3+}$  phosphors were obtained by annealing those products from the hydrothermal stage at different temperatures (550-850°C) for 2h in air. It was found that the crystals morphology was strongly dependent on the reactants concentration and aging time. Depending on those conditions, rods and solid or hollow spheres were obtained. The XRD pattern for the precursor showed the presence of sharp peaks that were attributed to  $\text{Gd}_2(\text{CO}_3)_3 \cdot x\text{H}_2\text{O}$ . Moreover, the authors claimed that the samples annealed at 600°C exhibited the pure cubic phase. The diffraction peaks became sharper when the solids were produced at higher annealing temperatures. However, from their FT-IR results, in addition to Gd-O bond peak ( $553\text{cm}^{-1}$ ), the presence of -OH group ( $3410\text{cm}^{-1}$ ) and  $\text{CO}_3^{2-}$  anion ( $1508$  and  $1429\text{cm}^{-1}$ ) bands were evident, which suggested an incomplete conversion of the precursors into the anhydrous oxide phase. The corresponding luminescence measurements (the excitation spectra were monitored by

using the 610nm line) revealed an intense band at 260nm that was attributed to the CTB and whose intensity increases as the annealing temperature increases. Furthermore, the weak lines observed at 279nm and 310nm were related to internal  $Gd^{3+}$  f-f transitions ( $^8S-^6I$ ) and ( $^8S-^6P$ ) indicating an effective energy transfer from  $Gd^{3+}$  to  $Eu^{3+}$ . The authors reported that the obtained spherical  $Gd_2O_3:Eu^{3+}$  phosphors had better red luminescence properties, and that the relative luminescence intensity and the lifetime increased with increasing annealing temperatures (figure 3.8). Moreover, they considered that, because with the increasing the annealing temperature, the crystallinity becomes better, and the impurities such as  $-OH$ ,  $CO_3^{2-}$  decrease, the quenching of the luminescence of  $Eu^{3+}$  by the vibrations of these impurities decreases, resulting in the increase of the lifetime of  $Eu^{3+}$ .

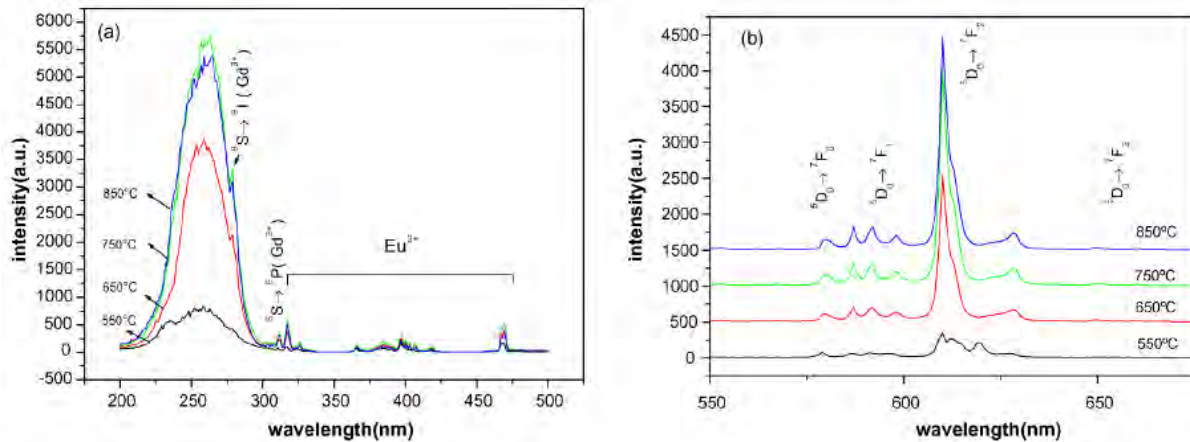


Figure 3.8 Excitation (a) and emission (b) spectra of samples calcined at different temperatures [18].

Ch.S. Park, et al. [66], synthesized nanoparticles of  $Gd_2O_3:Eu^{3+}$  by a liquid-phase reaction method using hydrated acetate as the precursor salts. They Investigated the

influence of  $\text{Eu}^{3+}$  content (in the range of 5-15wt%,) on the optical properties of phosphors. After synthesized, the precursors were treated at  $600^\circ\text{C}$  for one hour and under oxygen atmosphere (2L/min). The XRD analyses reported that, regardless of the europium content, all solids crystallized in the cubic  $\text{Gd}_2\text{O}_3$  structure even at a temperature as low as  $600^\circ\text{C}$ . The average crystallite size was estimated in the range 21-41 nm. The largest sizes corresponded to the phosphor with 10wt%  $\text{Eu}^{3+}$ . The apparent relationship between composition and average crystallite size was not discussed by the authors.

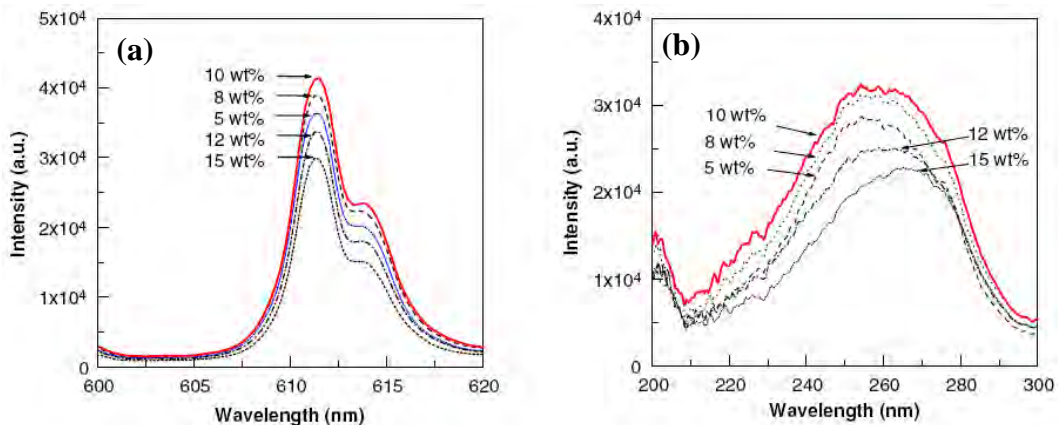


Figure 3.9 (a) Emission (excitation at 254nm) and (b) excitation (monitoring 611nm) spectra of  $\text{Gd}_2\text{O}_3:\text{Eu}^{3+}$  phosphors having different concentrations. [66]

In the same work, the excitation spectra shown in figure 3.8-b, for 611nm emission, consisted of a large band with a maximum at 254nm. This band was assigned to CTB. In these spectra, the maximum intensity was observed for the 10wt% Eu-doped  $\text{Gd}_2\text{O}_3$ . The CTB was shifted towards longer wavelengths (265nm) for the 15wt% Eu-doped  $\text{Gd}_2\text{O}_3$  phosphor. Typical peaks for internal  $\text{Gd}^{3+}$  f-f transitions were no mentioned within the

manuscript. Similarly, when the phosphors were excited by UV light of 254nm (CTB), only the main emission peak (detected at 611nm) was reported. The authors found that the phosphors showed an initial increase in luminescence and then a subsequent decrease with further doping (above 10wt%), which was attributed to the previously discussed concentration quenching effect.

Phosphor particles of Eu-Gd<sub>2</sub>O<sub>3</sub> with were synthesized by Y.C. Kang, et al. [67], by a continuous spray pyrolysis method. The effects of process temperature (800-1600°C) and Eu content (2-12at.%) on PL, morphology and crystallinity of the products, were investigated. Unlike normal spray pyrolysis methods, no milling was applied to powders. The mean size of the particles increased from 0.35 to 1.2 μm when the solution concentration was increased from 0.02 to 1M. The particles prepared at 800°C exhibited sharp XRD peaks corresponding to cubic Gd<sub>2</sub>O<sub>3</sub>. The crystallinity of the cubic phase was increased by rising the process temperature up to 1400°C. A transition from highly crystalline cubic to poorly crystalline monoclinic phase was observed at 1600°C, which was higher than the 1250°C previously reported for Gd<sub>2</sub>O<sub>3</sub> [8]. This discrepancy with expected transition temperature was explained in terms of the short residence time of the particles inside the hot wall reactor. The average size of the particles increased from 0.35 to 1.2μm when the solution concentration was increased from 0.02 to 1M; nevertheless, the effect of process temperature on crystal nor particle size was no reported. The Eu-Gd<sub>2</sub>O<sub>3</sub> particles absorbed excitation energy in the range between 220 nm and 300 nm, with a maximum excitation wavelength around 255nm. The optimum brightness was

obtained at a doping concentration of 10at.%, while the maximum PL intensity was observed in the sample annealed at 1400°C, (the main peak emission was at 612nm in both cases.) In turn, the particles prepared at 1600°C, showed two main emission peaks at 615 and 624nm and much lower intensity than for other samples synthesized at lower temperatures (between 1000 and 1400°C), as shown figure 3.10.

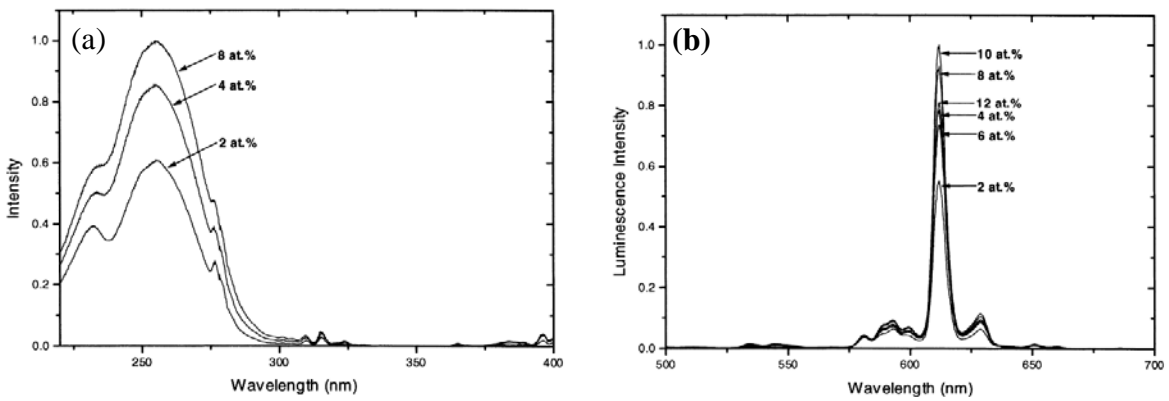


Figure 3.10 Excitation (a) and emission (b) spectra of Gd<sub>2</sub>O<sub>3</sub>:Eu particles at different doping concentrations, prepared at 900°C [67].

On the other hand, A. Garcia-Murillo, et al. [68] synthesized Eu<sup>3+</sup>-doped Gd<sub>2</sub>O<sub>3</sub> thin films by sol-gel method. In this work, used Gd(III) isopropoxide and Eu(III) nitrate pentahydrate were used as precursors. The solution was prepared under argon flux and deposited on pure silica substrate by di-coating in a glove box under argon controlled atmosphere. The authors found that films present waveguiding properties and the crystallization in the cubic phase occurs at 700°C, but no preferential orientation was observed. Also, after annealing at 1000°C very dense films were obtained with a refractive index of 1.88 at 632.8nm. Their PL studies revealed that the thin films

synthesized have the same sharp emission bands as  $\text{Eu}^{3+}$ -doped  $\text{Gd}_2\text{O}_3$  powders produced by solid state reaction method, corresponding to the  ${}^5\text{D}_0 \rightarrow {}^7\text{F}_J$  ( $J=0$  to 4). After the authors, these bands of cubic phase appear at  $700^\circ\text{C}$  by sol-gel process although with conventional method they become visible only after  $900^\circ\text{C}$ , but explain this fact.

It is evident from the reviewed literature that, due to the potential applications in various fields, the study of  $\text{Eu}^{3+}$ -doped  $\text{Gd}_2\text{O}_3$  nanostructured is matter of intense research, in order to search up its better properties. However, nevertheless the actual incorporation of Eu ions into  $\text{Gd}_2\text{O}_3$  structure has been demonstrated, phenomena like the concentration quenching are strongly dependent of the methods and conditions of synthesis. In addition, it is clear that the luminescent properties of this material are strongly dependent on method and condition synthesis. Therefore, in this work, the effect of  $\text{Eu}^{3+}$  content and annealing temperature on the structural, luminescent and magnetic properties of  $\text{Gd}_2\text{O}_3$  nanoparticles; and the effect of  $\text{Eu}^{3+}$  on structural, optical and luminescent properties of  $\text{Gd}_2\text{O}_3$  thin films are studied.

## CHAPTER IV: EXPERIMENTAL DETAILS

### 4.1 Synthesis of nanocrystalline ZnO in presence of $\text{Eu}^{3+}$ ions

#### 4.1.1 The sol-gel approach

##### *i. Materials*

$\text{Zn}(\text{C}_2\text{H}_3\text{O}_2)_2$  (99.99%, Aldrich) and  $\text{Eu}(\text{C}_2\text{H}_3\text{O}_2)_3 \cdot \text{XH}_2\text{O}$  (99.9%, Alfa Aesar) were used as precursor materials. 2-ethylhexanoic acid (boiling point  $227^\circ\text{C}$ , viscosity at  $20^\circ\text{C}$ ,  $7.5\text{mPa}\cdot\text{s}$ ; 98%, Alfa-Aesar), was selected as solvent. All reagents were used as received without any further purification. No additional chelating agent was used.

##### *ii. Experimental procedure*

First, suitable amounts of Zn(II) and Eu(III) acetates were dissolved separately in 2-ethylhexanoic onto a hotplate at  $200^\circ\text{C}$ . The weights of each precursor salt were calculated to give the desired atomic fractions of Eu, 'x', in  $\text{Zn}_{1-x}\text{O}:\text{Eu}_x$  stoichiometry. The 'x' values varied between 0.05 and 0.30. Obtained solutions were then mixed for 10 min. Next, the solvent was eliminated by heating the solution at  $200^\circ\text{C}$  for 72h until complete dryness. As-synthesized solids were pulverized in an Agate mortar and submitted for characterization. Figure 4.1 summarizes the synthesis procedure.

#### 4.1.2 The Ethanol route

##### *i. Materials*

As in the previous section,  $\text{Zn}(\text{C}_2\text{H}_3\text{O}_2)_2$  (99.99%, Aldrich) and  $\text{Eu}(\text{C}_2\text{H}_3\text{O}_2)_3 \cdot \text{XH}_2\text{O}$  (99.9%, Alfa Aesar) were used as precursors and anhydrous ethanol (98%, Alfa-Aesar) as solvent. Ethanol was selected not only as solvent but also due to its dehydrating

properties. We modified the ZnO synthesis methods proposed by Spanhel *et al.*, [69], and synthesized the ZnO nanocrystals, pure and doped, under room temperature conditions [70]. A LiOH monohydrate (98%) solution in ethanol was used as precipitating agent. In order to recover the products, n-heptane (98%, Fisher) was used as coagulating agent.

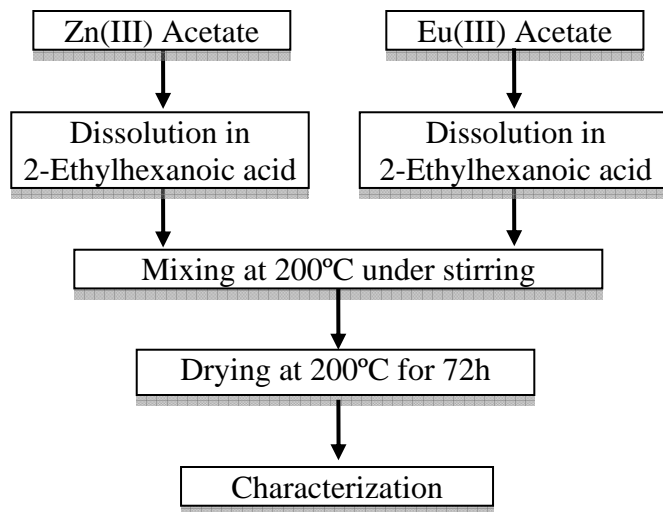


Figure 4.1 Flow diagram of the sol-gel process for synthesis of  $Zn_{1-x}O:Eu_x$  nanopowders.

### *ii. Experimental procedure*

Required amounts of acetate salts of Zn(II) and Eu(III) to give the desired atomic fraction of Eu ions, 'x' ( $x = 0.05-0.30$ ), were dissolved by careful heating in anhydrous ethanol at 65°C to obtain a 0.1 M solution. This solution was refluxed for 2h to assure complete dissolution of the precursor salts. A suitable amount of LiOH was dissolved by sonication in ethanol to get a 0.14M solution. The LiOH solution in ethanol was added dropwise into the Zn/Eu solution (with suitable atomic fraction of Eu ions, 'x') and mixed under vigorous stirring for 10 minutes (contact time). Nanocrystals were recovered by coagulation-dispersion cycles (two times) using n-heptane and resuspended in fresh

ethanol. The recovered solids were dried at 50°C for 12h and submitted for characterization. Figure 4.2 shows the corresponding experimental procedure.

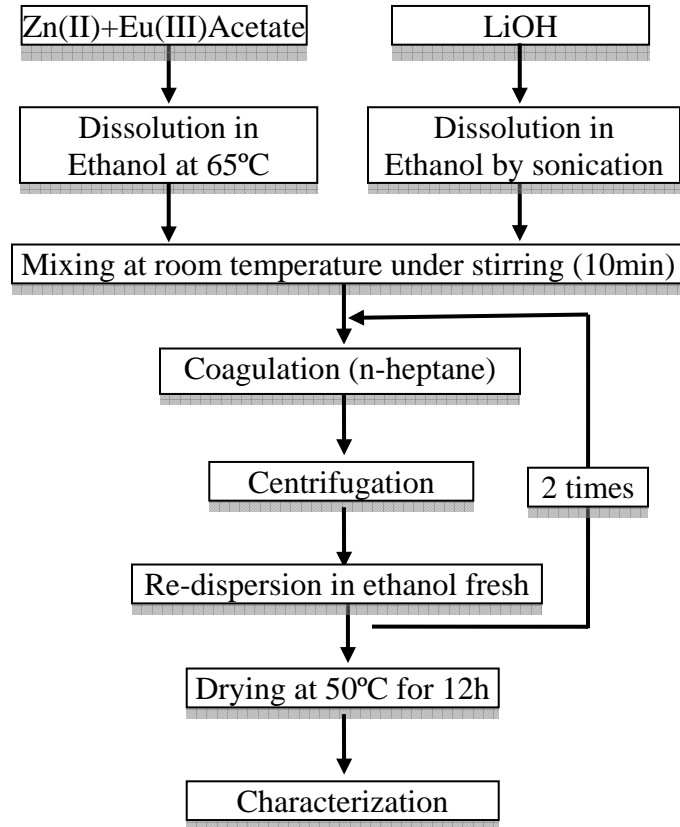


Figure 4.2 Flow diagram of the modified sol-gel method (ethanol route) of  $Zn_{1-x}O:Eu_x$  nanocrystals.

#### 4.2 Synthesis of nanostructured Eu-doped $Gd_2O_3$

The synthesis of Eu-doped Gadolinium oxide was attempted by a modified version of sol-gel method where no chelating agent was added to the obtained solutions. The solid products were obtained as powders and also as thin films deposited onto fused quartz substrates.

#### **4.2.1 Synthesis of nanocrystalline Eu-doped Gd<sub>2</sub>O<sub>3</sub> powders**

##### ***i. Materials***

Hydrated acetates of Gd(III) and Eu(III) (99.9%, Alfa Aesar) were used as precursor salts. 2-ethylhexanoic acid (boiling point 227°C, viscosity 7.5mPa.s at 20°C, 98%, Alfa-Aesar) was the solvent used for the preparation of nanocrystalline powders (nanopowders). These reagents were used as received and without further purification. Unlike previous related reports, no additional chelating agent was used in our case.

##### ***ii. Experimental procedure***

First, Gd(III) and Eu(III) acetates were dissolved separately in 2-ethylhexanoic at 200°C. Suitable weights of each precursor salt was used in order to attain desired atomic fraction of Eu dopant, (x= 0.0-0.30), in the Gd<sub>2-x</sub>Eu<sub>x</sub>O<sub>3</sub> powders. The solutions of Eu and Gd species were mixed and stirred for 10 min to obtain the atomic blending required to form the doped oxides. The total volume of this solution was 25ml with a total concentration of RE ions of 0.15M. The Eu-Gd solution was heated for 72 hours at 200°C till most of the solvent get evaporated. The solid intermediate was thermally treated by annealing for 2 hours at different temperatures (750°C, 850°C and 950°C), which were selected based on previous TG-DTA analysis of the precursor salts and intermediates. Final products were grounded in an Agate mortar and submitted for characterization. Figure 4.3 shows the flow diagram of the experimental process.

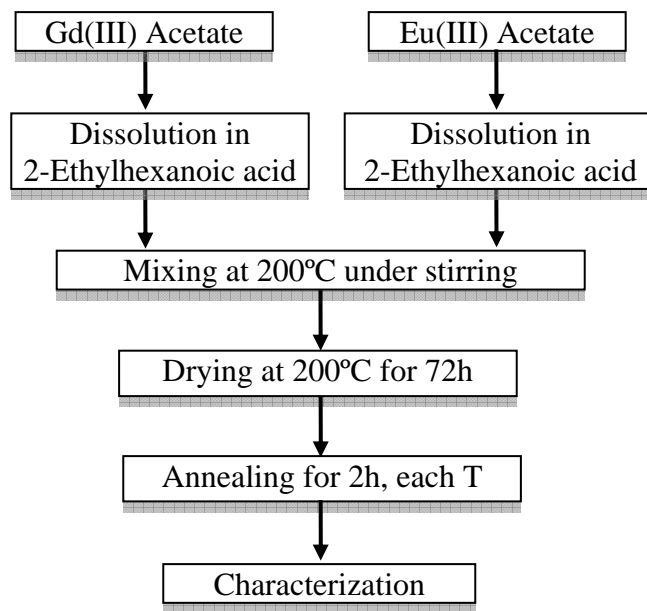


Figure 4.3 Experimental procedure for the synthesis of  $Gd_{2-x}Eu_xO_3$  nanocrystalline powders.

#### 4.2.2 Growth of nanocrystalline Eu-doped $Gd_2O_3$ Thin Films

##### *i. Materials*

Hydrated acetates of Gd(III) and Eu(III) (99.9%, Alfa Aesar) were used as precursor salts, and Glacial acetic acid was selected as solvent for the preparation of thin films. These reagents were used as received and without further purification. Unlike previous related reports, no additional chelating agent was used in our case.

##### *ii. Experimental procedure*

Europium-doped  $Gd_2O_3$  thin films were grown using the sol-gel method and spin coating onto fused quartz. Gd(III) and Eu(III) acetates were dissolved separately in acetic acid at  $120^\circ C$ , under vigorous stirring. Suitable weights of each precursor salt was used in order to attain desired atomic fraction of Eu dopant, ( $x= 0.0-0.30$ ), in the  $Gd_{2-x}Eu_xO_3$  thin films.

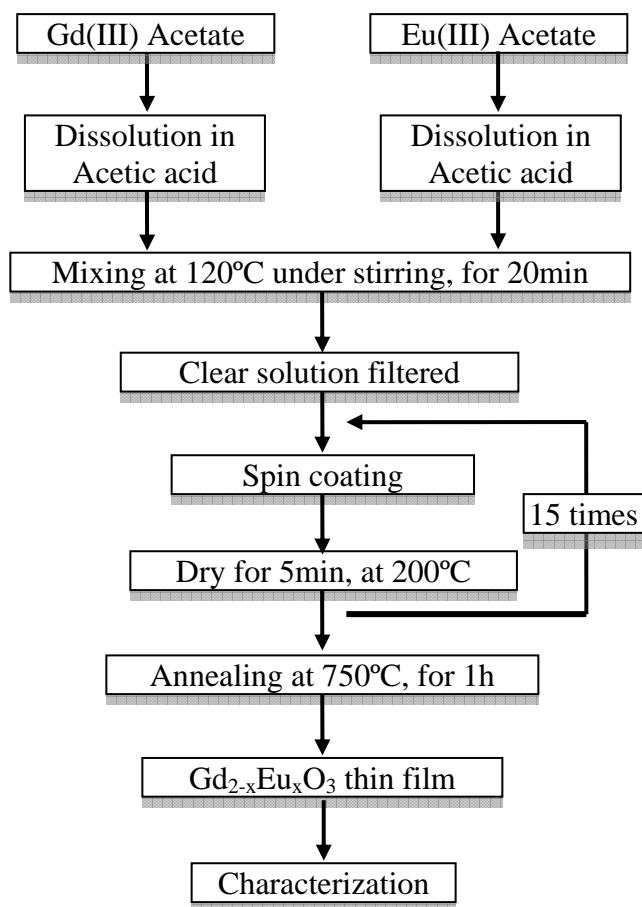


Figure 4.4 Flow diagram of the sol-gel spin coating of  $Gd_{2-x}Eu_xO_3$  thin films.

The solutions of Eu and Gd species were mixed and stirred for 20 min till a clear and homogeneous solution was obtained, which served as the coating solution. The total volume of this solution was 15ml with a total concentration of RE ions of 0.05M. Solutions were filtered through a  $0.2\mu m$  syringe filter before placing it onto fused quartz (1cm x 1cm x 1mm) substrate by spin coating. After setting the substrate on the disk of the spin coater, the coating solution was added dropwise while spin coating at 6000 rpm for 20s in air. The precursor film was placed onto a hot plate (in air) for 5 minutes at  $200^\circ C$  to remove residues of solvent. The dried film was then placed back onto the spin coater to repeat the previous coating process. This coating/drying cycle was repeated 15

times to assure a suitable thickness of the deposit. Produced films were heated (annealed) in air at 750°C for 1 hour in a muffle furnace, cooled down inside the furnace and finally submitted for characterization. Figure 4.4 summarizes the steps followed in the preparation of the thin films.

### **4.3 Characterization of the nanostructures**

In this work, different characterization methods were used to evaluate the structural, optical, luminescent and magnetic properties of different nanostructures produced, as well as the precursors and intermediates properties. In order to estimate the range of temperatures to develop the oxide structure, the thermal decomposition of different acetate salts precursors and intermediates was investigated by Thermogravimetric and differential thermal analysis (TG-DTA) using a TGA-Mettler Toledo. A suitable amount of the precursor powders was loaded into a standard aluminum oxide crucible (70 $\mu$ l), which was heated from room temperature to 950°C at 10°C/min in flowing N<sub>2</sub> atmosphere. Solid intermediates and annealed products were structurally characterized by X-Ray Diffraction (XRD) using the Cu-K $\alpha$  radiation in the 2 $\theta$  range between 15° and 80°. Other measurement conditions were 0.02° scanning step and 1sec of sampling time. The average crystallite size was estimated from the XRD patterns using the FWHM approach (Scherrer's formula [73]). These structural analysis were complemented by Fourier Transform Infrared (FTIR) spectroscopy of intermediates and final products using a MIRacle™ ATR FTS 1000 spectrometer in the transmittance mode. SEM- EDAX was used for elemental composition analysis of annealed powders. The nanostructures were

investigated by Raman spectroscopy with a Renishaw micro-Raman system. The spectra were taken at room temperature using a 514.5nm (2.41eV) excitation line from an Ar<sup>+</sup>-ion laser. Luminescence properties of the produced oxides were determined by Photoluminescence (PL) spectroscopy, using a Spectrofluorometer FluoroMax-2 with a 150mW continuous ozone-free Xe lamp as the excitation source. The measurements were carried out at room temperature, placing a suitable amount of powder on aluminum holder, designed for solid samples, and covered with a quartz slice. The thin films were placed directly on the movable base. To evaluate the magnetic response of Eu<sup>3+</sup>-doped Gd<sub>2</sub>O<sub>3</sub> nanopowders, the M-H loops of selected samples were measured in a Superconducting Quantum Interferometer Device (SQUID) Quantum Design MPMS XL-7 magnetometer, under room temperature conditions. Following, the main characterization techniques used are briefly reviewed.

#### **4.3.1 X-Ray Diffraction (XRD)**

X-ray diffraction is a nondestructive technique, and is one of the widely used for determining lattice parameters, preferred orientation of the crystal, phase composition (qualitatively and quantitatively), grain sizes, lattice strain, residual stress etc. XRD can provide the information from a relative larger area of the specimen compared to TEM. When a monochromatic x-ray beam incident onto a crystal sample, the constructive diffractions (or interference) from parallel planes of atoms with inter-planar spacing  $d$  occur if Bragg's law is satisfied (figure 4.5) [71]:

$$2d \sin\theta = n\lambda \quad (4.1)$$

where  $n$  is integer that indicates the order of the reflection,  $\theta$  is Bragg angle, and  $\lambda$  is the wave length of the x-ray beam.

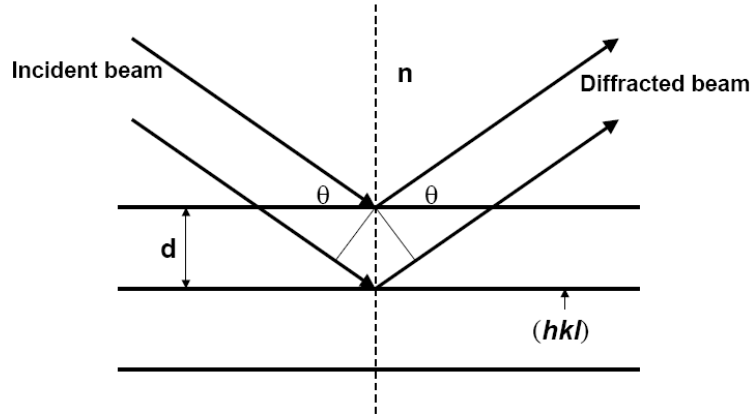


Figure 4.5 Schematic diagram of Bragg's diffraction from a set of parallel planes.

By measuring the Bragg angle  $\theta$ , the interplanar distance  $d$  can be obtained if the wavelength of the x-ray beam is known. In our case, the Cu-K $\alpha$  radiation ( $\lambda=1.54056\text{\AA}$ ) was used, and the crystalline phases and orientation were identified by matching the XRD peaks with those given in the data base of the program MATCH [72]. Furthermore, the lattice parameters are related with Miller indexes  $(hkl)$  of each reflection plane and interplanar distance ( $d_{hkl}$ ). For example for hexagonal and cubic structures, we have, respectively:

$$\frac{1}{d_{hkl}^2} = \frac{4}{3} \left( \frac{h^2 + hk + k^2}{a^2} \right) + \frac{l^2}{c^2} \quad (4.2)$$

and

$$a = d_{hkl} \sqrt{h^2 + k^2 + l^2} \quad (4.3)$$

On the other hand, the first treatment of particle size broadening was done by Scherrer. By making some simplifications, e.g., taking a powder sample of a small cubic crystal, and assuming they are free from strains and faulting, so that the peak broadening is due only to the small size, the following Scherrer's equation [71]

$$D = \frac{K\lambda}{B \cos\theta} \quad (4.4)$$

where  $D$  is the particle diameter,  $\theta$  is the diffraction angle, and  $B$  is the full width at the half high maximum (FWHM). The factor  $K$  involves different instrumental aspects, such as geometry, penetration of X-Ray in the sample, etc. From the width of the diffraction peak using the Scherrer's equation, one can calculate the average particle size. In our case, the value  $K=0.9$  was used. However, the width of diffraction peaks is broadening due to presence of defects or strain in the crystal lattice. The extreme case corresponds to amorphous materials, for which the peaks disappear totally.

In nanostructured materials, the Scherrer's equation provides an estimated value of the crystal size. However, in these materials, an appreciable fraction of atoms are on surface, and the ordering of these atoms is slightly different that those inside, which leads to broadening of peaks.

### **4.3.2 Absorption spectroscopy**

One the widely used method of optical characterization is the absorption (from infrared to ultraviolet range). When an incident light beam interacts with a medium, part of the beam

will be reflected on the medium surface, part of the beam will be transmitted through the medium, and the rest of the beam will be absorbed. Absorption of photons arises due to the transition of the electrons from lower energy levels to the higher energy levels. The absorption ability of a matter is measured by its absorption coefficient. Absorption coefficient,  $\alpha$ , for a uniform medium can be defined in terms of the intensity change of a monochromatic light beam in unit distance that the beam traveled in the medium:

$$\frac{dI(\lambda)}{dx} = -\alpha(\lambda)I(\lambda) \quad (4.5)$$

Therefore, the beam intensity as a function of the distance  $x$  can be written as:

$$I(\lambda) = I_0(\lambda)e^{-\alpha(\lambda)x} \quad (4.6)$$

On the other hand, absorption coefficient is a function of frequency (or wavelength). The variation of absorption coefficient with wavelength is called the absorption spectrum of the medium.

An absorption spectrometer (or transmission spectrometer) is generally composed of one (or two) monochromator, a continuous light source, and a photomultiplier. The spectrometer is equipped with two continuous light sources - a W lamp for measuring in the visible range (from 1000 nm to 320 nm) and a deuterium lamp for the measurement in ultraviolet range (from 320 nm to 200 nm; in our case, this technique was used to evaluate the optical properties of ZnO-based nanocrystals and Gd<sub>2</sub>O<sub>3</sub>-based thin films, in the wavelength range between 200nm and 800nm). In brief, light beam is first split into a

monochromatic one by the pre-monochromator, and then is incident onto the sample. A main monochromator is also installed in order to increase the measurement resolution. After the transmitted beam passes through the main monochromator, its intensity is measured by the photomultiplier and recorded by the computer. It should be noticed that reflectivity is not always negligible and the contribution from reflection is also added into the final data. The data obtained from absorption spectrometer is not the absorption coefficient, but its product with the sample thickness  $d$ . To obtain the value of absorption coefficient,  $d$  must be known. Therefore, the optical band gap ( $E_g$ ) is calculated using the value of  $\alpha$  in the following equation for semiconductors:

$$\alpha \equiv \frac{A(h\nu - E_g)^n}{h\nu} \quad (4.7)$$

where  $A$  is a constant which depends on the effective mass of the holes and electrons, and the refractive index of the material, but independent of the frequency;  $h$  is Planck constant,  $\nu$  is the frequency of the incident photon, and  $n$  depend of the type of transition, being  $\frac{1}{2}$  for direct transitions.

### **4.3.3 Photoluminescence (PL) Spectroscopy**

#### ***4.3.3.1 Fundamentals***

In photoluminescence spectroscopy, the sample is excited with a light with energy higher than the bandgap energy, and the emitted radiation is measured as a function of energy. The excitation creates electron-hole pairs which thermalize rapidly. The emitted light is

produced by the radiative recombination of these pairs. The most important radiative recombination centers are donors and acceptors, where the electrons and holes can be localized by themselves or after forming a common bound state called an exciton. Hence in a photoluminescence spectrum four different types of optical transitions are observed: band-to-band (no localization), free-to-bound (either hole or electron is localized), donor-acceptor-pair (both the hole and the electron are localized) and exciton recombination (either free or bound). In conclusion, PL spectrum provides us the information about the structure of energy levels in the sample.

The excitation spectrum is actually an absorption spectrum, which is obtained by monitoring the luminescence at a specific wavelength, i.e. at the peak of emission of our interest. Therefore, the excitation spectrum is used to locate the energy levels of the excited states. In our case, figure 4.6 shows a general structure of Spectrofluorometer used for photoluminescence measurements. In the monochromator, white light from a xenon lamp is collected by an elliptical mirror and directed to the entrance slit. Then the light is dispersed through the grating and then is directed to the exit slit of the monochromator (for excitation). A specific wavelength is selected by the monochromator from the incoming light. The entrance and exit ports (or slits) of the spectrometer and the monochromator are adjustable in increments of  $25\mu\text{m}$ . These are computer-controlled slits. To be able to detect the lamp profile of the output beam, a photodiode is used. The slits of the monochromator determine the amount of monochromatic light that is used to illuminate the sample. The spectrometer slits, on the other hand, control the intensity and

resolution of the fluorescence signal that is detected by the photomultiplier (PMT). The PMT signals are amplified and processed.

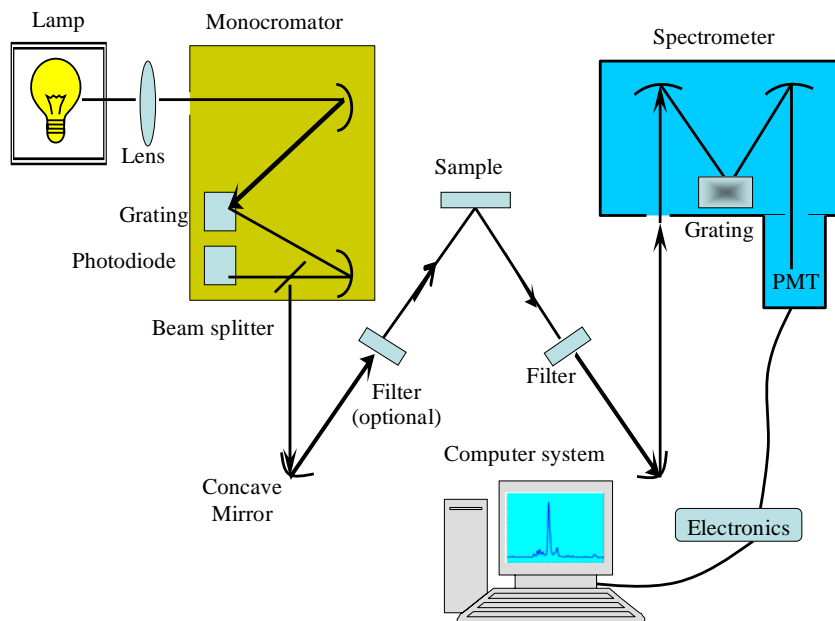


Figure 4.6 Simplify Structure of the Spectrofluorometer Fluoromax 2.

#### 4.3.3.2 Optimization of measurements

Due to the sensitivity of photoluminescence spectroscopy measurements, several aspects required special attention in order to improve the precision in the SPEX FluoroMax 2. The following aspects were considered in our case.

- a) **Lamp interference.** The spectrofluorometer used in this work uses a 150mW continuous ozone-free Xe lamp with a spectral range of 200-800nm, as the excitation source. The original emission spectrum obtained under standard conditions is shown in figure 4.7. The broad band centered on 450nm was overlapped with other sharp peaks (the most intense was centered on 466nm). These sharp peaks correspond to the

lamp profile and, evidently, will mask any signal coming from the materials. Therefore, the use of any filtration method (for example using an UV band pass filter), should be advised. Unfortunately, it was not possible use the UV band pass filter in our system. However, due to intensity of  $\text{Eu}^{3+}$  ions, no effect on spectra is expected.

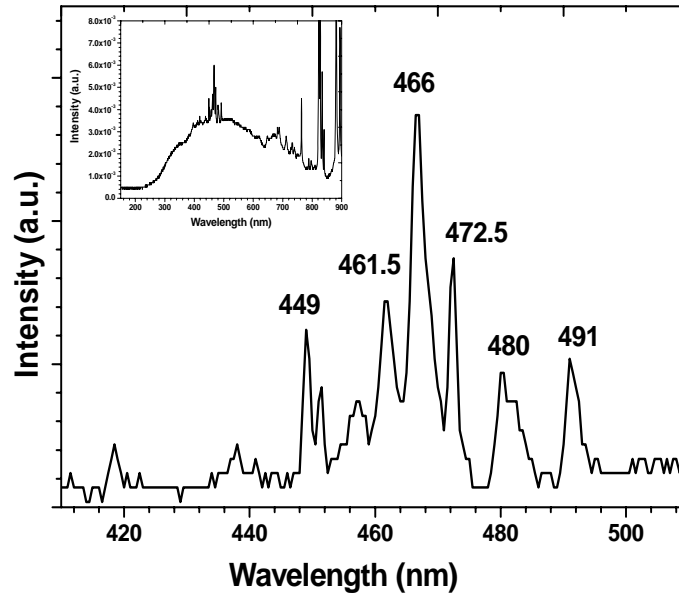


Figure 4.7 Detailed Emission spectrum of the 150mW continuous ozone-free Xe lamp, of the Spectrofluorometer FluoroMax-2, used for photoluminescence measurements. The whole spectrum is shown inset.

b) **Slit width and operation mode.** Preliminary PL measurements (excitation and emission) were carried out to determine the optimum measurement conditions. Considering that the maximum intensity of the bands of both spectrum excitation and emission do not saturate the detector, different slit widths were used in our measurements. The spectra of  $\text{Eu}^{3+}$ -containing ZnO nanocrystalline powders and nanocrystals were collected using a slit width of 4mm, where 4nm stands the aperture of out slit, whereas a slit width of 2mm was selected for the measurements in the  $\text{Eu-Gd}_2\text{O}_3$  system.

The selection of the operation mode will affect the quality of the PL measurements (figure 4.8). The observed variations by selecting the different combination of slit and S/RC or Sc modes reflect the interference by the lamp signal. Therefore, on the previous considerations, we solved this problem by selection the S/Rc and Rc modes, for excitation and emission spectra respectively.

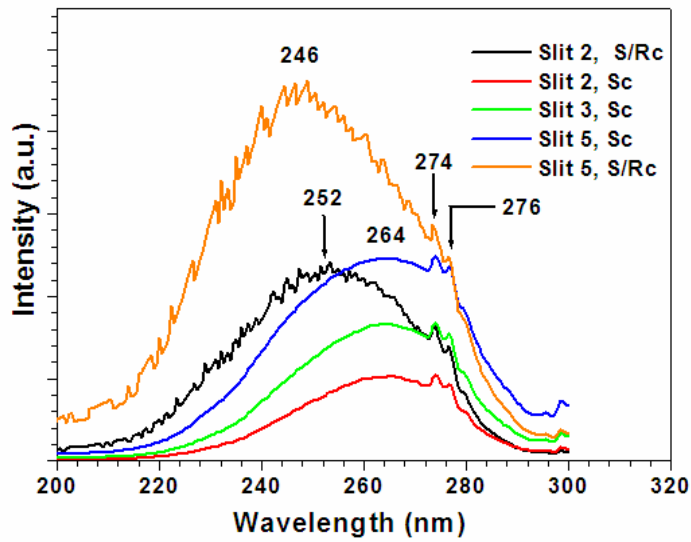


Figure 4.8 Effect of Slit and collect mode of the spectrometer on the excitation spectra at low wavelength region. A sample of Eu<sup>3+</sup>-doped Gd<sub>2</sub>O<sub>3</sub> (x=0.05) was used, but similar effects were observed for other cases.

# CHAPTER V: RESULTS AND DISCUSSION

## 5.1 Eu<sup>3+</sup>-containing ZnO

### 5.1.1 Nanopowders

#### 5.1.1.1 Thermal analysis of precursor salts

Figure 5.1 shows the TGA-DTA profiles of Eu(III) and Zn(II) precursor acetate salts. Three decomposition stages are clearly distinguished in the TG profile for Eu precursor while only two stages are observed to Zn precursor. The first stage for both salts, at low temperature is attributed to the evaporation of adsorbed moisture and crystallization water from the acetate salts. The second step ends at around 400°C for Europium and at around 340°C for Zn(II) acetate. There is a last step that is completed at 650°C for the Eu(III) precursor suggesting the end of the thermal decomposition processes and complete crystallization of the oxide phase.

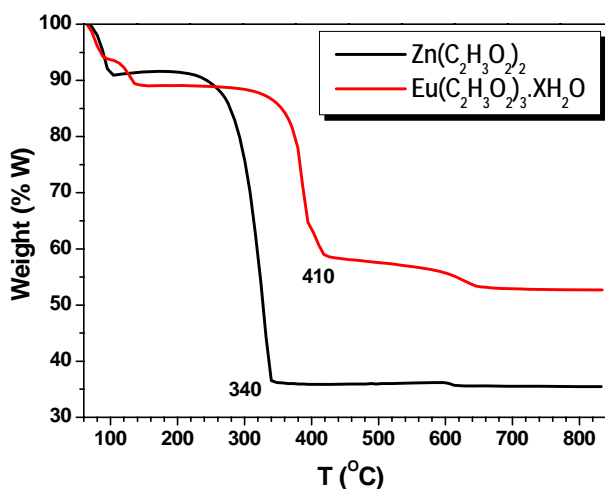


Figure 5.1 TGA profiles for Zn(II) and Eu(III) acetate salts. Different transformation temperatures are shown.

The total weight loss was around 50% for Eu(III) precursor acetate salt and 65% for the Zn(II) acetate. The remarkable differences in the TG behavior of both precursors salts suggest, the difficulty of achieving actual doping of ZnO with Eu species under the conditions used in this work.

#### ***5.1.1.2 Structural characterization***

Figure 5.2 shows the XRD patterns of ZnO powders synthesized by the sol-gel method at 200°C and with different atomic fractions of Eu ions, 'x'. Only the peaks corresponding to wurtzite ZnO (JCPDS card No 36-1451), were observed. The absence of other isolated phases may suggest the possible incorporation of  $\text{Eu}^{3+}$  within the host ZnO lattice. However, considering that the ionic radii of  $\text{Eu}^{3+}$  (0.95Å) is much larger than that for  $\text{Zn}^{2+}$  (0.74Å), the exchange between Eu and Zn species should have been reflected by a strong distortion of the ZnO unit cell and hence, of the corresponding lattice parameters. This distortion would be evidenced by marked shifts of the XRD peaks toward lower diffraction angles. It was not the case, since all XRD peaks appeared more or less on the same angular position (figure 5.2). Moreover, as shown in figure 5.3, a random behavior of the values of the lattice parameters with 'x' was observed. Therefore, although actual incorporation of Eu species into the ZnO lattice could not be claimed the possible presence of Eu species as poorly crystalline precipitates or as adsorbed species onto ZnO particles could be considered. Although the lattice parameter values exhibited a random variation with the nominal  $\text{Eu}^{3+}$  contents, 'x', no appreciable effect on "c" and "a" parameters was observed when compared to pure ZnO.

The average crystallite size, estimated by using the Scherrer's equation, varied between 7.7 and 11.6nm when the 'x' values were increased from 0, i.e. pure ZnO, up to 0.30 (Figure 5.4).

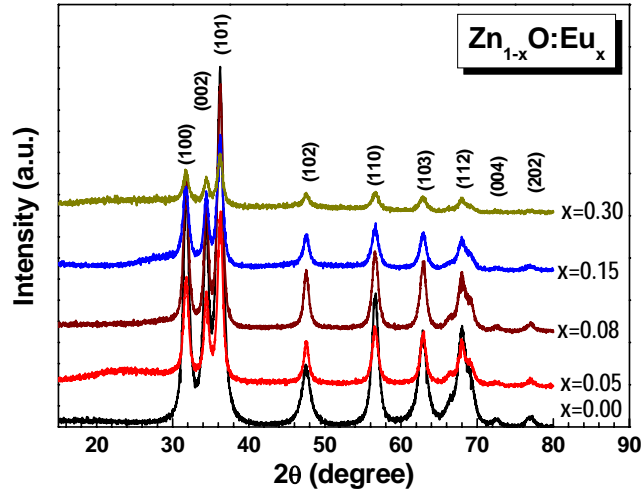


Figure 5.2 XRD patterns of nanopowders of ZnO, synthesized by sol-gel method, with different contents of Eu<sup>3+</sup> ions.

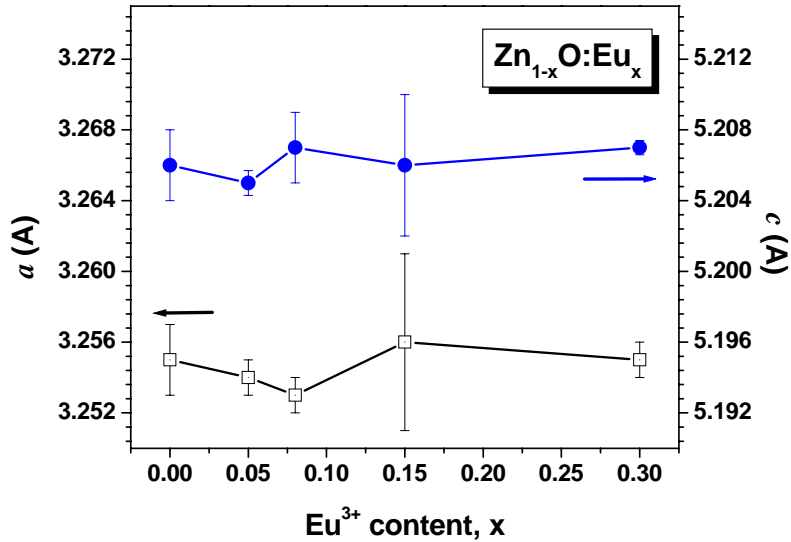


Figure 5.3 Variation of lattice parameters of ZnO nanopowders with Eu<sup>3+</sup> ions content, 'x'. The solid line is only for visual guide.

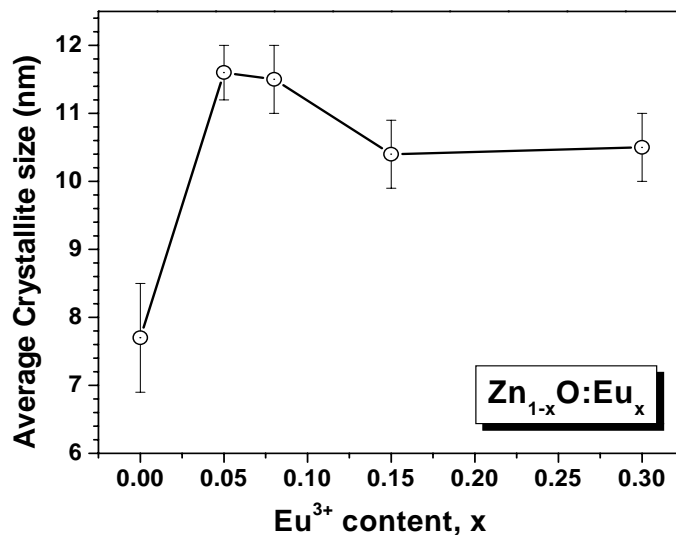


Figure 5.4 Variation of the average crystallite size of  $\text{Zn}_{1-x}\text{O}:\text{Eu}_x$  nanopowders as function of  $\text{Eu}^{3+}$  content. In general, the presence of  $\text{Eu}^{3+}$  ions leads to larger crystallite than pure ZnO. The solid line is only for visual guide.

As an attempt to clarify the presence of Eu species in the solid products, Zn(II) and Eu(III) acetates were dissolved separately. The corresponding solutions were then heated at 200°C for 72 hours. The dried solids were analyzed by XRD and the corresponding patterns are shown in figure 5.5. Evidently, the Zn(II) acetate was thermally converted into the anhydrous oxides, whereas the Eu(III) solid was still amorphous. This result suggests that the thermal decomposition of Zn acetate and Eu acetate precursor should take at different conditions and no probable formation of a solid solution should be expected under these conditions, as was previously discussed in section 5.1.1.1 about Thermal analysis of precursor salts (see figure 5.1).

Therefore, based on the above information, the actual incorporation of Eu species into the ZnO host lattice seems not to be a viable process. Apparently, the Eu species will remain as an isolated poorly crystalline phase coexisting with well crystallized ZnO.

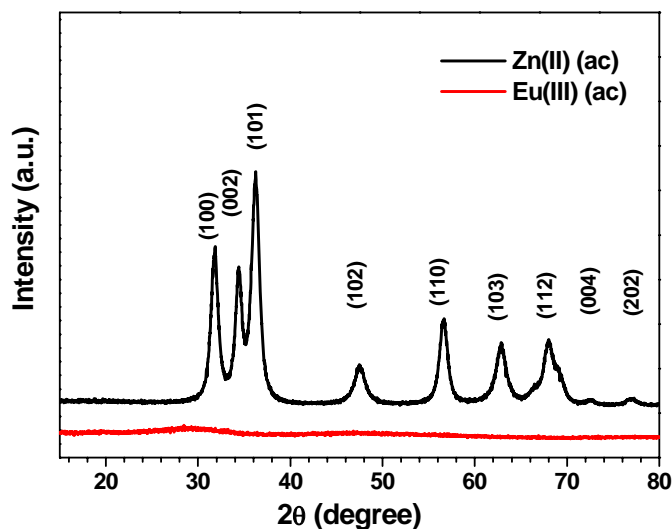


Figure 5.5 XRD patterns of Zn(II) and Eu(III) acetates, after dissolving and drying at the same conditions used for synthesis of nanopowders.

To get additional supportive data to our preliminary interpretation about the presence of Eu species in the ZnO solids, selected samples were annealed at different temperatures (350°C-550°C) in air for 1 hour. Figure 5.6 shows the corresponding XRD patterns for the solids obtained after annealing. As seen, the formation of crystalline  $\text{Eu}_2\text{O}_3$  became evident after annealing of the samples at temperatures above 500°C. No remarkable variation on lattice parameters of host ZnO was observed. Accordingly, poorly crystalline solid bearing Eu ions would be thermally decomposed into the corresponding oxide particles and then grow at temperatures higher than those required to form ZnO. The sharpening of the XRD peaks for the Zn and Eu oxides is a consequence of crystal growth, due to intergrain diffusion, a process that is promoted by higher temperatures. Therefore, the annealed solid would be considered more likely as a composite, with ZnO as matrix and Eu oxide as the disperse phase, than as a real doped ZnO structure.

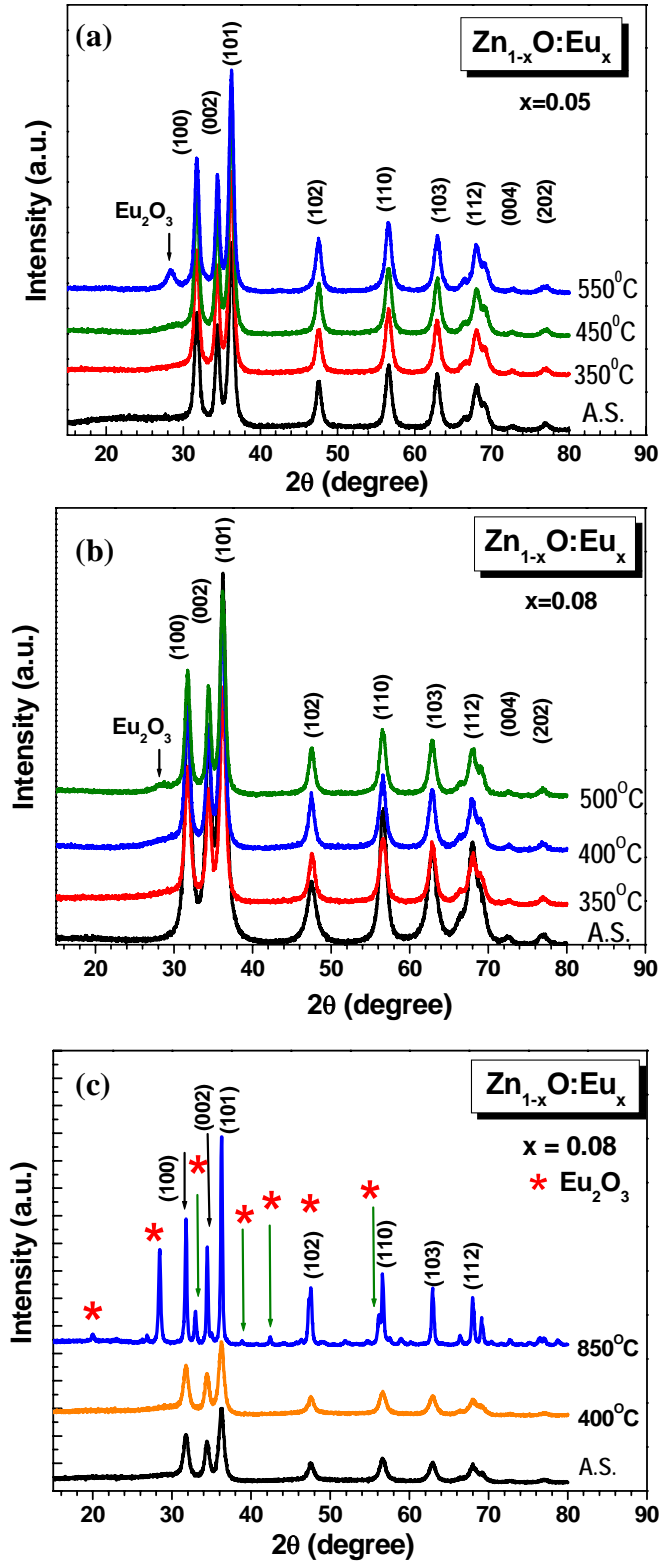


Figure 5.6 XRD patterns of nanopowders of ZnO containing  $\text{Eu}^{3+}$  ions and annealed at different temperatures.

### 5.1.1.3 Infrared analysis

In order to complement the structural information proved by XRD, as synthesized powders were analyzed by FT-IR spectroscopy. Figures 5.7 and 5.8 show the spectra for the solids synthesized at different 'x' values and annealing temperatures. The sharp band at  $524\text{cm}^{-1}$  is assigned to Zn-O bond, which is in good agreement with XRD analysis. However, broad and strong bands around  $1419\text{cm}^{-1}$  and a  $1550\text{cm}^{-1}$  were clearly observed in the spectra for all samples. These bands are assigned to asymmetric and symmetric C=O stretching vibration modes, respectively, in acetate species. As figure 5.7 shows, the bands of the acetate group were detected for all 'x' values, even after intensive washing of the samples in ethanol, suggesting that these group remaining as adsorbed species and/or as Eu-bearing intermediate that was not converted into the oxide phase. On the contrary, those bands almost disappeared after annealing of the samples (figure 5.8). These two facts support our previous interpretation of the early formation of ZnO followed by crystallization of Eu-oxide at higher temperatures.

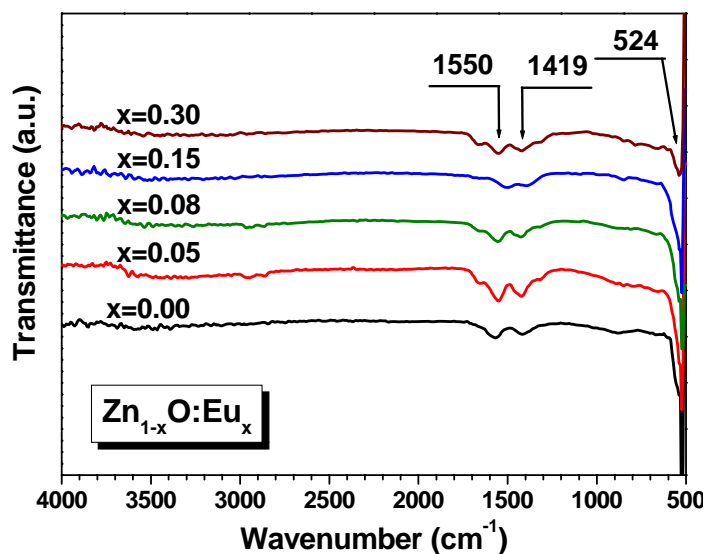


Figure 5.7 FT-IR spectra of ZnO pure and containing Eu<sup>3+</sup> ions.

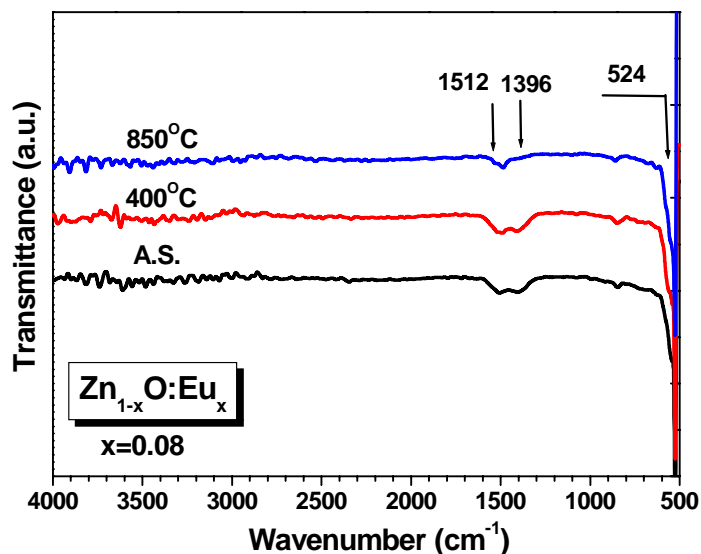


Figure 5.8 FT-IR spectra of ZnO containing  $\text{Eu}^{3+}$  ions ( $x=0.08$ ) annealed at different temperatures.

#### 5.1.1.4 Raman measurements

The wurtzite structure of ZnO belongs to the space group  $C_{6v}^4$  ( $C6_3mc$ ) with two formula units per primitive cell, where all atoms occupy the  $C_{3v}$  sites. Therefore, the group theory predicts the following lattice phonons:  $A_1+2E_2+E_1$ . The phonons of  $A_1$  and  $E_1$  symmetry are polar phonons and, hence, exhibit different frequencies for the transverse-optical (TO) and longitudinal-optical (LO) phonons. Non-polar phonon modes with symmetry  $E_2$  have two frequencies:  $E_2(\text{high})$ , which is associated with oxygen atoms and  $E_2(\text{low})$  that is related to the Zn sub-lattice. All phonon modes have been reported in the Raman-scattering spectra for bulk ZnO [73,74].

Figure 5.9 shows the Raman spectra, taken at room temperature, of as-synthesized ZnO powder (a), and after annealing at  $650^\circ\text{C}$  for 1 hour in air, (b). The spectrum

corresponding to (a) shows weak bands at  $438\text{cm}^{-1}$ ,  $332\text{cm}^{-1}$  and  $578\text{cm}^{-1}$  that are assigned to  $E_2$  (high), second order ZnO and  $A_1(\text{LO})$  modes, respectively. These bands became more intense after annealing of the samples; however, no shift was observed. This increase in the band intensity is associated to the enhanced crystallinity of the powders after annealing. The strong noise observed in the spectrum for the as-synthesized powder could be attributed to the low crystallinity in the sample, although the effect of acetates and solvent residual can not be ruled out at this time.

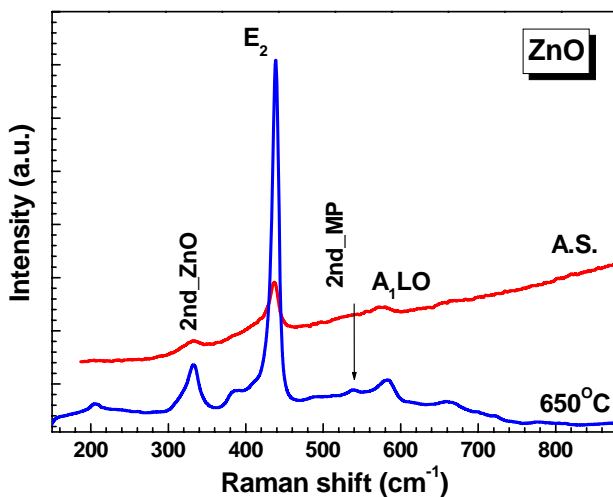


Figure 5.9 Raman spectra of ZnO nanopowders as synthesized (A.S.) and annealed at  $650^{\circ}\text{C}$  for 1 hour in air. The enhancement of crystallinity after annealing is evident, confirming the XRD results.

Similar spectra were obtained for the ZnO powders produced in presence of  $\text{Eu}^{3+}$  ions,  $x=0.05$ , (figure 5.10). For this sample, it seemed that expected enhancement in crystallinity at  $450^{\circ}\text{C}$  was not large enough to increase the intensity of the bands. In turn, the noise signal could be consequence of the luminescence of Eu species in the less crystalline fraction contained in the samples.

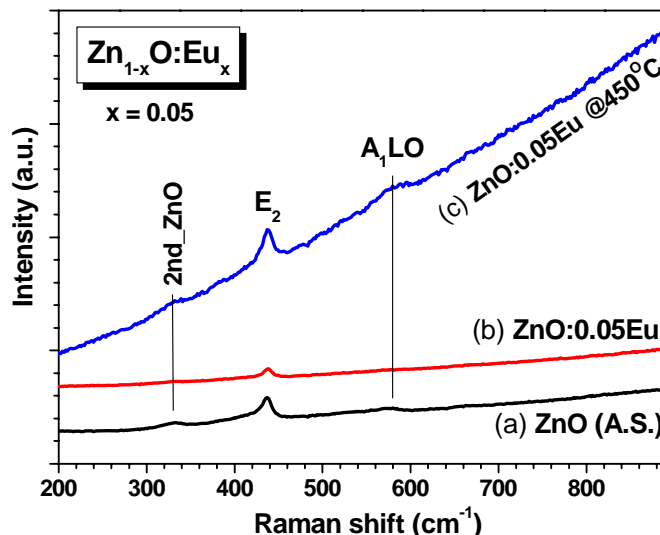


Figure 5.10 Raman spectra of ZnO nanopowders (a) without  $\text{Eu}^{3+}$  (as synthesized), (b) containing  $\text{Eu}^{3+}$  ( $x=0.05$ ) as synthesized and (c) the same of (b) but annealed at  $450^\circ\text{C}$  for 1 hour in air.

Also, according to TGA results (figure 5.1) a little amount of Eu-oxides would be present in the sample; therefore, bands related to these oxides should have been detected. The noisy signal should have masked those bands in the Raman spectra.

#### 5.1.1.5 Photoluminescence measurements

Figure 5.11 shows the room temperature photoluminescence spectra of bare and Eu-containing ZnO samples on excitation at 350nm. As observed, the spectrum of all samples only showed UV luminescence around 390nm, which based in previous studies on ZnO nanoparticles [45] has been attributed to the band edge emission. The visible emission typical of ZnO was considerably quenched; only the red emission band arising from  $\text{Eu}^{3+}$  ions was observed, whose intensity increases as the content of Europium increases. The bands assigned to the lamp effect were identified based on their characteristic emission spectrum (figure 4.1).

The absence of visible emission in our samples was also observed by Kanade et al. [75] and Wang et al. [77] for nanosize ZnO. They proposed that synthesized powders could be considered stoichiometric and defect-free. However, we propose that the band centered on 470nm must correspond to the lamp spectra rather than singly ionized oxygen vacancies, in contrast to Wang's interpretation [76].

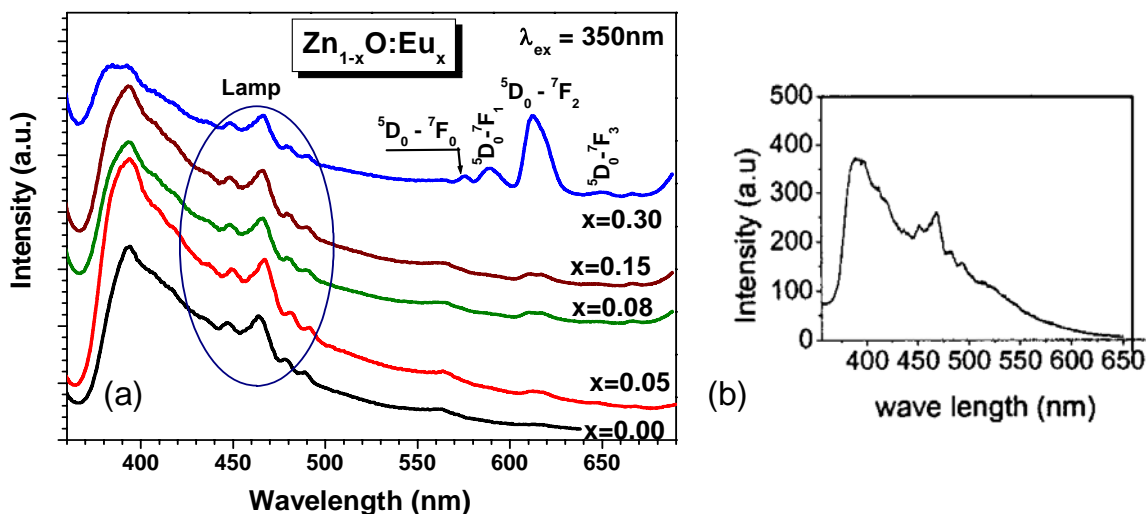


Figure 5.11 (a) Emission spectra, at room temperature, of bare and containing  $\text{Eu}^{3+}$  ions ZnO nanopowders synthesized in this work. No visible emission, related to ZnO defects, was observed. (b) Emission from ZnO nanowires on a silicon substrate reported in [76].

Based on the well-accepted fact that electronic and luminescence properties in a material can be strongly influenced by the synthesis conditions (type of solvent, heating temperature, for instance) [75,77], the probable influence of the residual amount of solvent on the PL behavior of Eu-containing samples was also considered in our experimental work. Therefore, the nanocrystalline ZnO powders were annealed at 650°C for 1h in air. This temperature is far above the boiling point of 2-ethylhexanoic acid

(227°C), and would be enough high to fully evaporate it. Figure 5.12 shows emission spectra of as-synthesized ZnO, washed in ethanol and annealed. As seen, although the increase in luminescence intensity after annealing of the sample was evident, no emission in the visible region was observed. The absence of this PL band in the visible region would suggest the possibility of producing high optical quality nanocrystalline ZnO with a low, or null, concentration of oxygen defects. This feature will be very important to enable the use of ZnO in optoelectronic devices.

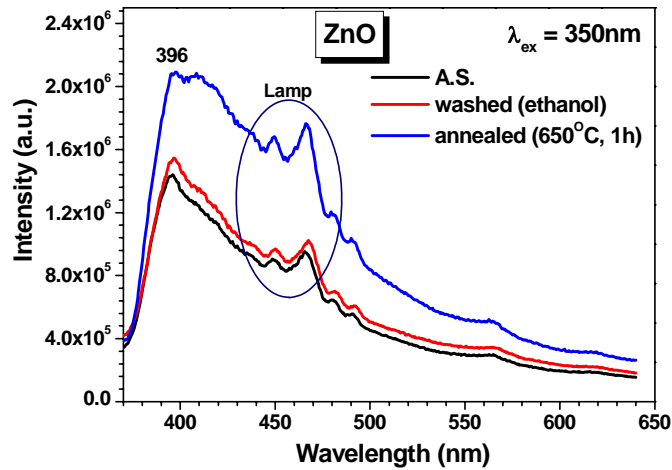


Figure 5.12 Effect of washing and annealing on emission spectra, at room temperature, of ZnO nanopowders. Similar to in synthesized (A.S.), no visible emission related to ZnO defects, was observed.

It is a well-established fact that the red emission from  $\text{Eu}^{3+}$  ions can be activated either by direct excitation, energy transfer or charge transfer from the host material. Figure 5.13 shows the PL spectra of ZnO samples containing  $\text{Eu}^{3+}$ , excited with lights of different wavelengths. The excitation by anyone of the mechanisms mentioned above implies the actual incorporation of the trivalent ion into the lattice of the host material. However, the claiming on the actual incorporation of  $\text{Eu}^{3+}$  into ZnO lattice from PL measurements is still under discussion and no clear conclusion can be stated.

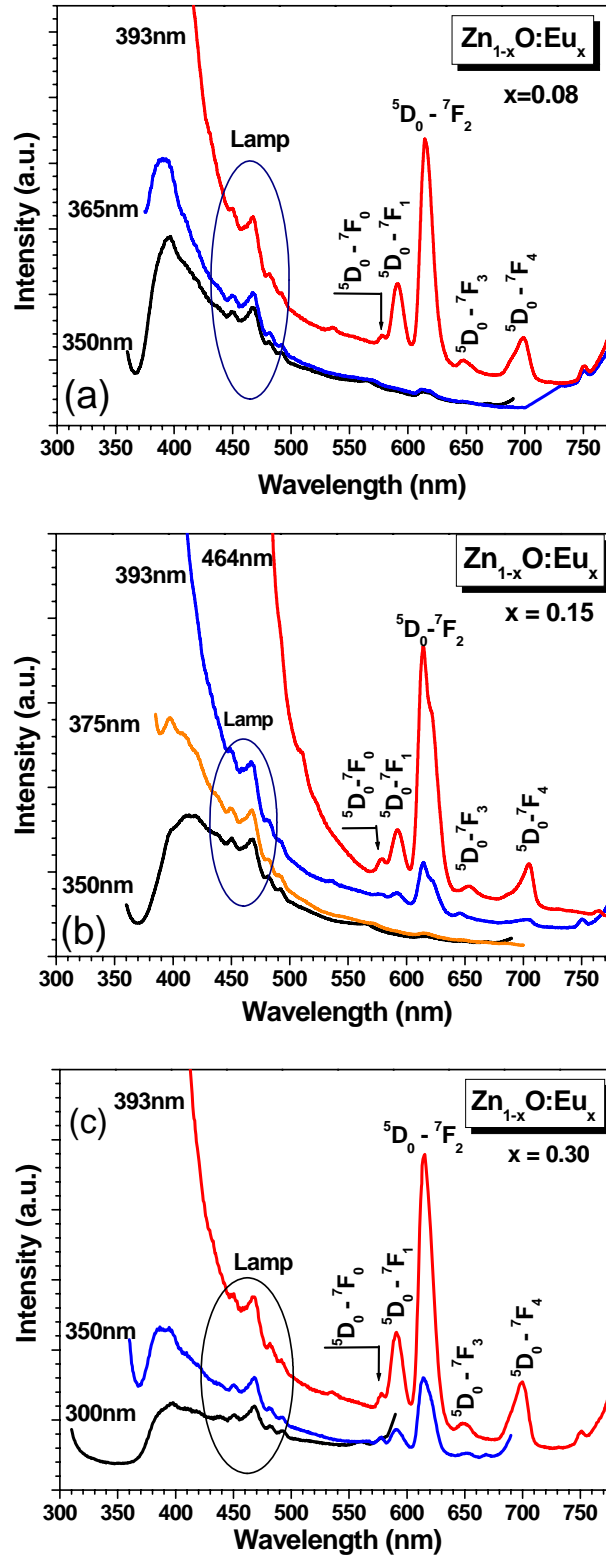


Figure 5.13 Emission spectra, at room temperature, of ZnO powders synthesized with different contents of  $\text{Eu}^{3+}$ .

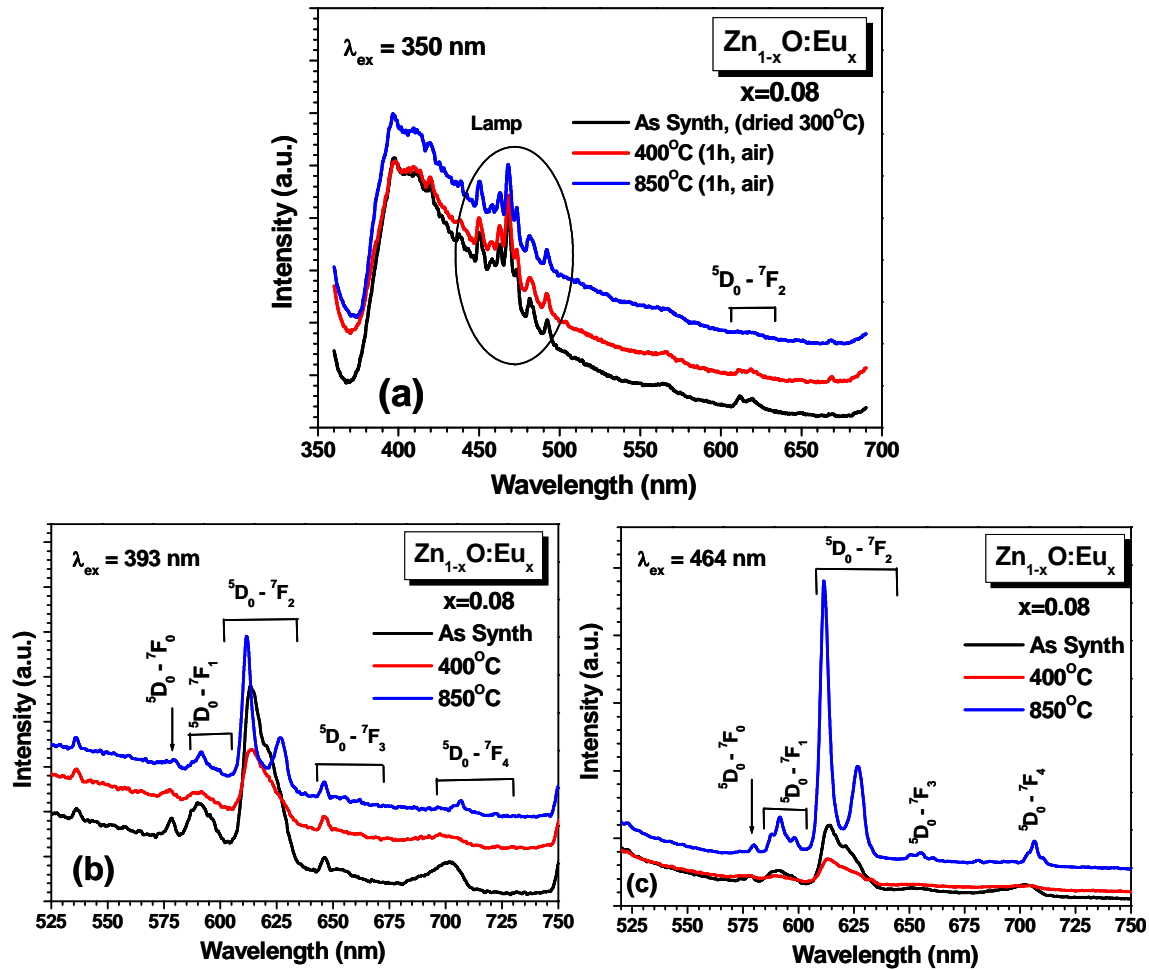


Figure 5.14 Emission spectra of ZnO nanopowders, containing 0.08%  $\text{Eu}^{3+}$  (w/w), as synthesized and annealed at different temperatures, and using different excitation wavelength: (a) 350nm, (b) 393nm and (c) 464nm.

The luminescence observed in ZnO produced in presence of Eu ions has been explained in terms of the presence of trivalent Eu species on the surface of ZnO [78]. Related works suggested that observed luminescence can be considered as the evidence for energy transfer from host ZnO to  $\text{Eu}^{3+}$ , and hence, actual doping. On this basis, the results from our PL measurements could indicate a possible energy transfer from ZnO host to  $\text{Eu}^{3+}$  ions, and therefore the actual incorporation of them in the wurtzite lattice; however, if this incorporation have really taken place, it should be only on a partial basis; i.e., only a

minor fraction of Eu species should be allocated in the ZnO lattice. This partial and minor incorporation of Eu species could also explain the observed results from the XRD analyses of our samples. Therefore, to get a better understanding of the actual role of Eu species on the observed photoluminescence in ZnO powders, 8%Eu<sup>3+</sup> (w/w)-ZnO samples were annealed in air at different temperatures and characterized by PL spectroscopy. The corresponding results are discussed as follows.

Figure 5.14 shows the PL spectra of ZnO with Eu<sup>3+</sup> (x=0.08), before and after annealing at different temperatures. This figure clearly shows that the intensity of luminescence associated to Eu<sup>3+</sup> ions at 614nm is continuously reduced, under 350nm excitation. This drop in the luminescence intensity took place despite of the observed enhancement in crystallinity, as suggested by XRD measurements. It would indicate that Eu ions are not excited. Therefore, in order to evaluate the luminescence behavior due to Eu species, the samples were excited using light of 393nm and 464nm, which correspond to the direct excitation of Eu ions from the ground state (<sup>7</sup>F<sub>0</sub>) to excited states <sup>5</sup>L<sub>0</sub> and <sup>5</sup>D<sub>0</sub> respectively, as shown figures 5.14(b) and 5.14(c). The analyses of these spectra revealed the splitting of the band corresponding to the radiative transition <sup>5</sup>D<sub>0</sub>-<sup>7</sup>F<sub>1</sub> of the Eu<sup>3+</sup> ions in the samples. This fact confirms that Eu species are in a crystalline field, which would be attributable to Eu<sub>2</sub>O<sub>3</sub> rather than ZnO (as shown figure 5.6 (c)); in other words, there was no actual incorporation of Eu species into the ZnO lattice.

From the above discussion, it can be concluded that although the thermal decomposition method allow us obtain ZnO nanoparticles with wurtzite structure, apparently without

Eu-based secondary phases, as shown results of XRD, FT-IR and Raman, the difference in the transformation temperatures of precursors (Zinc acetate and europium acetate), obtained by TGA, difficult the actual incorporation of the  $\text{Eu}^{3+}$  ions into ZnO structure, as shown from PL measurements. These measurements, carried out in annealed powders confirm conclusively that there is not energy transfer from the ZnO host to  $\text{Eu}^{3+}$  dopant. Also, from the results obtained with the annealed powders, it is possible that the ions would be adsorbed on surface of ZnO nanoparticles as amorphous phase. However, is important to note that the absence of visible emission, related to defects, would open the possibility to use this route to obtain ZnO nanoparticles for optoelectronic applications. However, in order to confirm it, complimentary measurements by other techniques, such as Electron Paramagnetic Resonance (EPR), Extended X-Ray Absorption Fine Structure (EXAFS), or X-Ray Absorption Near-Edge Structure (XANES) could be used in order to determine the lattice distortions around the trivalent Europium ion.

## **5.1.2 Nanocrystals**

### ***5.1.2.1 Structural characterization***

Figure shows 5.15 shows the XRD patterns of  $\text{Eu}^{3+}$ -containing ZnO nanocrystals. Except a weak peak near to (101) plane in the sample with  $x=0.30$ , which could be assigned to basic zinc acetate, in these patterns, no additional peaks of any impurities were detected. All peaks correspond to ZnO with a hexagonal wurtzite structure (JCPDS card No 36-1451). These patterns are similar to that reported by Y. Liu, et al., [7] who synthesized nanocrystals of  $\text{Eu}^{3+}:\text{ZnO}$  with a nominal concentration of 2at % following a similar

synthesis approach that in our case. Figure 5.16 summarizes the variation of lattice parameters with the  $\text{Eu}^{3+}$  contents, 'x'. Also in this case, a clear trend was no observed. On the other hand, the peak broadening is evidence of the nanocrystalline nature of the solids. The average crystallite size, which varied between 3.79nm and 3.54nm, was decreased by the presence of europium ions (figure 5.17). This behavior would indicate that the  $\text{Eu}^{3+}$  ions retarded the growth of ZnO nanocrystals probably by inhibiting the rate of the oxide formation from the re-dissolution crystallization of the hydrated intermediate.

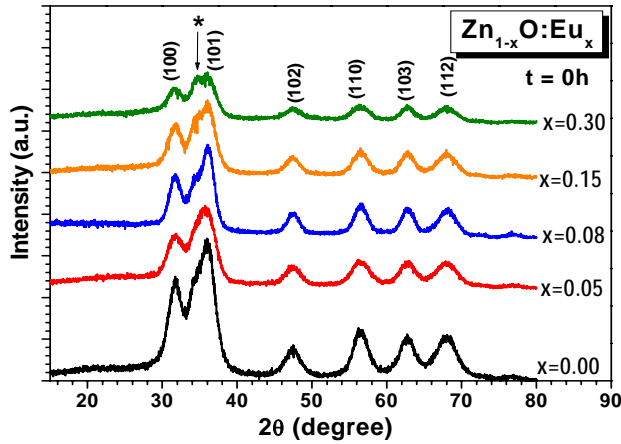


Figure 5.15 XRD patterns of  $\text{Zn}_{1-x}\text{O}:\text{Eu}_x$  nanocrystals, no aged, with different contents of  $\text{Eu}^{3+}$  ions.

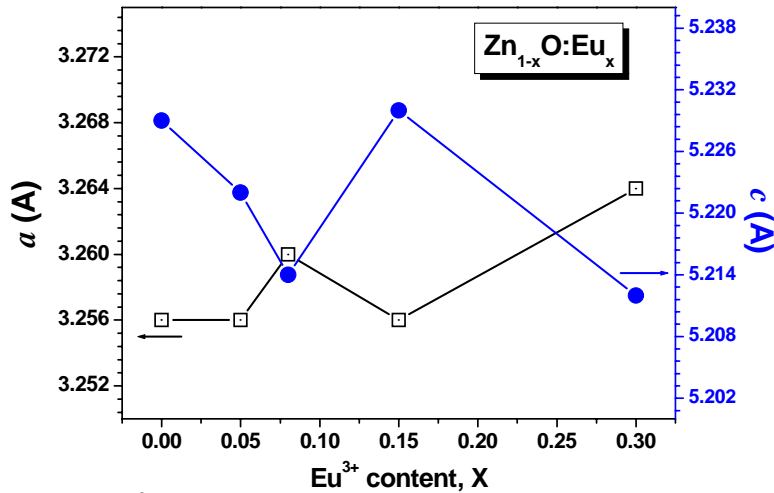


Figure 5.16 Effect of  $\text{Eu}^{3+}$  ions content on the lattice parameters of ZnO nanocrystals no aged.

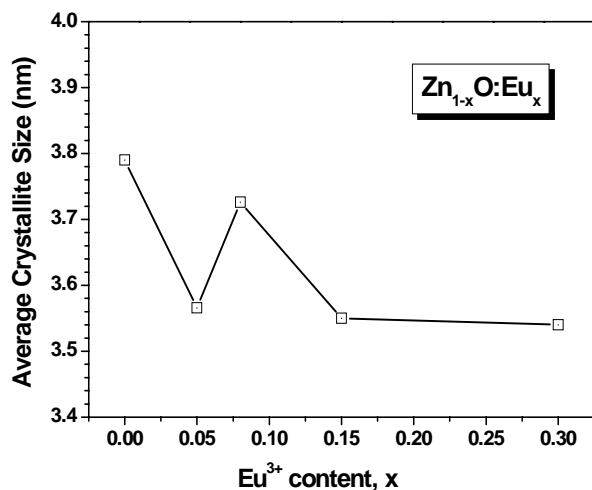


Figure 5.17 Effect of  $\text{Eu}^{3+}$  ions content on average crystallite size of ZnO nanocrystals no aged.

Figures 5.18 and 5.19 show the XRD patterns of bare and  $\text{Eu}^{3+}$  containing ( $x=0.30$ ), nanocrystals, respectively, aged for different times in their mother liquors at room temperature. The enhanced sharpness on the XRD peaks for pure ZnO samples with aging time confirms the promotion of crystal growth during aging. The corresponding average crystallite ranged from 3.79 to 8.45nm when the aging time was increased from 0h to 120 hours. This trend is in good agreement with what we observed in previous works [70]. However, in the samples containing  $\text{Eu}^{3+}$  ions ( $x=0.30$ ) a very sharp peak at  $2\theta=34.46^\circ$  was observed in the sample aged for 120 hours. This peak could correspond to some remaining amount of crystals of intermediate (basic zinc acetate) that were grown under prolonged aging times. The presence of this intermediate compound has also been detected in other related works [70]; somehow, the presence of Eu species could have stabilized the intermediate compound, or in other words, delayed the development of the ZnO phase.

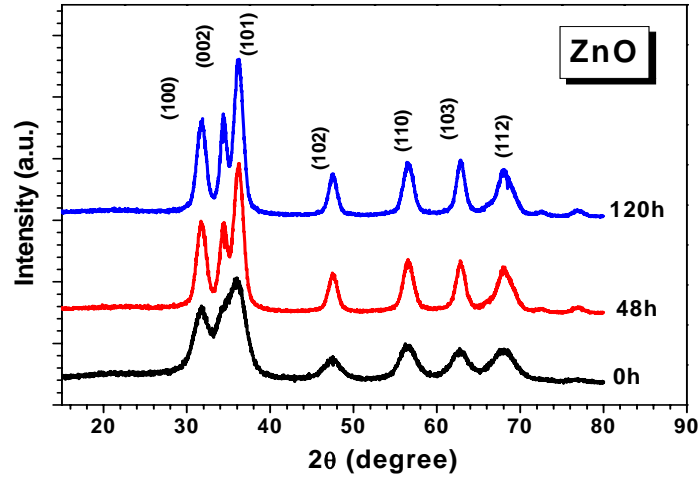


Figure 5.18 XRD patterns of ZnO nanocrystals aged for different times.

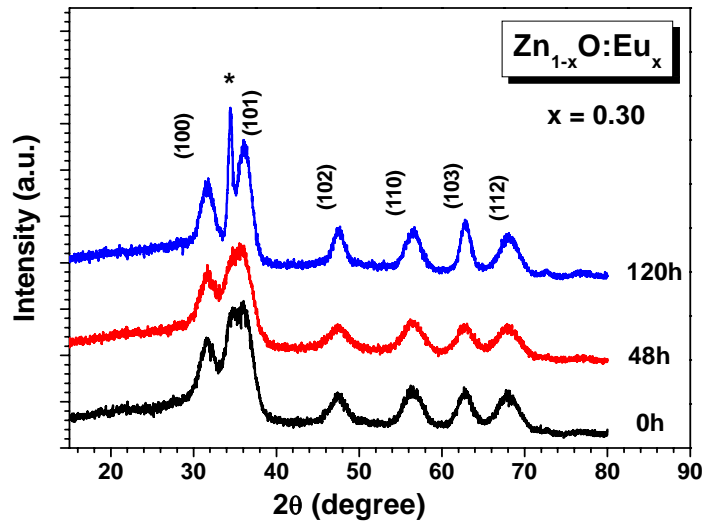


Figure 5.19 XRD patterns of  $\text{Eu}^{3+}$ -containing ZnO nanocrystals ( $x=0.30$ ) and aged for different times.

From the structural analysis it is clear that, the presence of  $\text{Eu}^{3+}$  would affect the growth of nanocrystals of ZnO. Therefore, further analysis in order to confirm these effects on the structural, optical and luminescent properties are necessary. However, due to the presence of intermediate compound detected in samples aged during 120h, which affect the luminescence properties of ZnO, all the following measurements are restricted to no aged samples.

### 5.1.2.2 Infrared analysis

Figure 5.20 shows the FT-IR spectra for non-aged pure and Eu-containing ZnO nanocrystals synthesized at various 'x' values. The intense centered on  $524\text{cm}^{-1}$  can be assigned to Zn-O bond, which corroborates the formation of the host ZnO. The broad bands around  $1411\text{cm}^{-1}$  and a  $1573\text{cm}^{-1}$  were assigned to asymmetric and symmetric C=O stretching vibration modes in acetate species, respectively. Aging did not affect the position and intensities of these bands (figure 5.21-a). Similar behavior was observed for samples containing  $x=0.30$   $\text{Eu}^{3+}$  (figure 5.21-b). These results would indicate that the acetate species could be adsorbed on surface of ZnO and on them the  $\text{Eu}^{3+}$  ions. However, further chemical studies are necessary in order to elucidate this fact.

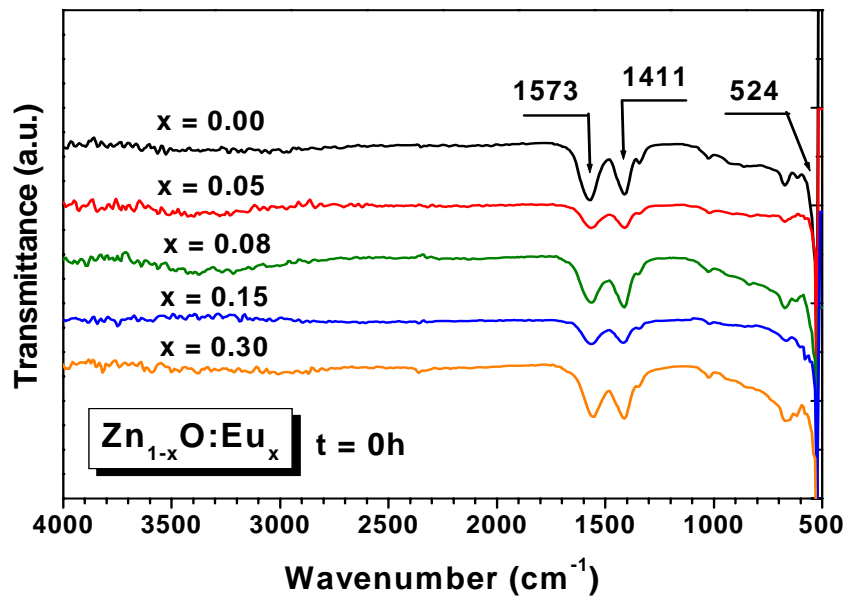


Figure 5.20 FT-IR spectra of  $\text{Eu}^{3+}$ -containing ZnO nanocrystals, which were not aged.

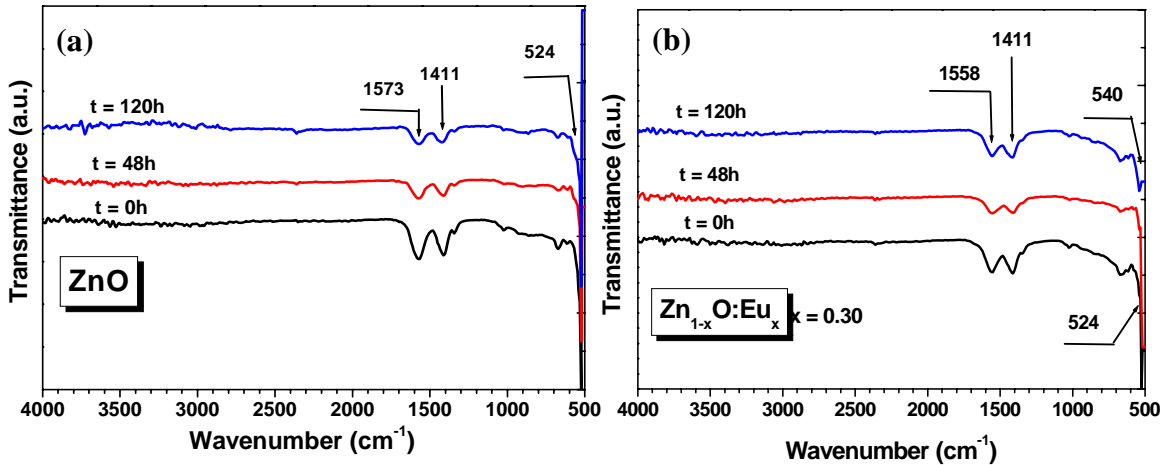


Figure 5.21 FT-IR spectra of (a) bare and (b) with Eu<sup>3+</sup> ions (x=0.30) ZnO nanocrystals aged for different times.

### 5.1.2.3 Raman measurements

Figure 5.22 shows the Raman spectra of bare and Eu<sup>3+</sup>-containing ZnO nanocrystals. The strongest band at 438cm<sup>-1</sup> has been assigned to non-polar modes with E<sub>2</sub>(high) symmetry and is associated with oxygen atom displacement. The intensity of this band increases as the Eu<sup>3+</sup> ions increases. The weak band at 330cm<sup>-1</sup> has been assigned to second order multiphonon process, which originates from the zone-boundary phonon of E<sub>2</sub>(low). The band at 581cm<sup>-1</sup> corresponds to E<sub>1</sub>(LO) mode, and is associated with oxygen deficiency [79]. The intensity of this band increases with the content of Eu<sup>3+</sup> ions, which would indicate that the presence of trivalent europium leads to generation of defects related to oxygen vacancies. In addition, the band assigned to multiphonon process shifts to lower energies by rising Eu<sup>3+</sup> ions contents. This effect could be consequence of a weak interaction between ZnO host and Eu<sup>3+</sup> ions.

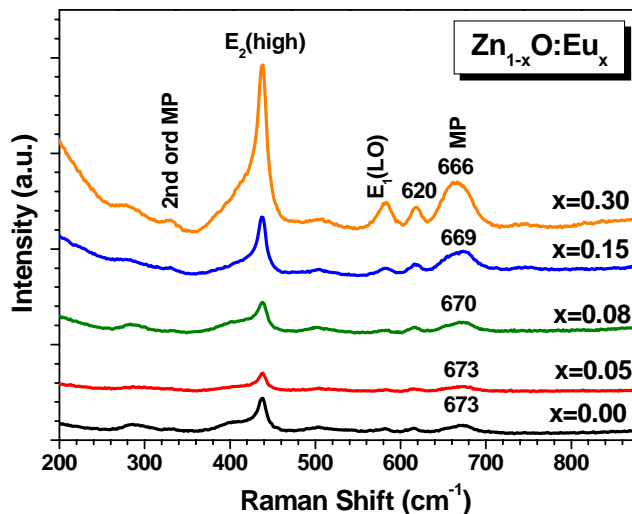


Figure 5.22 Raman spectra of bare and  $\text{Eu}^{3+}$ -containing ZnO nanocrystals no aged.

#### 5.1.2.4 Uv-Vis measurements

UV-Vis measurements were carried out in order to study the ZnO formation and crystal growth during aging. For this purpose, stable suspensions of  $\text{Zn}_{1-x}\text{O}:\text{Eu}_x$  nanocrystals in ethanol were withdrawn at different aging times and submitted for Uv-Vis measurements at room-temperature.

Figure 5.23 shows the absorbance spectra for non-aged bare and Eu-ZnO nanocrystals. A well-defined exciton peak was observed for all samples, which suggests a very fast nucleation. In addition to be blue shifted, the exciton peak became broad at rising values of the atomic fraction of Eu species, 'x'. This feature would evidence the increase in the crystals polydispersity.

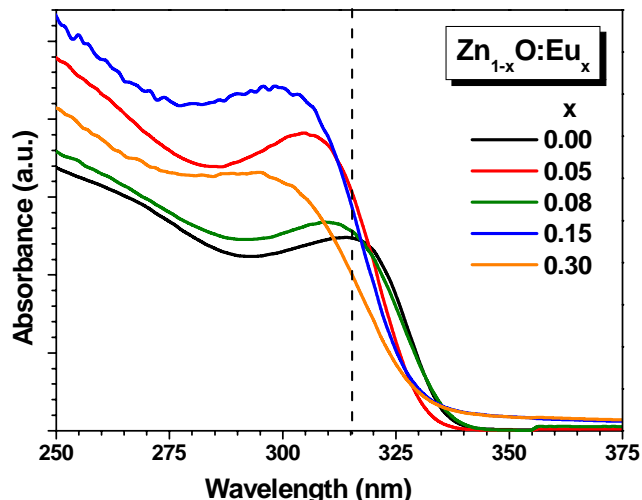


Figure 5.23 Absorption spectra of suspensions of bare and with  $\text{Eu}^{3+}$  ions ZnO nanocrystals no aged.

The band gap energy ( $E_g$ ) for each sample was estimated after linear fitting of the linear region of the UV-vis absorption curve, as shown in figure 5.24. Although the estimated band gap values did not exhibit a remarkable increase with rising ‘x’ values; however, the presence of Eu species in reacting solutions caused the absorption peak to be blue-shifted with respect to pure ZnO synthesized under similar conditions. This trend in the band gap energy could be related to the inhibition on crystal growth by the presence of Eu species in reacting solutions, a fact that was also proposed based on the results from XRD analysis. The relationship between band gap and  $\text{Eu}^{3+}$  ions content is summarized in figure 5.25-a. This figure also compares the obtained band gap values with those of bulk ZnO and  $\text{Eu}_2\text{O}_3$  (figure 5.25-b). In all cases, the nanocrystals (pure and Eu-containing ZnO) reported band gap energy values above the bulk value for ZnO (3.37 eV). This fact can be attributed to the strong quantum confinement effect, rather than any actual incorporation of europium.

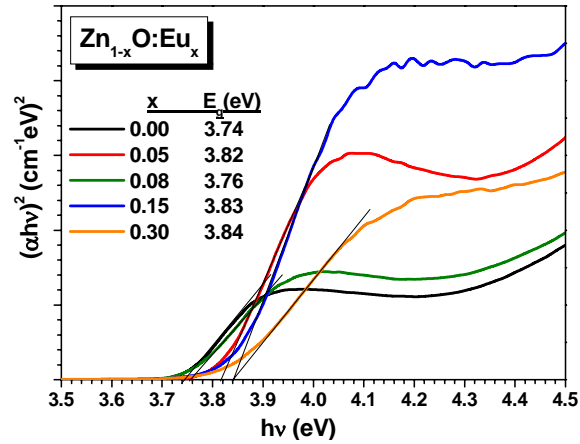


Figure 5.24 Absorption spectra of suspensions of bare and with  $\text{Eu}^{3+}$  ions ZnO nanocrystals no aged. The variation of band-gap is shown inset.

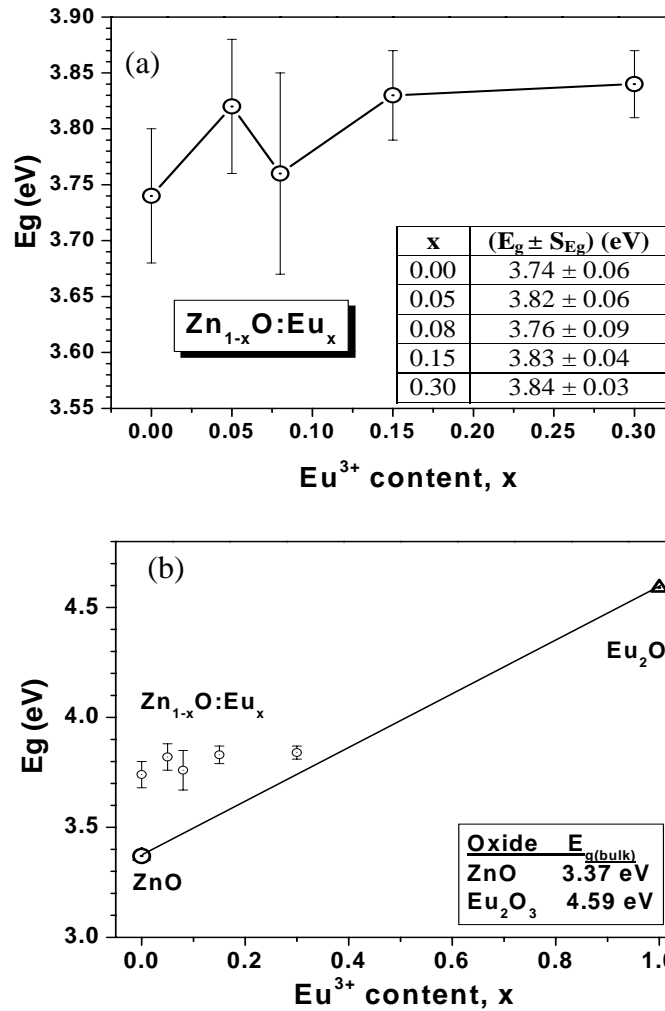


Figure 5.25 (a) Energy gap of  $\text{Zn}_{1-x}\text{O}:\text{Eu}_x$  nanocrystals no aged, as function on  $\text{Eu}^{3+}$  ions content, and (b) their position as respect to that of bulk ZnO and  $\text{Eu}_2\text{O}_3$ .

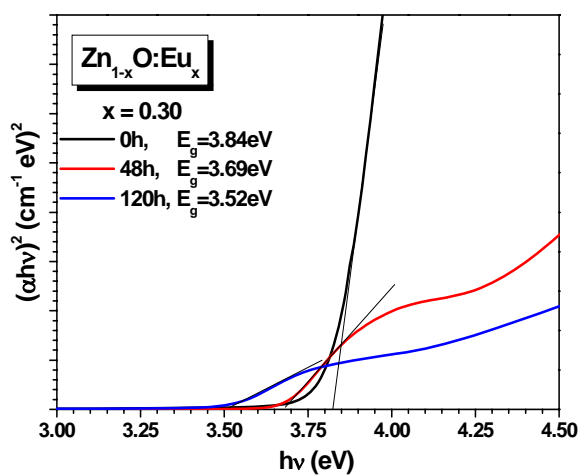
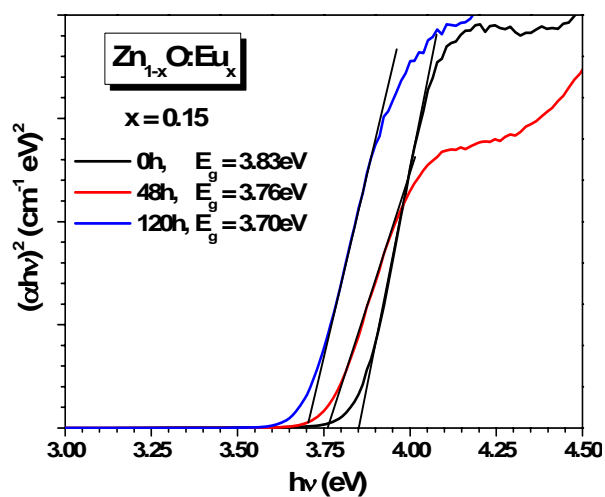
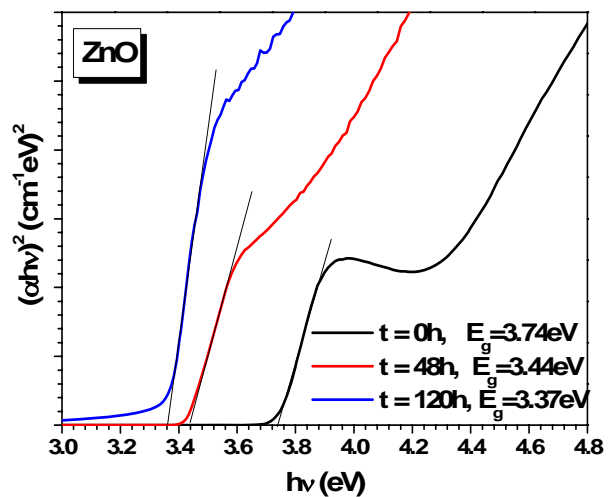


Figure 5.26 UV-vis absorption spectra of bare (top) and  $\text{Eu}^{3+}$ -ions containing (center and below) ZnO aged for different times.

The spectra in figures 5.26 clearly show the strong effect of aging time on the position and broadening of the exciton peak. First, the exciton peaks became broadened when the aging time was prolonged. This band broadening would suggest that aging would promote a less narrow distribution of the crystal size. Next, the red-shift in the exciton peaks with aging time can be attributed to the decrease in quantum confinement due to crystal growth. As the crystal size increases, the band gap shifts towards the bulk value. The observed red-shift in the exciton peak was less pronounced for ZnO containing Eu species when compared to pure ZnO (figure 5.27). This trend can be related to the previously commented inhibition effect of Eu species on crystal growth.

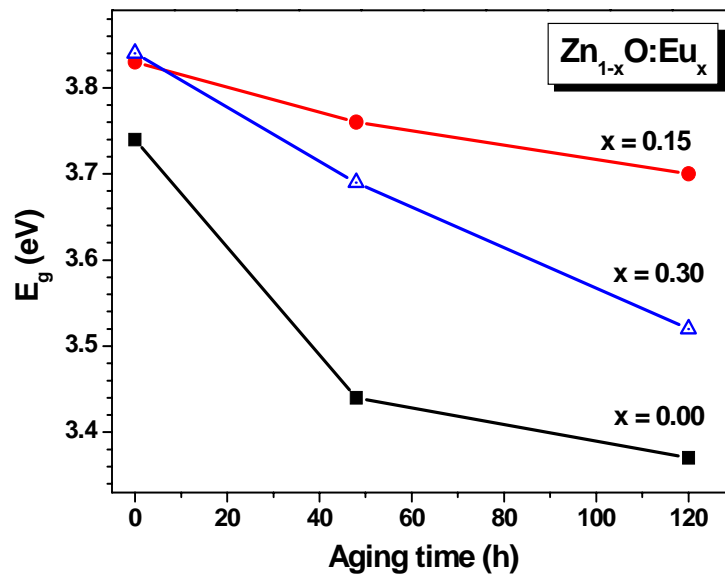


Figure 5.27 Effect of aging time and europium content on the band gap of ZnO nanocrystals.

### ***5.1.2.5 Photoluminescence measurements***

Figure 5.28 shows the emission spectra corresponding to non-aged pure and Eu-containing ZnO nanocrystals powders. One band in the UV region and other one in the visible region were identified. The intensity of the visible emission band, related to oxygen defects, is much higher than that of the exciton emission band. Moreover, the visible/UV intensities ratio increases as  $\text{Eu}^{3+}$  ions content increases, as showed in figure 5.29. As both emission processes compete with each other, the observed trend in the visible/UV intensities ratio could suggest that the visible emission process must involve a step in which the photo-generated hole is trapped efficiently somewhere in the crystal. The rate of this hole trapping process must be much faster than the radiative recombination of the emission exciton. Because of the large surface-to-volume ratio of our ZnO nanocrystals, efficient and fast trapping of photo-generated holes at surface sites can be expected. Schoenmarkers, et al., [80] proposed to  $\text{O}^{2-}$  ions as probable candidate for the trapping of holes at the surface of the crystals. In our case, the contribution of  $\text{Eu}^{3+}$  ions to the generation of defects, that would enhance the visible emission, was understood from the Raman spectroscopy measurements on our samples. However, a more detailed study to identify the actual mechanisms involved with the effect of Eu species on the relative intensities of the emission bands is necessary.

Figure 5.28 also shows that the presence of  $\text{Eu}^{3+}$  ions was conducive to a blue shift of the visible emission peak. This fact would confirm that Eu species are really inhibiting the growth of nanocrystals, in good agreement with our previous discussion based on XRD

and UV-Vis analyses. W. Chen *et al.* [81] suggested that the described behavior could be caused by presence of europium ions inside or on the surface of the ZnO nanocrystals.

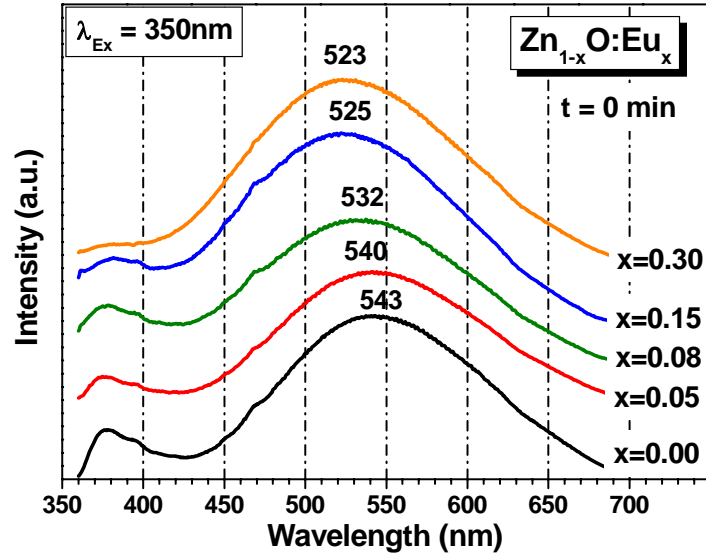


Figure 5.28 Emission spectra, at room temperature, of ZnO nanocrystals with different contents of  $\text{Eu}^{3+}$  ions.

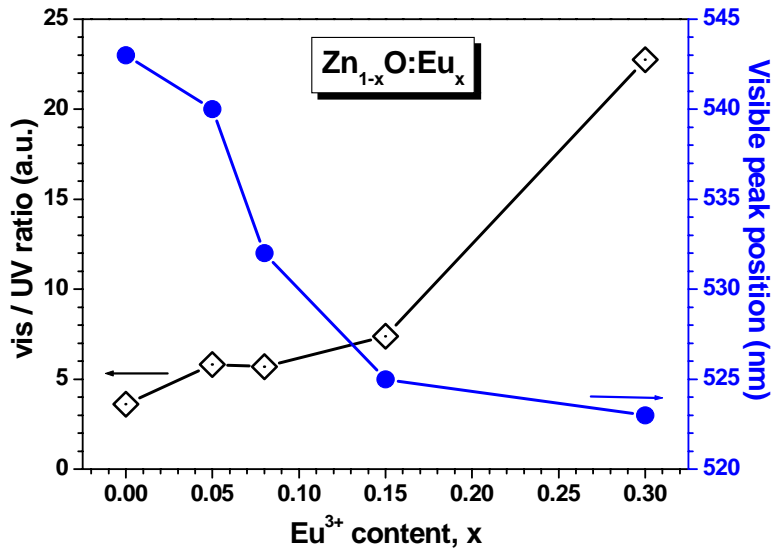


Figure 5.29 Effect of  $\text{Eu}^{3+}$  ions content on visible to UV emission ratio (vis/UV) and visible emission peak of  $\text{Zn}_{1-x}\text{O}:\text{Eu}_x$  nanocrystals. Excitation radiation was 350nm.

As above discussed, only green visible emission was obtained from all samples under excitation by using 350nm; no red emission was observed. This fact would indicate that no energy transfer took place from ZnO to  $\text{Eu}^{3+}$  ions. G. Blasse [26] proposed that the indicator of actual energy transfer from the host to luminescent dopant is the presence of the excitation band of the host excitation in addition to the spectrum corresponding to the dopant emission. Accordingly, we have also measured the excitation and emission spectra of  $\text{Eu}^{3+}$ -ion containing ZnO nanocrystals by using different wavelengths excitation.

Figure 5.30 shows the excitation spectra of ZnO synthesized in presence of  $\text{Eu}^{3+}$  ions ( $x=0.15$ ). The spectra were obtained by monitoring the green emission (525nm) from ZnO nanocrystals and the red emission (614nm) from the  ${}^5\text{D}_0$ - ${}^7\text{F}_2$  transition of Eu species. The band at 345nm can be attributed to the transition from valence band to conduction band in ZnO. In addition to absorption band of ZnO, two well defined peaks centered on 393nm and 464nm, were observed when a wavelength of 614nm was monitored. These peaks correspond to the direct excitation of the  $\text{Eu}^{3+}$  from the ground state  ${}^7\text{F}_2$  to the excited states  ${}^5\text{L}_6$  and  ${}^5\text{D}_2$ , respectively. This result is in good agreement with the spectra obtained by Liu [7] for  $\text{Eu}^{3+}:\text{ZnO}$  nanocrystals synthesized by similar approach.

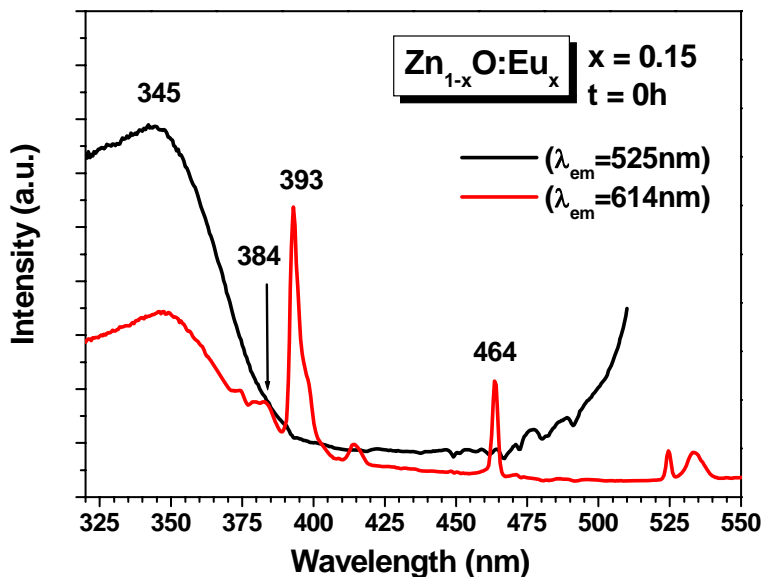


Figure 5.30 Room temperature excitation spectra of no aged  $Zn_{1-x}O:Eu_x$  ( $x=0.15$ ) nanocrystals.

The room temperature emission spectra shown in figure 5.31 were obtained by using the characteristic absorption band for ZnO (345nm), direct excitation of  $Eu^{3+}$  ions (393nm) and one intermediate wavelength excitation (384nm). For the excitation at 345nm, the emission spectrum only shows a broad band centered at 525nm, which can be related to intrinsic defects [39,41]. This fact would indicate that no energy transfer from the host to  $Eu^{3+}$  ions to occur. Exciting directly to europium ions (using a 393nm radiation) only characteristic peaks corresponding to the intra-configurational  ${}^5D_0-{}^7F_1$ ,  ${}^5D_0-{}^7F_2$ ,  ${}^5D_0-{}^7F_3$  and  ${}^5D_0-{}^7F_4$  transitions were obtained. After S.A.M. Lima et al., [65] the high intensity of the hypersensitive transition  ${}^5D_0-{}^7F_2$  indicates that  $Eu^{3+}$  occupies a low symmetry site, but the authors no precise if such ions are either into lattice or surface of ZnO.

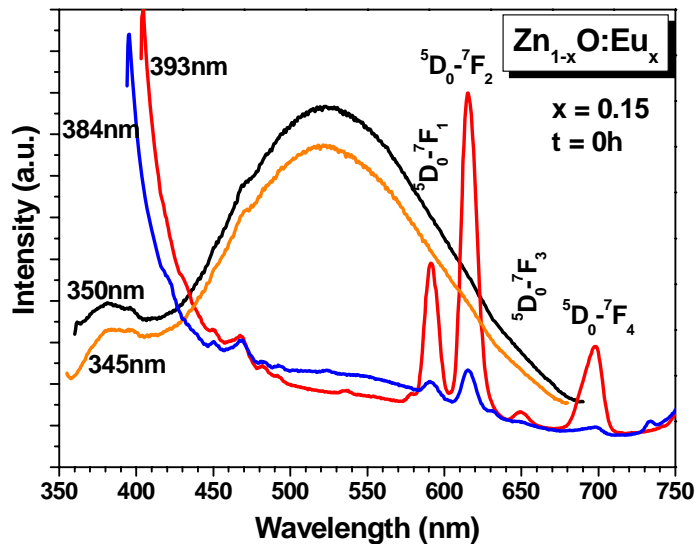


Figure 5.31 Room temperature excitation spectra of no aged  $\text{Zn}_{1-x}\text{O}:\text{Eu}_x$  ( $x=0.15$ ) nanocrystals, monitored under different wavelength excitation.

As was before identified, the 393nm light will directly excite  $\text{Eu}^{3+}$  ions in ZnO nanocrystals, i.e. this photon energy will resonantly excite the  $^5\text{D}_0-^7\text{F}_2$  transition. When the nanocrystals were excited by using the wavelength 384nm, the spectrum consists of a weak broad band and red emission peaks characteristic of  $\text{Eu}^{3+}$  ions. Therefore, it is evident that red luminescence can be observed inclusive under the effect of a non-resonant excitation. Similar behavior was observed in samples with different contents of Eu species (figures 5.32).

On the other hand, based on the dependence of the PL intensity on the excitation energy Ishizumi et al. [5] claimed the actual energy transfer from ZnO to  $\text{Eu}^{3+}$  ions. Therefore, in order to detect energy transfer in the nanocrystals synthesized in this thesis work, the luminescence properties of the sample containing  $\text{Eu}^{3+}$  ( $x=0.15$ ) under different excitation wavelengths was analyzed, as shown figure 5.33.

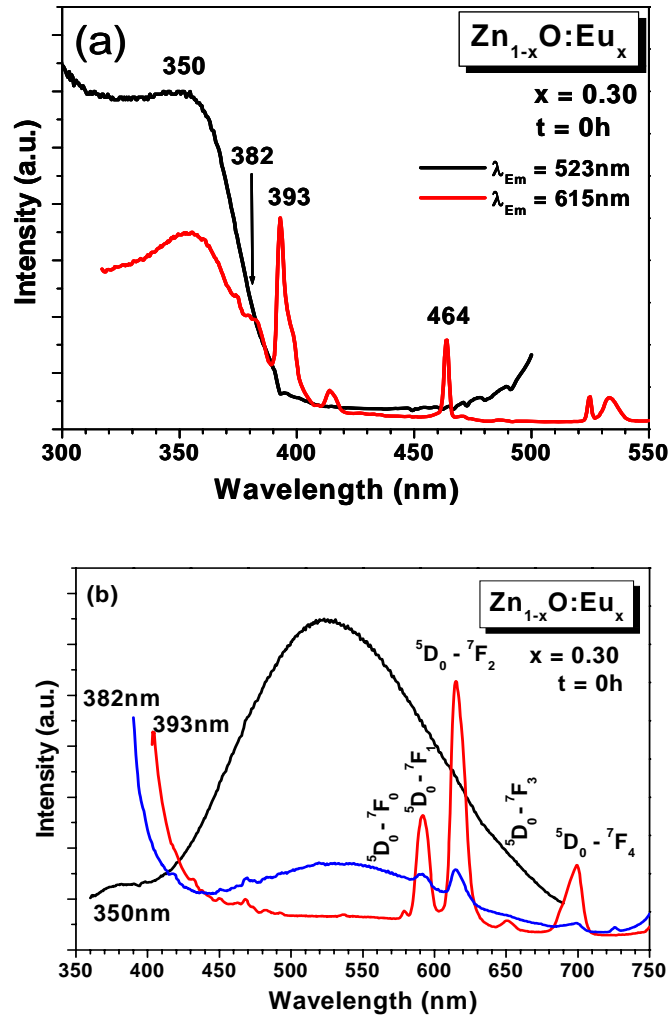


Figure 5.32 (a) Excitation and (b) emission spectra, at room temperature, of Zn<sub>1-x</sub>O:Eu<sub>x</sub> (x=0.30) ZnO nanocrystals no aged, under different wavelength excitation.

The data showed in figure 5.33 evidenced that the strongest emission peaks corresponding to trivalent Eu species were obtained when they were directly excited by using wavelengths of 393nm and 464nm. Although sharp red emission peaks were also observed for excitations with 375nm, 460nm and 470nm, in good agreement with the results presented in reference [5] and showed in figure 3.5, no visible emission from ZnO host was observed.

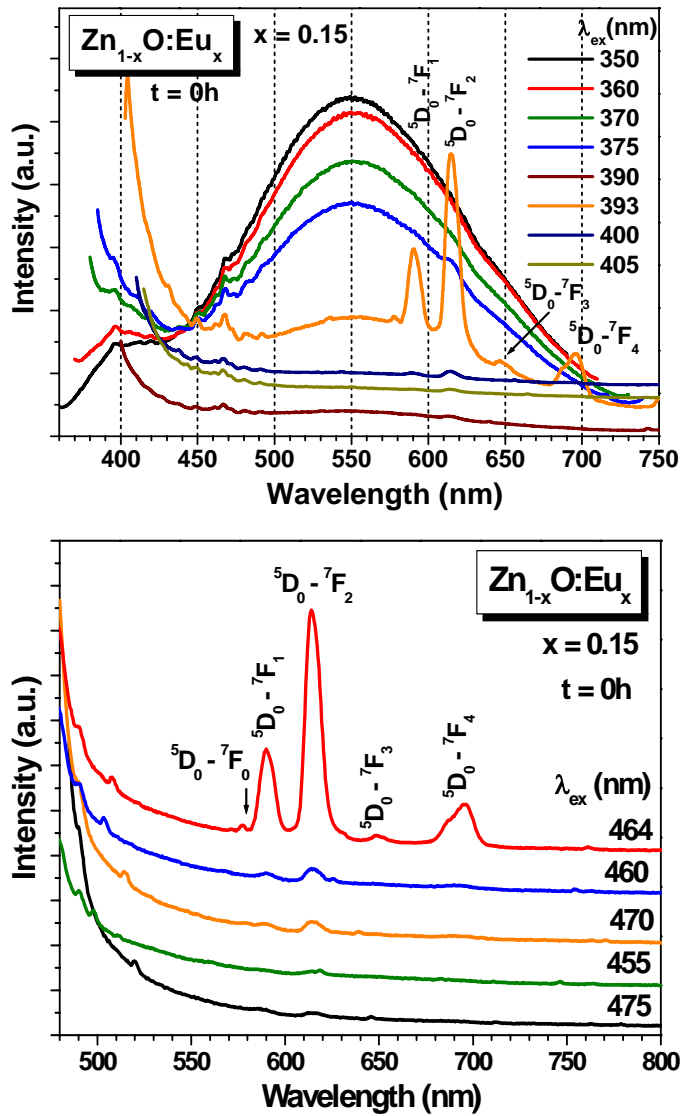


Figure 5.33 Emission spectra, at room temperature, of Zn<sub>1-x</sub>O:Eu<sub>x</sub> (x=0.15) nanocrystals no aged, using different wavelength excitation.

It has been suggested that the luminescence arising from excitation with nonresonant energy at 460nm and 470nm, could be considered as evidence for actual energy transfer from the ZnO host to Eu<sup>3+</sup> ions. On the consideration that that these excitation energies are below the energy gap of ZnO, such energy transfer would occur through the defects of ZnO nanocrystals [5].

From the above discussion for the Eu-ZnO system, synthesized by both thermal decomposition and ethanol solution methods, it could be that: although the thermal decomposition method allow us obtain ZnO nanopowders with wurtzite structure, apparently without Eu-based secondary phases, as shown results of XRD, FT-IR and Raman, the difference of transformation temperatures of precursors (Zinc acetate and europium acetate), obtained by TGA, difficult the actual incorporation of the  $\text{Eu}^{3+}$  ions into ZnO structure, as shown from PL measurements. These measurements confirm conclusively that there is not energy transfer from the ZnO host to  $\text{Eu}^{3+}$  dopant. Also, from the results obtained with the annealed powders, it is possible that the ions would be adsorbed on surface of ZnO nanopowders as amorphous phase. However, since when a dopant, for example a trivalent RE ion, is embedded into a host lattice (even in small concentrations) perturbations may be produced in the neighborhood of the dopant, measurements by other techniques are necessary. For instance, Electron Paramagnetic Resonance (EPR), Extended X-Ray Absorption Fine Structure (EXAFS), or X-Ray Absorption Near-Edge Structure (XANES) could be used in order to determine the lattice distortions around the trivalent RE dopants.

On the other hand, for the nanocrystals obtained through the modified sol-gel method (ethanol solution based), a net effect of the  $\text{Eu}^{3+}$  ions on the UV-vis and PL properties were clearly observed, which evidence a real interaction between ZnO host and  $\text{Eu}^{3+}$  ions, but no necessary the incorporation into ZnO structure. Also, from the XRD results an inhibiting effect on growth of ZnO nanocrystals was observed. The results of Raman, UV-vis y PL allow us to suppose that the europium ions would be adsorbed on ZnO

surface, inhibiting the growth kinetic, which would explain the decreasing of crystallite size of nanocrystals, and also generating surface defects, which would explain the increasing of visible luminescence intensity respect to that of the UV region. However, as was already mentioned for nanopowders synthesized by thermal decomposition, complimentary measurements are necessary in order to confirm or discard it.

## 5.2 Eu-doped Gd<sub>2</sub>O<sub>3</sub>

### 5.2.1 Nanopowders

#### 5.2.1.1 Thermal analysis of precursors and intermediate

The possibility of achieving atomic blending as required by the formation of solid solutions will be strongly dependent on the mixing capability of the constituents. Therefore, any attempt to produce Eu-Gd oxides by mixing and thermal decomposition of their acetates will depend on how similar the individual acetate will behave as a function of temperature. Another important issue related to these TG-DTA analyses is the possibility of determining the most suitable temperature conducive to the complete conversion of the precursors into the desired oxides. On this basis, Figure 5.34 shows the TGA-DTA profiles of Eu(III) and Gd(III) precursor acetate salts, (a), and the intermediate, i.e. the solid obtained after removing the solvent from mixture of Eu and Gd acetate solutions, for Gd<sub>2-x</sub>Eu<sub>x</sub>O<sub>3</sub>, x=0.08, (b). Three decomposition stages are clearly distinguished in the TG profile for precursors. The first stage at low temperature is attributed to the evaporation of adsorbed moisture and crystallization water from the acetate salts. This first step was not observed in the intermediate since it was previously heated at 200°C to remove solvent and any residual content of water. The second step ends at around 400°C and corresponds to the almost complete decomposition of the acetate salts. There is a last step that is completed at 650°C for both, the Eu(III) and Gd(III) precursors suggesting the end of the thermal decomposition processes and complete crystallization of the oxide phase. The similarities in the TG behavior of both precursors suggest the possibility of achieving actual doping of Gd-oxides with Eu species on the consideration that proper mixing conditions for both RE ions are provided.

Excluding the first weight loss step, the TG-DTA profile of the intermediate (figure 5.34-b) was very similar to the profiles corresponding to each individual acetate precursor. The well defined exotherm at 350°C is in good agreement with the observed drastic drop in weight attributed to the thermal decomposition of the acetates. The total weight loss was around 50% for precursor acetate salts and 44% for the mixed intermediate. Similar behaviors were observed for pure and Eu doped Gd-oxide at 'x' values other than 0.08. Accordingly, temperatures above 700°C were selected.

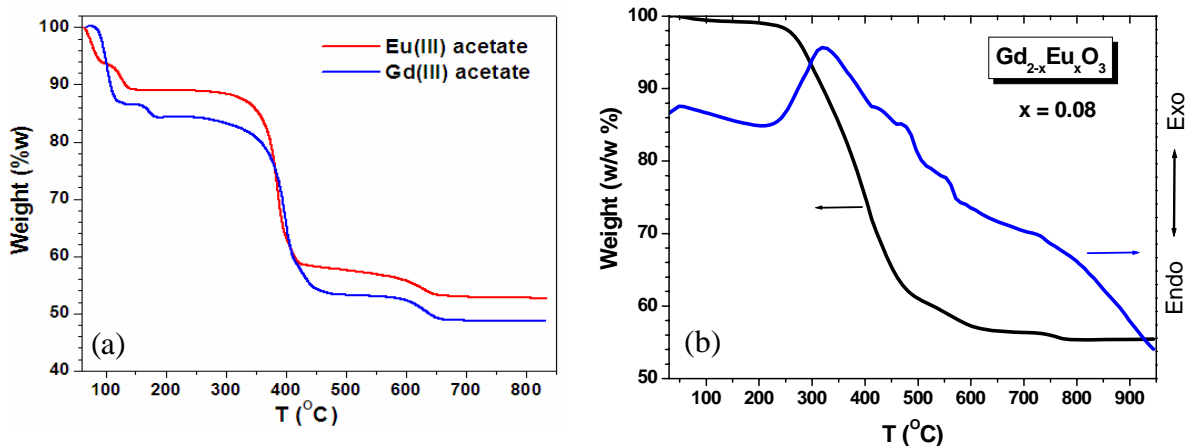


Figure 5.34 a) TGA profiles for Gd(III) and Eu(III) acetate salts; b) TGA-DTA profiles of  $Gd_{2-x}Eu_xO_3$  ( $x=0.08$ ) intermediate.

### 5.2.1.2 Structural characterization

Figure 5.35 shows the XRD patterns of the intermediate and annealed products of pure and  $Eu^{3+}$ -doped  $Gd_2O_3$  ( $x=0.05$ ) powders. The amorphous nature of the intermediates results evident. In turn, the XRD patterns of annealed powders showed very sharp peaks corresponding to cubic  $Gd_2O_3$  phase (JCPDS card N° 12-0797). As shown in the same figure, the peaks sharpness increased when higher annealing temperatures were

considered. This trend is explained in terms of the enlargement of the crystal size in the oxide. The XRD patterns of Figure 5.36 evidence that only the cubic phase of host Gd oxide was obtained for all contents of Eu ions. No transition to monoclinic  $Gd_2O_3$  was observed. The variation in average crystallite size with the annealing temperature and 'x' values is shown in figure 5.37. The average crystallite sizes were 29nm, 36nm and 41nm for 750°C, 850°C and 950°C, respectively. This rising trend in crystallite size with annealing temperature is attributed to the enhancement of intergrain diffusional processes at higher temperatures. The data in figure 5.36 also suggests that there is no remarkable effect of  $Eu^{3+}$  content on the average crystallite size. This behavior is in good agreement with A.M. Pires, *et al.* who reported the synthesis of  $Eu^{3+}$ -doped  $Gd_2O_3$  by a precipitation method [19].

Table 5.1 and figure 5.38 summarize the influence of the annealing temperature and doping level, 'x', on the dimension of the lattice parameter 'a'. The data suggests the negligible influence of annealing temperature on the lattice parameter. Nevertheless, a small but noticeable increment on the lattice parameter was observed when the 'x' value varied from 0.01 to 0.30. This variation of the lattice parameter can be attributed to the actual substitution of  $Gd^{3+}$  ions (0.94Å, ionic radii) by  $Eu^{3+}$  ions (0.95Å) in the  $Gd_2O_3$  lattice. The lattice parameter for pure Gd oxide (x=0.00) is in good agreement with the value for the bulk (10.813Å).

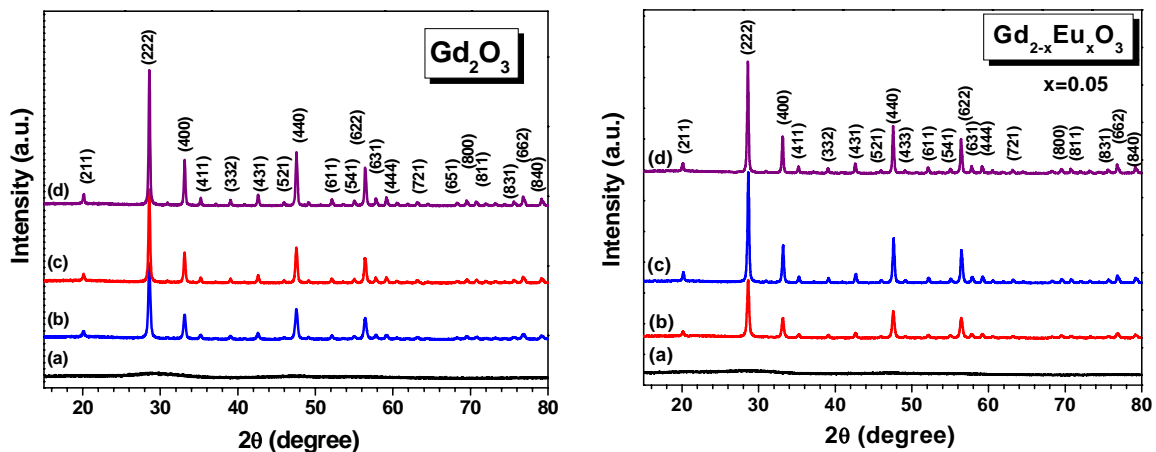


Figure 5.35 XRD patterns of pure  $\text{Gd}_2\text{O}_3$  and  $\text{Gd}_{2-x}\text{Eu}_x\text{O}_3$  ( $x=0.05$ ) before (a) and after annealing at (b)  $750^\circ\text{C}$ , (c)  $850^\circ\text{C}$ , and (d)  $950^\circ\text{C}$  for 2h. All peaks correspond to cubic  $\text{Gd}_2\text{O}_3$  phase.

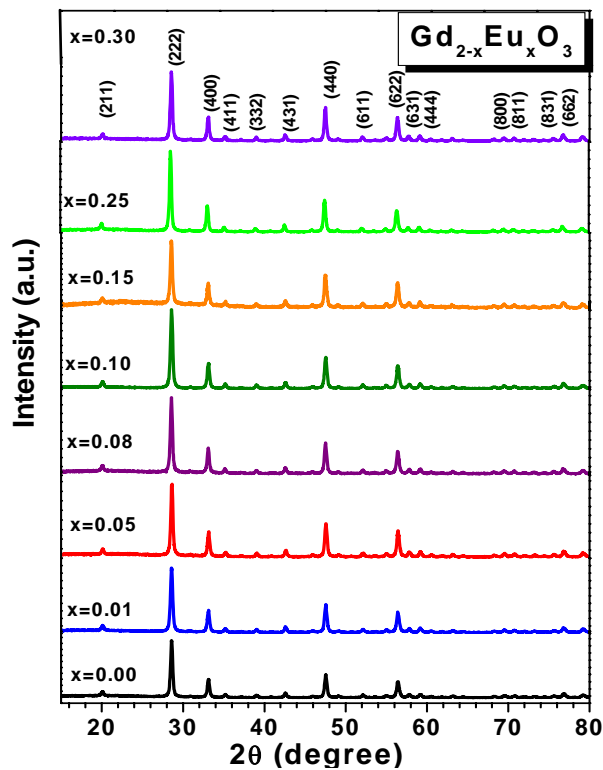


Figure 5.36 XRD patterns of  $\text{Gd}_{2-x}\text{Eu}_x\text{O}_3$  powders synthesized at different atomic fractions of Eu ions, 'x'. The solids were crystallized after annealing in air at  $750^\circ\text{C}$  for 2h. All peaks correspond to cubic  $\text{Gd}_2\text{O}_3$  host structure.

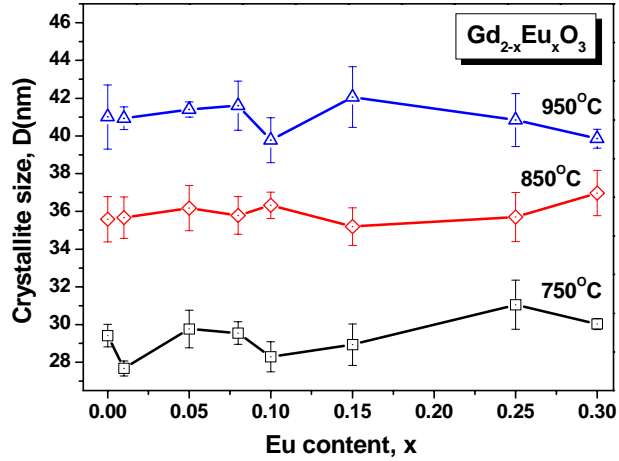


Figure 5.37 Effect of annealing and  $\text{Eu}^{3+}$  content, 'x', on the average crystallite size of  $\text{Gd}_{2-x}\text{Eu}_x\text{O}_3$  nanocrystalline powders. The continuous lines only are as visual help.

Table 5.1 Variation of lattice parameter of  $\text{Gd}_{2-x}\text{Eu}_x\text{O}_3$  nanopowders annealed at different temperatures.

x	$a$ (Å)		
	750°C	850°C	950°C
0.00	10.816±0.002	10.817±0.001	10.813±0.001
0.01	10.818±0.001	10.810±0.002	10.802±0.004
0.05	10.809±0.004	10.799±0.006	10.816±0.001
0.08	10.824±0.002	10.823±0.002	10.822±0.001
0.10	10.818±0.002	10.816±0.001	10.806±0.005
0.15	10.827±0.002	10.822±0.001	10.821±0.001
0.25	10.827±0.001	10.823±0.001	10.825±0.001
0.30	10.826±0.002	10.830±0.001	10.825±0.001

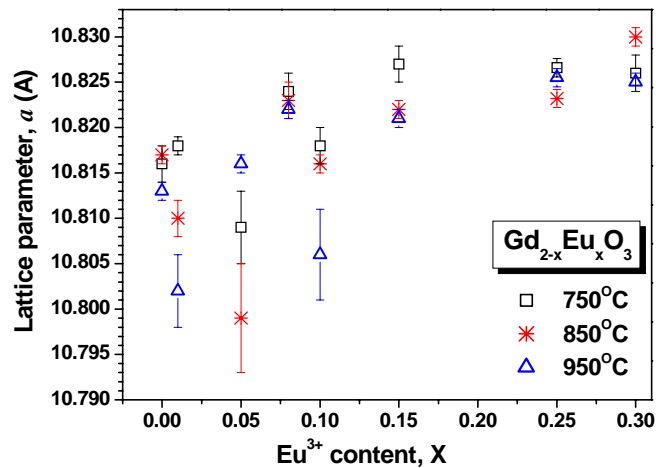


Figure 5.38 Effect  $\text{Eu}^{3+}$  ions content on lattice parameter of  $\text{Gd}_{2-x}\text{Eu}_x\text{O}_3$  nanopowders annealed at different temperatures.

### 5.2.1.3 Infrared analysis

Structural information proved by XRD was complemented by FTIR spectroscopy (Figure 5.39). Intense bands at  $1535\text{cm}^{-1}$  and  $1419\text{cm}^{-1}$  were observed for the intermediate. These bands are assigned to symmetric and asymmetric C=O stretching vibration modes in acetate species in the precursor salts, respectively. FT-IR spectra of the samples after annealing only showed a sharp band at  $540\text{cm}^{-1}$ , associated with the vibration of the Gd-O bond. The presence of this band evidences the formation of the host  $\text{Gd}_2\text{O}_3$  structure, which confirms the XRD results. The absence of the bands of acetate species suggests the complete thermal decomposition of the intermediate. This fact is of great importance to assure optimum optical properties in synthesized nanophosphors. Similar spectra were obtained for bare  $\text{Gd}_2\text{O}_3$  and doped with  $\text{Eu}^{3+}$  for all contents.

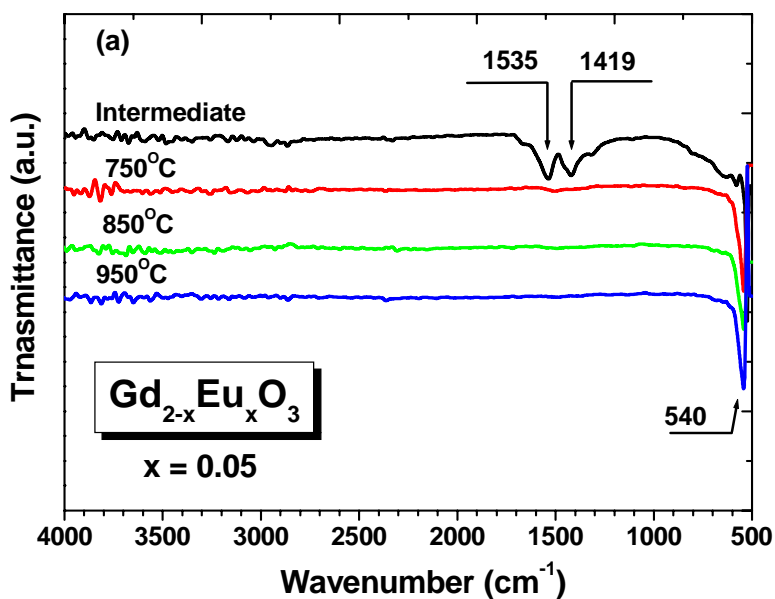


Figure 5.39 FT-IR spectra of  $\text{Eu}^{3+}$ -doped  $\text{Gd}_2\text{O}_3$  precursor and annealed phosphor. Acetates group ( $1535\text{cm}^{-1}$  and  $1419\text{cm}^{-1}$ ) and metal-O bond ( $540\text{cm}^{-1}$ ) bands are clearly identified.

#### 5.2.1.4 Raman measurements

As was shown by XRD results, nanocrystalline  $\text{Eu}^{3+}$ -doped  $\text{Gd}_2\text{O}_3$  exhibited cubic structure at room temperature. The corresponding space groups are  $Ia\bar{3}$ ,  $T_h^7$ ,  $Z=16$  [58]. The actual structure is body-centered cubic and the unit cell contains the primitive structure twice, so that only eight unit formulas must be used to theoretically determine the number of vibrations [57]. The irreducible representations for the optical ( $\Gamma_{op}$ ) and acoustical ( $\Gamma_{ac}$ ) modes are:

$$\begin{aligned}\Gamma_{op} &= 4A_g + 4E_g + 14F_g + 5A_{2u} + 5E_u + 16F_u, \\ \Gamma_{ac} &= F_u\end{aligned}\tag{5.1}$$

$A_g$ ,  $E_g$ , and  $F_g$  are Raman active,  $F_u$  is IR active and  $A_{2u}$  and  $E_u$  are inactive. Therefore, on the whole, twenty-two Raman lines can be predicted. However, it has been reported that the spectra of sesquioxides are often very complex, depending on the laser wavelength, because of the presence of signals due not only to the Raman scattering, but also to the photoluminescence of the RE ions [82]. In these cases, the spectrum seems to be very different from those of the other C-type oxides making difficult any comparison. So, not all sesquioxides are suitable for Raman analysis.

Figure 5.40 shows Raman spectra of  $\text{Gd}_2\text{O}_3$  and  $\text{Eu}^{3+}$ -doped  $\text{Gd}_2\text{O}_3$  nanocrystalline powders annealed at  $950^\circ\text{C}$  for 2 hours in air. In addition to several weaker bands, a strong band at  $362\text{cm}^{-1}$  is observed for the pure  $\text{Gd}_2\text{O}_3$  sample which, in general, is in good agreement with data available in the literature [57,82,83], which has been assigned for the  $F_g$  mode and  $A_g + F_g$  combination [57,82,83]. The strong intensity of this band

indicates a large polarizability change during the atoms vibration. Therefore, this band is expected to be one of the most sensitive to changes in chemical bonding.

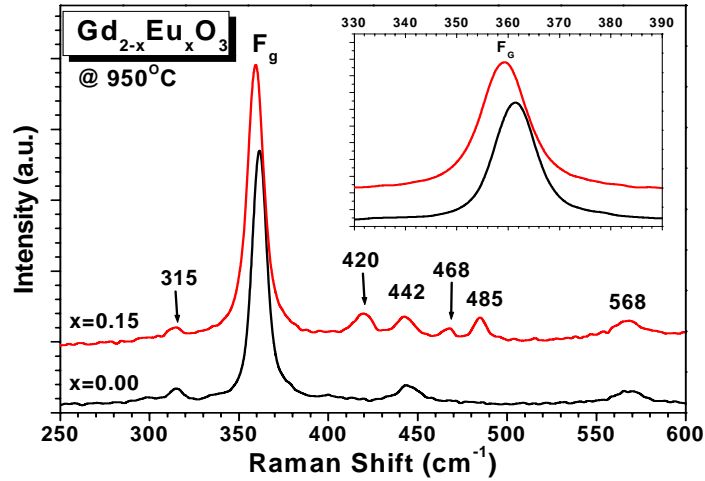


Figure 5.40 Raman spectra of bare and containing  $\text{Eu}^{3+}$  ions ( $x = 0.15$ )  $\text{Gd}_2\text{O}_3$  annealed at  $950^\circ\text{C}$ . The shift of the  $F_g$  band is shown inset.

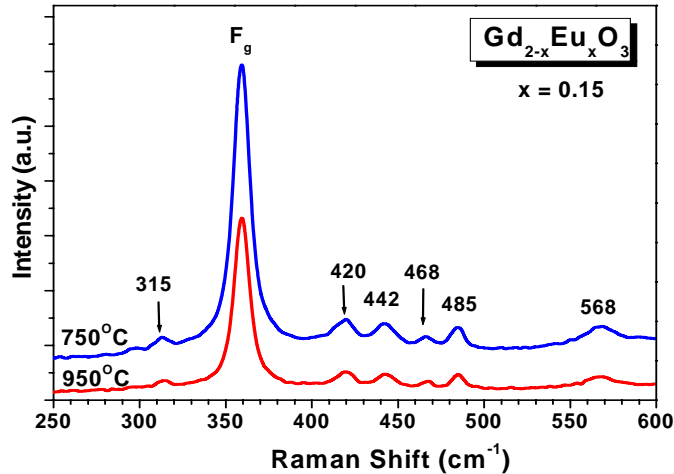


Figure 5.41 Raman spectra of  $\text{Gd}_{2-x}\text{Eu}_x\text{O}_3$  nanocrystalline powders, with  $x=0.15$  annealed at different temperatures.

The Raman spectrum of the  $\text{Eu}^{3+}$ -doped  $\text{Gd}_2\text{O}_3$  ( $x=0.15$ ) annealed at  $950^\circ\text{C}$  is also shown in figure 5.40. In this spectrum, a red shift of the strong  $F_g$  band was evident. This shift can be attributed to the actual incorporation of  $\text{Eu}^{3+}$  ions into  $\text{Gd}_2\text{O}_3$  structure, which is in

agreement with the XRD and PL considerations. Moreover, additional weak bands centered on 420, 468 and 485 $\text{cm}^{-1}$  were also identified. These bands can be assigned to Eu-based oxides, present in very small quantities, enough that was not detected by XRD. Similar spectra were obtained for different annealing temperature (figure 5.41).

### 5.2.1.5 Elemental analysis

SEM-EDS was used to confirm the qualitative elemental composition of the powders. Figure 5.42 shows the EDS spectrum of the Eu-doped Gd oxide powders synthesized at  $x=0.30$ . The presence of Gd, Eu and oxygen is confirmed by the corresponding EDS peaks associated to the different electronic transition for each species. Also, a very weak peak corresponding to carbon (from the sample holder and/or chamber) was observed. The absence of any other element in the EDS spectrum suggests the high purity of the nanocrystalline powders.

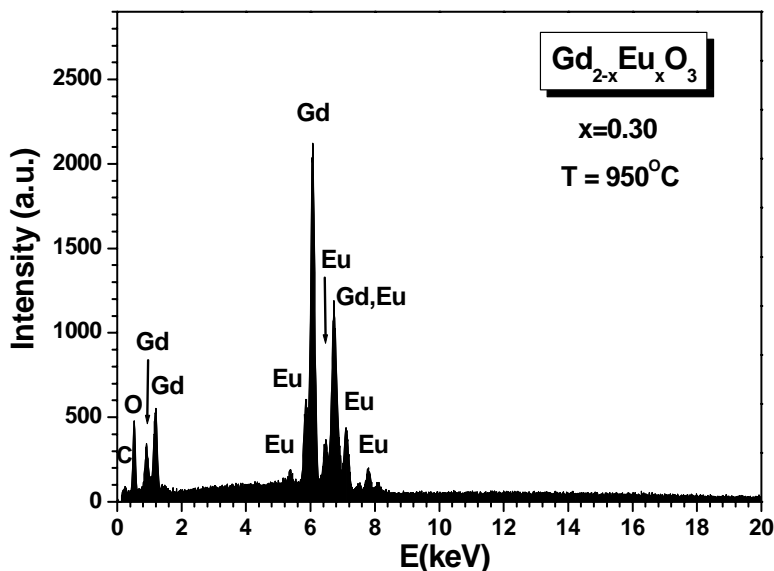


Figure 5.42 EDS spectrum for nanocrystalline Eu-doped  $\text{Gd}_2\text{O}_3$  powders,  $x=0.30$ , annealed at  $950^\circ\text{C}$ .

### 5.2.1.6 Photoluminescence measurements

Figure 5.43 shows the excitation spectra, recorded at room temperature, for  $\text{Eu}^{3+}$ -doped  $\text{Gd}_2\text{O}_3$  ( $x=0.05$ ) annealed at different temperatures. The large band around 250nm is assigned to the  $\text{O}^{2-} \rightarrow \text{Eu}^{3+}$  charge transfer band (CTB), which is due to the charge transfer from the O 2p state to the charge transfer state (CTS) of the  $\text{Eu}^{3+}$  ion, because this ion trends to capture one electron in order to achieve a more stable half-filled shell state (4f configuration). The weak ones at 274nm and 312nm are related to internal  $\text{Gd}^{3+}$  transitions, and these transitions can be observed due to the  $\text{Gd}^{3+} \rightarrow \text{Eu}^{3+}$  energy transfer process. The weak and narrow bands above 330nm are assigned to transitions of  $\text{Eu}^{3+}$  [11,25,63]. On a common sample-weight basis for all PL measurements, the observed increase of the intensity of the CTB can be attributed to the enhancement on crystallinity of the solids, as suggested by XRD analysis.

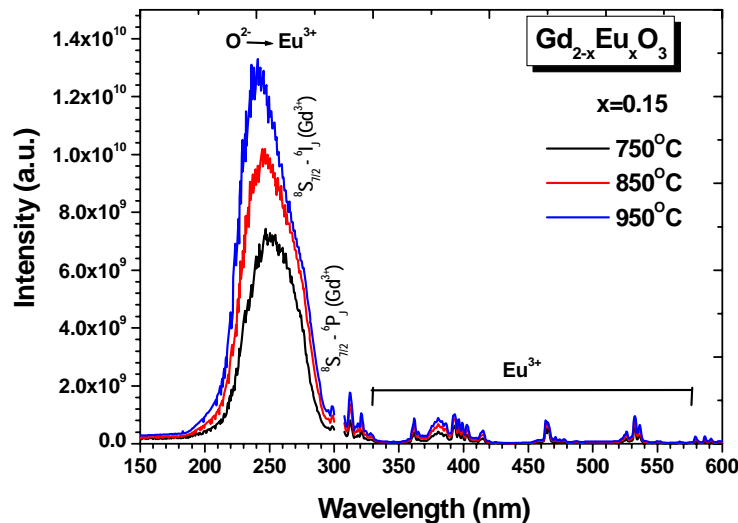


Figure 5.43 Excitation spectra of  $\text{Gd}_{2-x}\text{Eu}_x\text{O}_3$  nanocrystalline powders,  $x=0.15$ , for different annealing temperatures. The spectra were taken monitoring the 611nm emission line.

The effect of  $\text{Eu}^{3+}$  atomic fraction, 'x', on the excitation behavior of doped  $\text{Gd}_2\text{O}_3$  powders is shown in figure 5.44. The maximum intensity was obtained for  $x=0.15$ . Pelova *et al.*, [84] suggested that an increase of the CTB transition energy would be due to the influence of  $\text{Eu}^{3+}$  ions from the first coordination sphere of the activator or because of the increase of the separation distance between  $\text{Eu}^{3+}$  caused by  $\text{O}^{2-}$  ions.

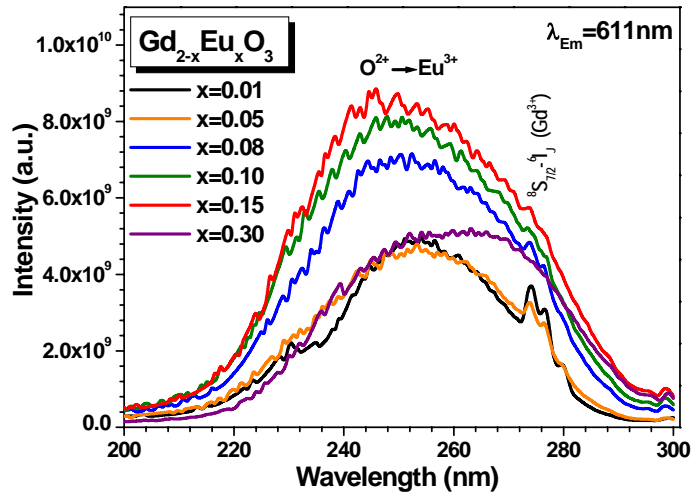


Figure 5.44 Excitation spectra of  $\text{Gd}_{2-x}\text{Eu}_x\text{O}_3$  nanocrystalline powders annealed at  $750^\circ\text{C}$  for different Eu contents, 'x'. The spectra were taken monitoring the 611nm emission line.

Figure 5.45 shows the room temperature emission spectra of  $\text{Gd}_{2-x}\text{Eu}_x\text{O}_3$  nanocrystalline powders synthesized at  $x=0.15$  and annealed at different temperatures. The spectra exhibit the five groups of distinctive emission peaks in the 550nm-720nm range. These emission peaks can be related to each one of the  ${}^5\text{D}_0 \rightarrow {}^7\text{F}_J$  ( $J=0,1,2,3,4$ ) transitions of  $\text{Eu}^{3+}$ , which are characteristic of  $\text{Eu}^{3+}$  ion within a crystallized cubic phase. Our findings are in good agreement with the level energies reported by Buijs [63]. The strongest emission peak at 611nm is caused by the electron dipole transition of  $\text{Eu}^{3+}$  ( ${}^5\text{D}_0 \rightarrow {}^7\text{F}_2$ ) corresponding to red luminescence. The splitting of ( ${}^5\text{D}_0 \rightarrow {}^7\text{F}_1$ ), ( ${}^5\text{D}_0 \rightarrow {}^7\text{F}_3$ ), and

( $^5D_0 \rightarrow ^7F_4$ ) transitions, due to crystal field effect, confirms the actual incorporation of  $\text{Eu}^{3+}$  ions in the host gadolinium oxide structure.

As was above mentioned, in the cubic structure,  $\text{RE}^{3+}$  ions would occupy two sixfold-coordinated distinctly non equivalent sites with  $C_2$  and  $S_6$  point symmetry and which differ from each other in the position of  $\text{RE}^{3+}$  ion relative to the vacancy oxygen [59,61]. Therefore, the different transitions can be assigned to the symmetry sites,  $C_2$  and  $S_6$  as shown in the figure 5.45. The increase of the luminescence intensity at higher temperatures of annealing is attributed to the crystal growth, evidenced by XRD measurements. In our case, the highest intensity was obtained in nanophosphors annealed at  $950^\circ\text{C}$ . The intensity of the emission peak at 611nm was strongly dependent on the composition, i.e., the atomic fraction of Eu ions in the host Gd oxide. Figure 5.46 shows the RT emission spectra of the solids synthesized at different 'x' values obtained using the CTB (250nm) as the excitation wavelength.

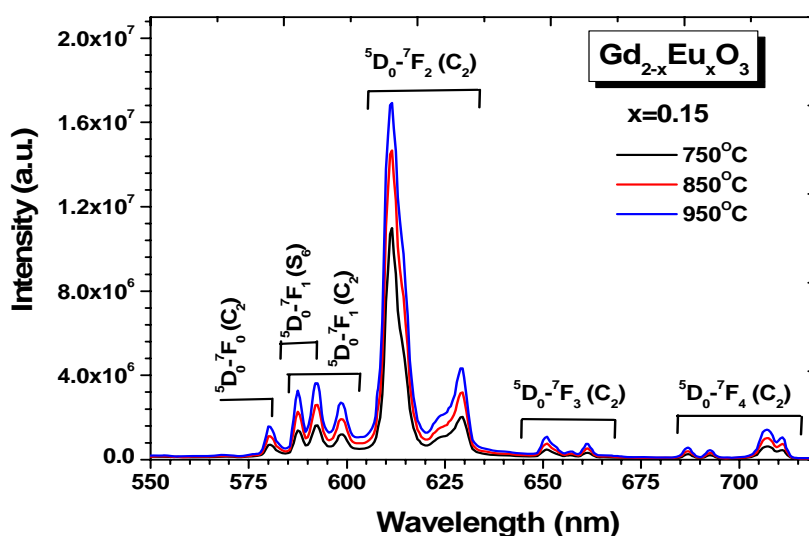


Figure 5.45 Emission spectra at room temperature of  $\text{Gd}_{2-x}\text{Eu}_x\text{O}_3$  nanocrystalline powders ( $x=0.15$ ), annealed at different temperatures. The spectra were obtained by using a 250nm UV as excitation light. Similar behavior was observed for all  $\text{Eu}^{3+}$  contents.

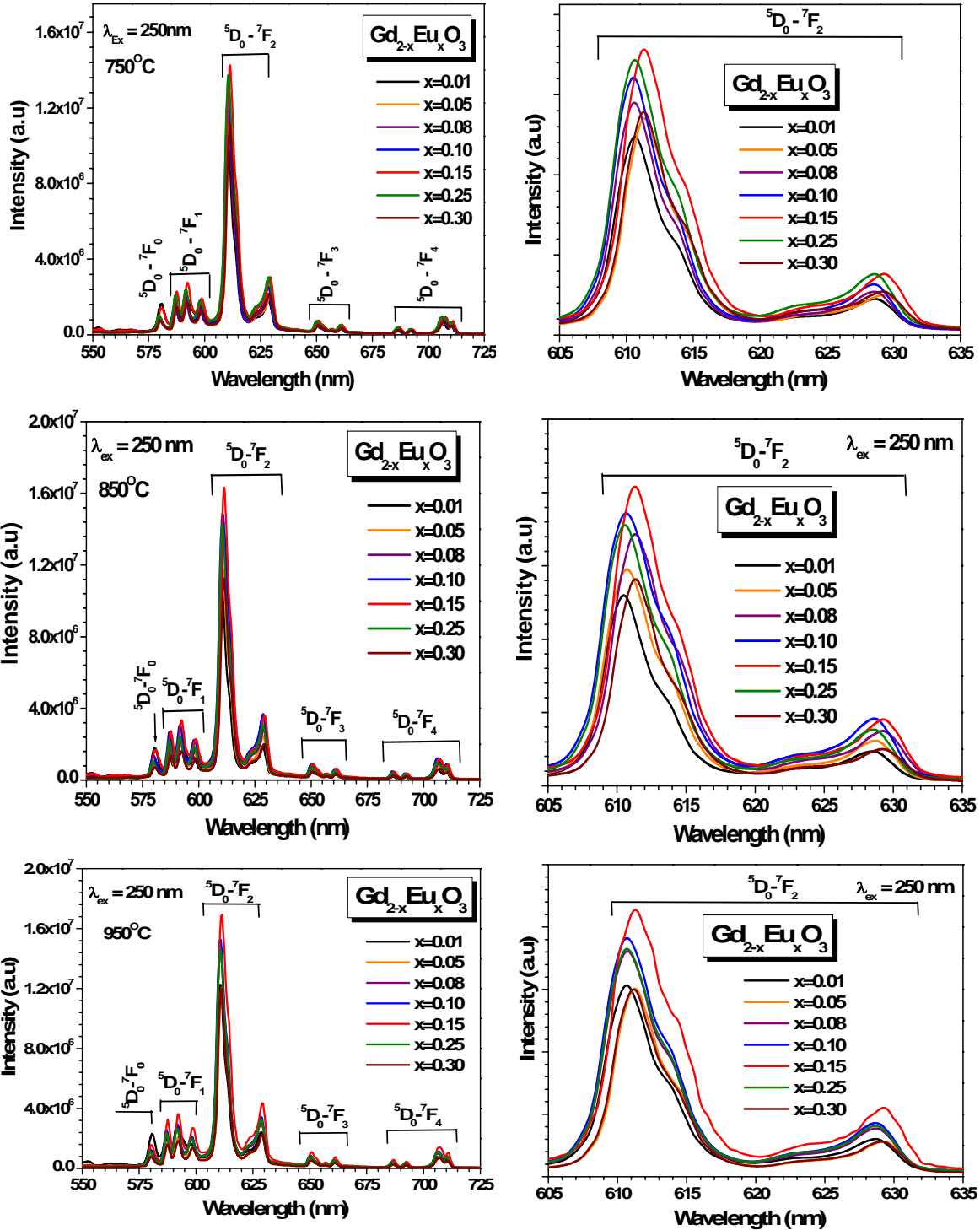


Figure 5.46 RT-Emission spectra Gd<sub>2-x</sub>Eu<sub>x</sub>O<sub>3</sub> nanopowders with different 'x' values annealed at different temperatures for 2 hours. Detail of the <sup>5</sup>D<sub>0</sub>-<sup>7</sup>F<sub>2</sub> transition, are shown on the right for each case.

Figure 5.47-a summarizes the variation of the relative luminescence intensity at 611nm with ‘x’ values, on a common sample-weight condition. As seen, the maximum intensity was attained at x=0.15 (7.5% w/w of Eu). This particular composition is lower than the reported for Eu (10% w/w)-doped Gd oxide powders having similar average crystallite size (41nm) but synthesized by liquid-phase reaction [66], but comparable to the 8 %w/w of Eu observed for 25nm particles synthesized by combustion [85]. The concentration quenching in the luminescence intensity observed for x>0.15 can be ascribed to transfer energy from RE ions to nearby quenching centers; as the Eu<sup>3+</sup> concentration increases, the distance between Eu<sup>3+</sup> ions decreases favoring the effective energy transfer between Eu<sup>3+</sup> species. This promotion of the energy transfers between Eu<sup>3+</sup> species would cause the migration of the excited states to the quenching sites were the energy will be dissipated by nonradiative processes. Although the same phenomenon has been observed in other phosphors, the optimal concentration, and luminescence in general, depends of several factors, such as material host, synthesis method and conditions, solvent, precursor salts, etc. [85].

The mechanism involved with the luminescence quenching in solid state materials can be determined by analyzing the values of the critical constants in the following equations [86]:

$$f(x) = [1 + \beta(x)^{s/3}]^{-1}$$

$$\frac{I}{x} = K [1 + \beta(x)^{s/3}]^{-1} \quad (5.2)$$

where ‘x’ is the dopant concentration, I is the relative emission intensity, K and  $\beta$  are constants for the same excitation conditions for a given host material, and s is the mutual

interactions constant, which value indicates the nature of the interaction in the quenching phenomena. When  $s$  is equal to 6, 8 or 10, the luminescence quenching will result from the mutual reactions between dipole and dipole-dipole, dipole-quadrupole or quadrupole-quadrupole interactions, respectively. These interactions are electrostatic in origin. It has been also proposed that a 's' value of 3 would indicate that mutual interactions comes from exchange interactions between  $\text{Eu}^{3+}$  [87]. This interaction arises from requirement of the antisymmetry of the electronic wavefunction for the system consisting of a donor ion and an acceptor ion. These mechanisms differ from one another in the dependence of the transfer rate on donor-acceptor distance, but common to all is the condition that an overlap between the donor emission spectrum and the acceptor absorption spectrum is essential for the transfer to occur.

D. Wang et al. [88] have proposed that when 'x' in the above equation is larger than the critical quenching concentration; then  $\beta(x)^{s/3} \gg 1$  and equation (5.2) can be approximated by ('K' is a constant):

$$\frac{I}{x} = \frac{K'}{\beta(x)^{s/3}} \quad (5.3)$$

Figures 5.47-b, -c and -d show the linearized plot of above equation for  $\text{Eu}^{3+}$ -doped  $\text{Gd}_2\text{O}_3$  powders annealed at 750°C, 850°C and 950°C, respectively. The estimated value of  $s$  are summarizes in the table 5.2, being 3 for all cases. This value is in good agreement to the one reported for nanocrystalline  $\text{Gd}_2\text{O}_3:\text{Eu}^{3+}$  powders synthesized by combustion

process [87]. Accordingly, the luminescence quenching in  $\text{Eu}^{3+}$ -doped  $\text{Gd}_2\text{O}_3$  nanocrystalline powders would result from exchange interactions.

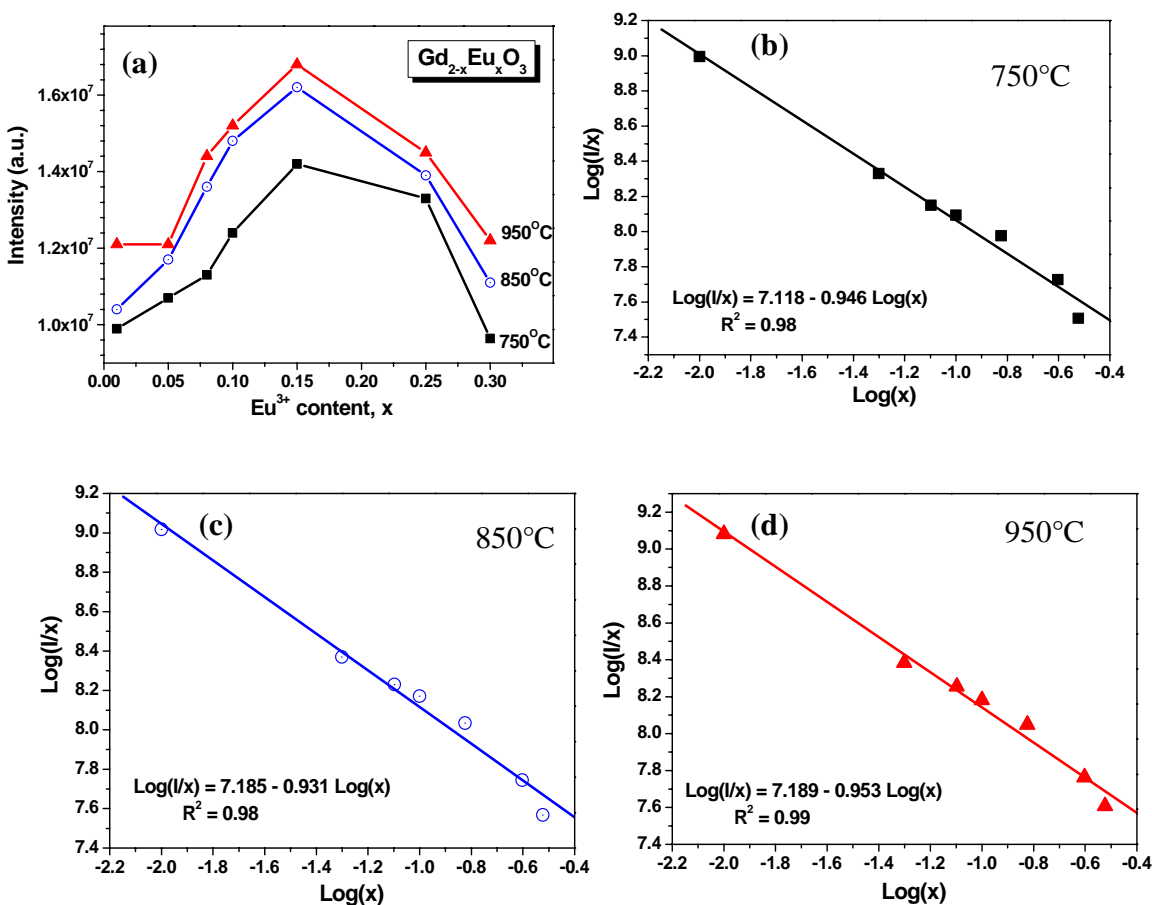


Figure 5.47 Relation luminescence at 611nm and  $\text{Eu}^{3+}$  concentration (a), and relationship between  $\text{Log}(I/x)$  and  $\text{Log}(x)$  in  $\text{Eu}^{3+}$ -doped  $\text{Gd}_2\text{O}_3$  nanoparticles annealed at 750°C (b), 850°C (b) and 950°C (c).

Table 5.2 Mutual interaction constant ( $s$ ) for  $\text{Gd}_{2-x}\text{Eu}_x\text{O}_3$  nanocrystalline powders annealed for 2 hours at different temperatures. The values were obtained from slope of plots shown in figure 5.47.

T(°C)	750	850	950
slope	$-(0.946 \pm 0.052)$	$-(0.931 \pm 0.055)$	$-(0.953 \pm 0.046)$
S	$2.85 \pm 0.156$	$2.79 \pm 0.165$	$2.86 \pm 0.138$

### *5.2.1.7 Preliminary magnetic characterization*

As mentioned, Gd-chelates are commonly used as contrast agent in MRI thanks to the magnetic properties of Gd species. Nevertheless, these Gd-compounds tend to be non-specific and cause a rapid accumulation in the liver; therefore, a very short time-imaging window is available [13]. The possibility of using the combined effect of the luminescent properties from  $\text{Eu}^{3+}$ -doped  $\text{Gd}_2\text{O}_3$  and the ferromagnetic properties from  $\text{Fe}_3\text{O}_4$ , as core-shell nanoparticles, have also been suggested [14,89].

It is known that metallic Gadolinium is the only truly ferromagnetic RE element and its Curie temperature 293K [52] is the highest among the rare earths. The  $\text{Gd}^{3+}$  ion has an  $^8\text{S}_{7/2}$  ground state and, consequently, it can be considered an isotropic ion ( $L=0$ ) with magnetic properties originated from spin only. In  $\text{Gd}^{3+}$  compounds the crystal field effect is of second order and acts on magnetic properties at the low temperatures, cubic- $\text{Gd}_2\text{O}_3$  has a complex antiferromagnetic structure below 1.6K [58]. A paramagnetic behavior has also been reported for cubic- $\text{Gd}_2\text{O}_3$  [90,91].

The magnetic susceptibility of polycrystalline solid solutions  $(\text{Eu}_x\text{Gd}_{1-x})_2\text{O}_3$  with  $x=0.2, 0.4, 0.6, 0.8$ , has been studied by using a null coil pendulum magnetometer and in the temperature range between 95K and 295K [90]. The samples were prepared by mixing the individual oxides in the same molar ratios as in the final product, and firing below the cubic-monoclinic phase transition temperature of  $\text{Eu}_2\text{O}_3$  (1100°C). It was found that the magnetic susceptibility of  $\text{Eu}^{3+}$  ions had the same value as in  $\text{Eu}_2\text{O}_3$  for all values of 'x', i.e. it did not change all concentrations and temperatures. Based on this available

information, we measured the M-H behavior of the nanocrystalline Eu-doped powders synthesized by our method.

Figure 5.48 shows the magnetic behavior of nanocrystalline  $Gd_2O_3$  powders produced by our method and with different content of  $Eu^{3+}$  ions, 'x'. The powders were annealed at  $950^\circ C$  for 2h. Although the solid exhibited a high crystallinity with the actual substitution of Gd by Eu ions, as suggested by our previous characterization, no indication of ferromagnetic behavior was observed. Indeed, the powders were paramagnetic in nature for all  $Eu^{3+}$  contents. This behavior is in agreement with that reported by Grill and Schieber [90].

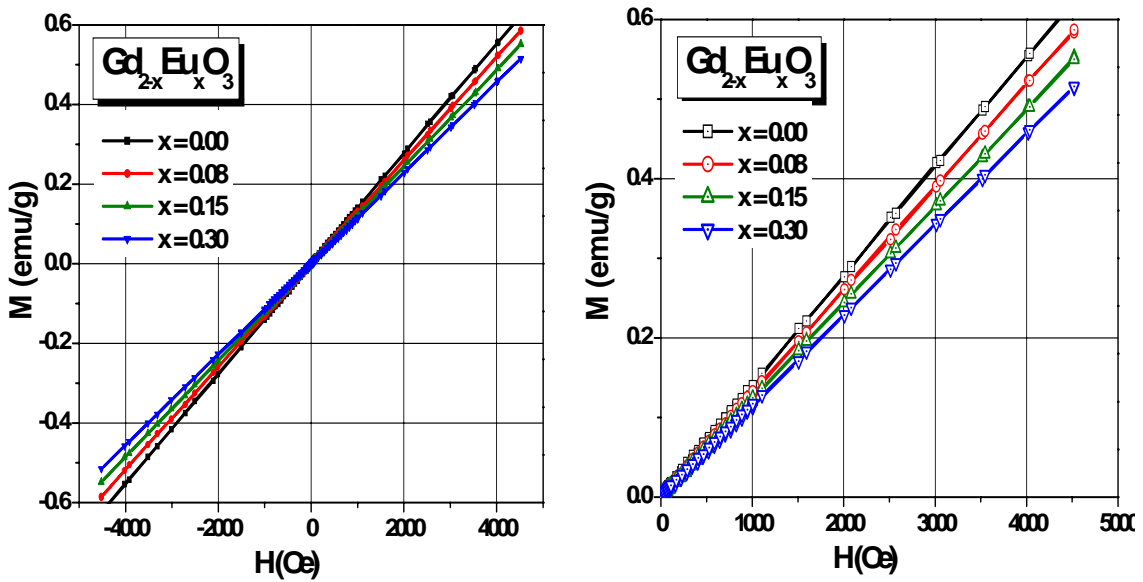


Figure 5.48 Magnetization as function of applied field, at 300K, of  $Eu^{3+}$ -doped  $Gd_2O_3$  nanopowders annealed at  $950^\circ C$ . A typical paramagnetic behavior is observed.

Table 5.3 Magnetic susceptibility, at room temperature, of  $Gd_{2-x}Eu_xO_3$  powders, annealed at  $950^\circ C$ .

x (w/w)	0.00	0.08	0.15	0.30
$\chi$ (emu/Oe.g). $10^{-4}$	1.383	1.296	1.216	1.140

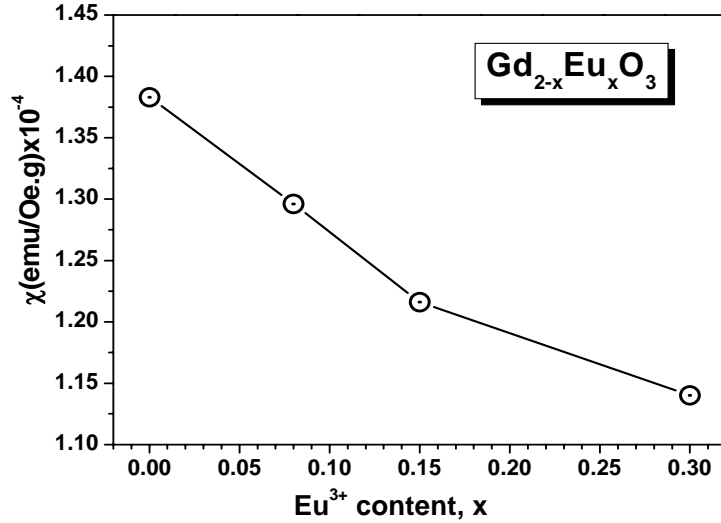


Figure 5.49 Magnetic susceptibility, at room temperature, of  $Gd_{2-x}Eu_xO_3$  nanopowders, annealed at  $950^\circ C$ , as function  $Eu^{3+}$  content. Solid line is only for visual help.

The most remarkable feature was the systematic decrease in the magnetic susceptibility when the atomic fraction of Eu ions was increased (table 5.3 and figure 5.49). This behavior could be explained as follows: in spite that theoretically the  $Eu^{3+}$  has  $J=0$  (see table 2.1), experimentally has been found that it has an effective magneton Bohr number of 3.4, which has been attributed to the mixing of the excited states into the ground state by the field, and to the thermal excitation of these states [52]. However, according to Grill and Schieber,  $Eu^{3+}$  no change its magnetic susceptibility, the decreasing of  $Gd^{3+}$  in  $Gd_{2-x}Eu_xO_3$  leads to a reduction of the magnetic susceptibility. However, more measurements at different temperatures would be necessary in order to define this behavior.

### 5.2.2 Properties of Eu-doped $Gd_2O_3$ Thin films

Pure and RE-doped optical waveguide films have always attracted great technological interest due to their potential applications in integrated optics [92,93]. The good structural,

optical and luminescence properties of  $\text{Gd}_2\text{O}_3$  have enabled this material to be considered a very promising candidate for waveguide applications. Although our research has been based on the materials characterization, any effort oriented towards practical application of Eu- $\text{Gd}_2\text{O}_3$  materials should consider their controlled formation onto suitable substrates forming the so-called thin films. Therefore, based on our previous work, the controlled preparation of homogeneous deposition of Eu-doped Gd oxides onto fused quartz has also been attempted.

#### ***5.2.2.1 Structural and morphological characterization***

Figure 5.50 shows the XRD patterns of the  $\text{Eu}^{3+}$ -doped  $\text{Gd}_2\text{O}_3$  thin films, synthesized by sol-gel method/spin coating, and annealed at  $750^\circ\text{C}$  for 1 hour. These patterns evidenced the formation of highly oriented films. Only a very sharp peak corresponding to (400) plane of cubic  $\text{Gd}_2\text{O}_3$  phase (JCPDS card N<sup>o</sup> 12-0797) was observed for all Eu contents. The variation of average crystallite size of  $\text{Gd}_2\text{O}_3$  in films with 'x' values is shown in figure 5.51. Similar to nanopowders, we found no remarkable effect of  $\text{Eu}^{3+}$  content on the average crystallite size, which ranging between 19.4nm and 23.5nm, when 'x' rising from 0.00 to 0.30 w/w. This values of average crystallite size is in good agreement with results of H. Guo [9] for non oriented  $\text{Gd}_2\text{O}_3$  thin films (annealed at  $750^\circ\text{C}$  for 1 hour) synthesized by sol-gel process and dip-coating method from acetates precursors, using 2-methoxyhetanol as solvent and Diethanolamine as chelating agent. Figure 5.51 also suggests that the lattice parameter increases slightly with a rise in 'x' value.

The morphology of thin films produced was analyzed by optical microscopy. Figure 5.52 shows the micrographs of bare (a) and doped ( $x=0.08$ w/w)  $Gd_2O_3$  (b). A smooth and cracks free surface was observed at the magnification of the images. The thickness of thin films for all europium contents, as measured by profilometry, was  $(68.8 \pm 1.9)$  nm, and no appreciable effect of europium content was observed.

Figure 5.50 XRD patterns of the  $Eu^{3+}$ -doped  $Gd_2O_3$  thin films. Preferential orientation along (400) direction of cubic structure is observed for all 'x' values.

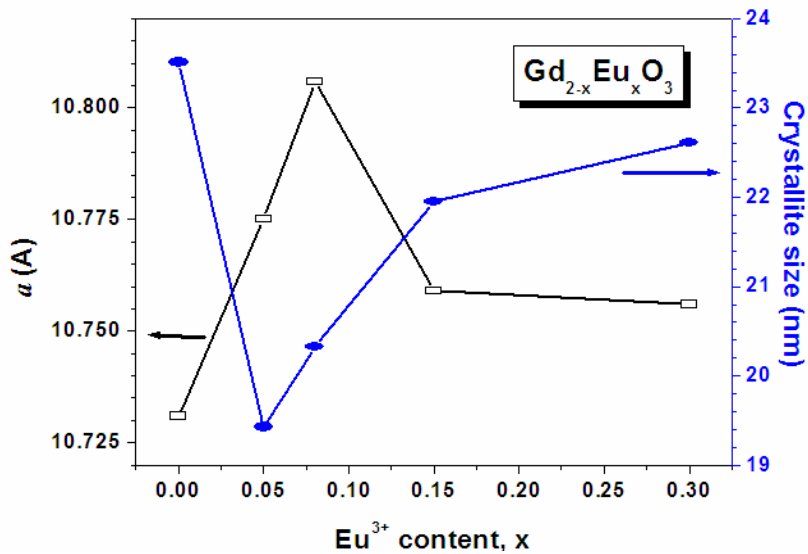


Figure 5.51 Lattice parameter and crystallite size as function of  $Eu^{3+}$  ions content ('x') of highly oriented thin films.

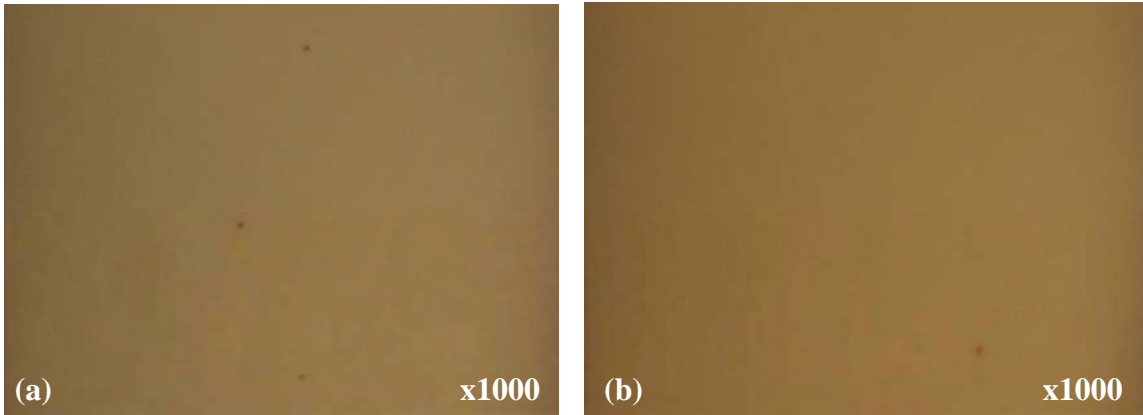


Figure 5.52 Optical micrographs of (a)  $Gd_2O_3$  and (b)  $Gd_{2-x}Eu_xO_3$  ( $x=0.08$ ) thin films grown onto fused quartz by sol-gel and spin coating, and annealed at  $750^\circ C$  for 1h.

#### 5.2.2.2 Optical properties

The absorbance and transmittance of  $Gd_{2-x}Eu_xO_3$  thin films were investigated by UV-vis spectroscopy. Figure 5.53 shows the absorption (a) and transmission (b) spectra of thin films synthesized at different 'x' values. As seen, all spectra were very similar independently of the Eu contents. Minimum absorption, i.e. transmittance above,  $>80\%$ , was observed in the visible region indicating the high transparency of the thin films within this region, which reveal that films are carbon free [94]. It is consistent with the SEM-EDS results (figure 5.42). In turn, a strong absorption in the UV region below 250nm is observed in both pure and  $Eu^{3+}$ -doped  $Gd_2O_3$  films independently of the  $Eu^{3+}$  ions concentration. This absorption band in the UV region is associated to  $Gd_2O_3$  hosts in agreement with previous results [93,95].

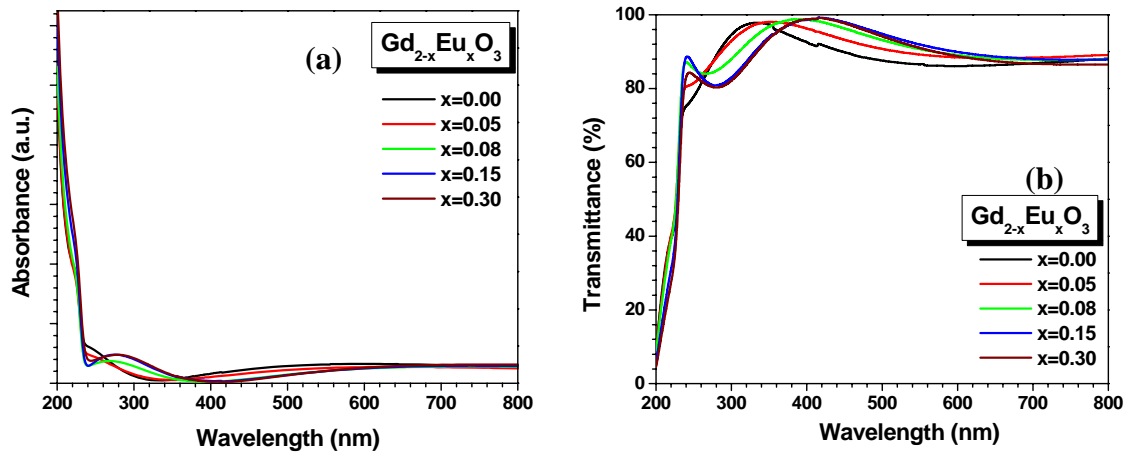


Figure 5.53 Absorption (a) and transmission (b) spectra of  $\text{Eu}^{3+}$ -doped  $\text{Gd}_2\text{O}_3$  thin films with different contents of  $\text{Eu}^{3+}$ , synthesized onto fused quartz.

Using the optical data, the corresponding values of the band gap energy were estimated by the equation (4.7), where  $n=1/2, 3/2, 2, 3$  depending upon the type of the electronic transitions. For allowed direct transitions  $n=1/2$  while  $n=3/2$  is used for forbidden direct transitions. The corresponding ‘ $n$ ’ values for the indirect transitions are 2 and 3, respectively. The range of validity for this equation is very small, which difficult the accurate determination of the exponent ‘ $n$ ’.

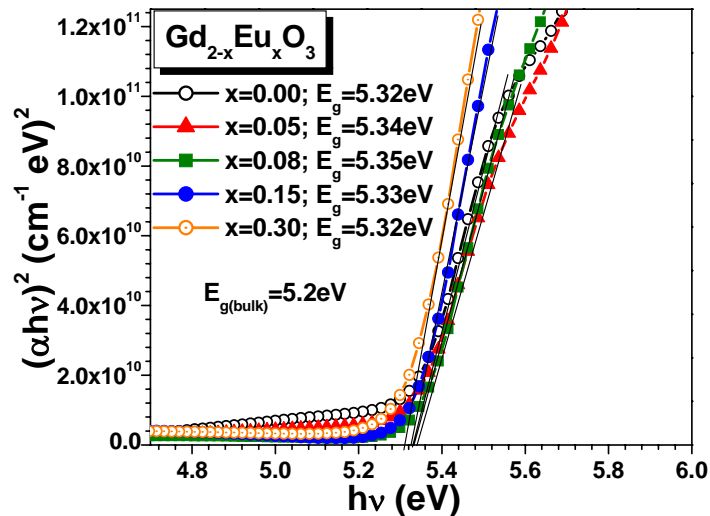


Figure 5.54 Absorption spectra, showing the band gap of  $\text{Eu}^{3+}$ -doped  $\text{Gd}_2\text{O}_3$  thin films. No appreciable effect of  $\text{Eu}^{3+}$  content is observed.

As known, the energy gap value will determine the threshold for the absorption of photons. In turn, the refractive index ( $n$ ) of a material is an indicator of its transparency to incident spectral radiation. Using the general theory of photoconductivity, based on the photo effect studies, Moss [96] proposed the following equation that correlates these two properties:

$$n^4 E_g = 95eV \quad (5.5)$$

According to this relation, the refractive index of the thin films synthesized in our work was estimated to be 2.1. This value is in good agreement with other works [9], and becomes to the thin films as potential waveguide and scintillation material.

### ***5.2.2.3 Photoluminescence measurements***

Figure 5.55 shows the shows the excitation spectra obtained when the 611nm line from  $\text{Eu}^{3+}$  ion was monitored in film samples prepared at different 'x' values. It can be seen that the excitation spectra consist of a strong band at about 229nm and the charge transfer band (CTB) from  $\text{O}^{2-}$  to  $\text{Eu}^{3+}$ . The intensity of the CTB increases with the  $\text{Eu}^{3+}$  content, a trend that was also observed in the nanocrystalline powders synthesized by the same method. The bands at 274nm and 312nm (related to internal  $\text{Gd}^{3+}$  transitions) and the bands of direct absorption of  $\text{Eu}^{3+}$  were weaker than that observed in nanocrystalline powders (see figures 5.43 and 5.44) for similar compositions. This fact indicate that the host  $\text{Gd}_2\text{O}_3$  is better sensitizer than  $\text{O}^{2-}$  and  $\text{Gd}^{3+}$ , which is in good agreement with previous reports [9,93]. As discussed, and based on UV-Vis measurements (figures 5.53

and 5.54), the band at 229nm can be assigned to absorption by Gd<sub>2</sub>O<sub>3</sub> host. The presence of the strong Gd<sub>2</sub>O<sub>3</sub> host band in the excitation spectra of Eu<sup>3+</sup> indicates that there exists an efficient energy transfer from Gd<sub>2</sub>O<sub>3</sub> host to the doped Eu<sup>3+</sup>.

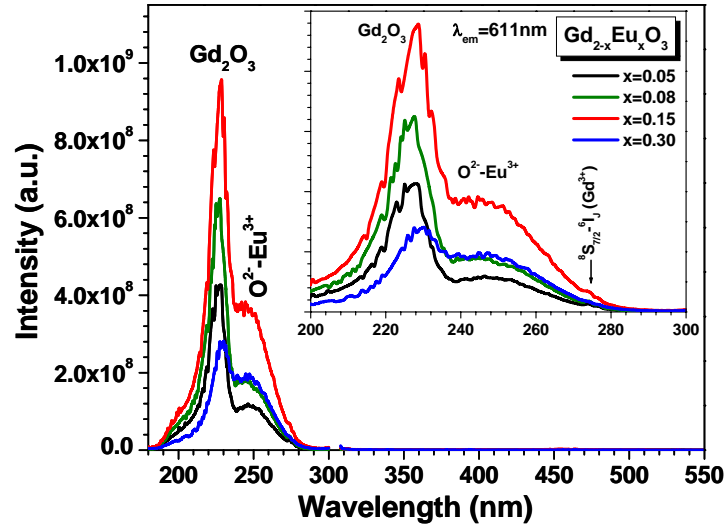


Figure 5.55 Excitation spectra of Gd<sub>2-x</sub>Eu<sub>x</sub>O<sub>3</sub> highly oriented thin films, with different content of Eu<sup>3+</sup> ions, and annealed at 750°C. The spectra were taken monitoring the 611nm emission line.

Figure 5.56 shows the effect emission spectra obtained for the Gd<sub>2-x</sub>Eu<sub>x</sub>O<sub>3</sub> (x=0.08) thin film, by using different wavelengths excitation. All emission bands correspond to typical intra shell <sup>5</sup>D<sub>0</sub>-<sup>7</sup>F<sub>J</sub> transitions of Eu<sup>3+</sup> ions, being the hypersensitive red emission <sup>5</sup>D<sub>0</sub>-<sup>7</sup>F<sub>2</sub> transition the predominant. The spectra also show that the Gd<sub>2</sub>O<sub>3</sub> absorption band excitation (229nm) produces the strongest and brightest red emission compared with the conventional direct excitation wavelength (393nm), inclusive superior to that obtained using CTB excitation. The spectra collected by exciting the film with Gd<sub>2</sub>O<sub>3</sub> host absorption band and CTB are shown in figure 5.57. The positions of the bands are in good agreement to those observed in nanocrystalline Gd<sub>2-x</sub>Eu<sub>x</sub>O<sub>3</sub> powders.

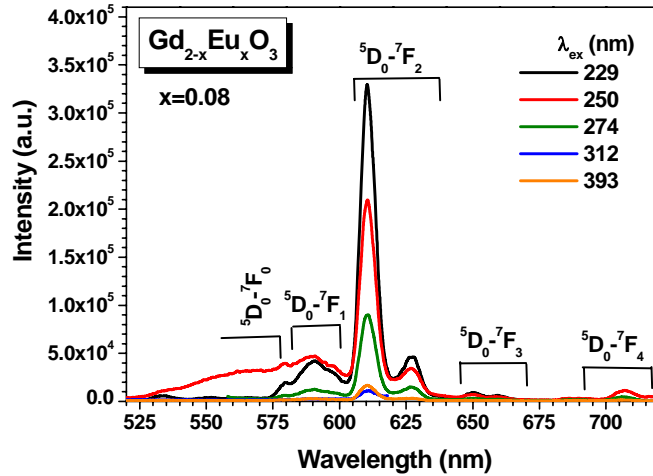


Figure 5.56 Effect of excitation wavelength on intensity of luminescence from  $^5D_0 \rightarrow ^7F_2$  transition of  $Gd_{2-x}Eu_xO_3$  thin films.

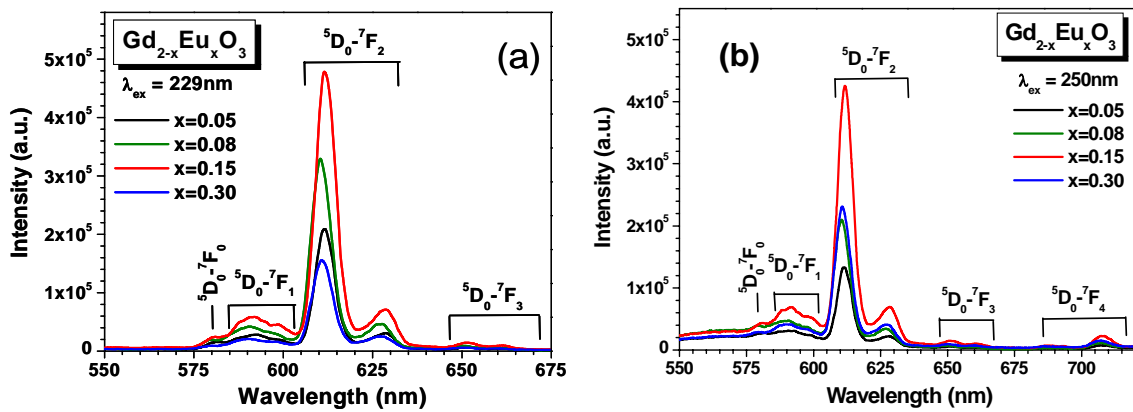


Figure 5.57 Emission spectra, at room temperature, of  $Gd_{2-x}Eu_xO_3$  highly oriented thin films, with different content of  $Eu^{3+}$  ions, and annealed at  $750^\circ C$ . The spectra were collected by using the 229 nm (a) and 250nm (b) excitation lines.

Similar to nanocrystalline powders, the luminescence of the thin films is strongly dependent of  $Eu^{3+}$  content, as shows figures 5.57 and 5.58. For each wavelength excitation (229nm and 250nm), the most intense luminescence was obtained in  $Gd_{2-x}Eu_xO_3$ , with  $x=0.15$ . Although the energy transfer has been verified, the quenching concentration phenomena also was observed for  $Eu^{3+}$  content higher than 0.15.

Figure 5.58 Relation of luminescence at 611nm and  $\text{Eu}^{3+}$  concentration for  $\text{Eu}^{3+}$ -doped  $\text{Gd}_2\text{O}_3$  highly oriented thin films annealed at 750°C.

From discussed results can be concluded that the suitable control of synthesis conditions allows obtain nanopowders and thin films highly crystalline, which sure a good luminescent performance. Although no quantum effects were observed, the effect of  $\text{Eu}^{3+}$  and annealing temperature on luminescence properties of both nanostructures (powders and thin films) was clearly defined. However, would be interesting optimizing these conditions to obtain smaller nanoparticles.

On the other hand, in the highly oriented thin films, with high transparence (>80%) in the visible region, the sensitization from host  $\text{Gd}_2\text{O}_3$  was the most effective in order to obtain the most intense red luminescence from the  $\text{Eu}^{3+}$ -doped  $\text{Gd}_2\text{O}_3$  films, which was different to nanoparticles were the most effective was through CTB. However, in both nanostructures, in contrast to  $\text{Eu}^{3+}$ -ZnO system, the energy transfer was clearly verified.

## CHAPTER VI: CONCLUSIONS AND SUGGESTIONS

The present research work was focused on the systematic study of the effect of the atomic fraction of  $\text{Eu}^{3+}$  ions and crystal size on the structural, optical absorption, luminescence and magnetic properties of two nanocrystalline hosts: ZnO (nanoparticles and nanocrystals) and  $\text{Gd}_2\text{O}_3$  (nanoparticles and thin films), by using different synthesis methods. From the results previously presented and discussed, it can be concluded that:

### On $\text{Eu}^{3+}$ - ZnO System: Nanopowders and Nanocrystals

- $\text{Eu}:\text{ZnO}$  nanocrystalline powders (7-11nm) were successfully synthesized by direct thermal decomposition of acetate precursors. Although the ZnO unit cell dimensions did not exhibit any distortion, no isolated crystalline Eu-compounds were detected by XRD for all evaluated Eu concentrations.
- XRD and PL measurements suggested the no-incorporation of Eu dopants into the ZnO lattice. The difference of thermal behavior of the precursors should be related with this behavior.  $\text{Eu}^{3+}$  ions would be present as poorly crystalline phase coexisting with well-crystallized ZnO crystals.
- $\text{Eu}:\text{ZnO}$  nanopowders did not exhibit luminescence in the visible region (*solvent effect*). This material can find applications in optoelectronic systems.
- Nanocrystals of ZnO, were successfully synthesized in presence of  $\text{Eu}^{3+}$  ions through a modified sol-gel method (ethanol route) at room-temperature.

- XRD data evidenced the drop in average crystallite size with a rising concentration of  $\text{Eu}^{3+}$  ions, which should have enhanced the stability of the intermediate compound (basic zinc acetate) retarding the atomic rearrangement and dehydration conducive to the ZnO structure.
- Raman, UV-Vis y PL measurements also suggested the inhibiting effect of Eu ions on the crystallinity and crystal size of ZnO nanocrystals.
- The enhancement of visible luminescence in ZnO nanocrystals suggests the presence of lattice defects (oxygen traps, interstitials) in ZnO nanocrystals.

### **On $\text{Eu}^{3+}$ - $\text{Gd}_2\text{O}_3$ System: Nanoparticles and Thin Films**

- Highly crystalline cubic  $\text{Eu}^{3+}$ -doped  $\text{Gd}_2\text{O}_3$  phosphors were successfully synthesized by thermal decomposition of acetate precursors. The average particle size varied from 29nm up to 41nm when the annealing temperature varied from 750°C to 950°C. The  $\text{Eu}^{3+}$  concentration in the Gd-oxide host did not affect the corresponding crystallite sizes.
- PL excitation spectra (at 250nm) verified the red emission, corresponding to  $^5\text{D}_0 \rightarrow ^7\text{F}_1$  transitions, and the efficient energy transfer from host to  $\text{Eu}^{3+}$  ions.
- The highest PL intensity was achieved at the Eu atomic fraction of 0.15 (7.5% w/w). Higher concentrations of dopants caused the quenching of the PL. This quenching was attributed to exchange interactions between  $\text{Eu}^{3+}$  ions incorporated in the host.

- $\text{Eu}^{3+}$ -doped  $\text{Gd}_2\text{O}_3$  nanopowders exhibited paramagnetism at room-temperature. The magnetic susceptibility decreased as the  $\text{Eu}^{3+}$  content increased. This behavior can be explained by the exchange of a magnetic species ( $\text{Gd}^{3+}$  ions) by a non-magnetic one (Eu species).
- Highly crystalline 68nm-thick (400) oriented thin films of  $\text{Gd}_{2-x}\text{Eu}_x\text{O}_3$ ,  $x= 0.1-0.3$ , were successfully growth by sol-gel and spin-coating processing. The films showed high transparency in the visible region.
- Unlike to nanoparticles, the more efficient excitation to obtain red luminescence was that corresponding to the absorption band of the host  $\text{Gd}_2\text{O}_3$  (229nm). Again, the energy transfer from host to Eu ions was confirmed.
- From the results found in this work, it is suggested the following:
  - Study of the nanostructures of  $\text{Zn}_{1-x}\text{O}:\text{Eu}_x$ , in order to clarify the absence of defects and verify the occupation place of  $\text{Eu}^{3+}$  ions.
  - Complete the study on the magnetic behavior of  $\text{Eu}^{3+}$ -doped  $\text{Gd}_2\text{O}_3$  nanopowders and thin films.
  - To explore the possibility of synthesizing core-shell  $\text{Fe}_3\text{O}_4/\text{Eu}^{3+}$ -doped  $\text{Gd}_2\text{O}_3$  nanoparticles in order to use their both magnetic and luminescence properties in biomedical applications.

## REFERENCES

- 1- B.M. Tissue, Chem. Mater. **10** (1998) 2837-2845
- 2- Z.L.Wang, Materials Today, June 2004 26-33
- 3- A. Yamamoto, *et al.*, J. Cryst. Growth **214-215** (2000) 308-311
- 4- R.D. Shannon, Acta Cryst. **A32** (1976) 751-767
- 5- A. Ishizumi and Y. Kanemitsu, Appl. Phys. Lett. **86** (2005) 253106
- 6- L.L. Zhang, *et al.*, Chin. Phys. Lett. **22**(5) (2005) 1225-1227
- 7- Y. Liu, *et al.*, Opt. Lett. **32**(5) (2007) 566-568
- 8- C. Boulesteix, *Defects and Phase Transformation Near Room Temperature in Rare Earth Sesquioxides*, in K.A. Gschneider, Jr. and L. Eyring (Eds.) Handbook on the Physics and Chemistry of Rare Earths, (1982) Vol. 5, Chap. 44, pp. 321-386. North-Holland Publishing Company, Amsterdam
- 9- H. Guo, *et al.*, Appl. Surf. Sci. **230** (2004) 215-221
- 10- W.O. Gordon, *et al.*, J. Lumin. **108** (2004) 339- 342
- 11- C. Görller-Walrand and K. Binnemans, *Spectral Intensities of f-f Transitions*, in K.A. Gschneider, Jr. and L. Eyring (Eds.) Handbook on the Physics and Chemistry of Rare Earths, Vol. 25, Chap. 167, 101-264. Elsevier, Amsterdam (1998)
- 12- M. H. V. Werts, Science Prog. **88**(2) (2005) 101-131
- 13- C.C. Berry and A.S.G. Curtis, J. Phys. D: Appl. Phys. **36** (2003) R198-R206
- 14- M. Nichkova, *et al.* Anal. Bichem. **369** (2007) 34-40
- 15- A.A. Bol, *et al.*, Chem. Mater. **14** (2002) 1121-1126
- 16- B. Mercier, *et al.*, J. Lum. **119-120** (2006) 224-227
- 17- B. Mercier, *et al.*, J. Lumin. **122-123** (2007) 756-758

- 18- G. Liu, *et al.*, J. Alloys Comp. **432** (2007) 200-204
- 19- A.M. Pires, *et al.*, J. Alloys Comp. **344** (2002) 276-279
- 20- H. Chen, *et al.*, J. Colloid Interface Sci. **273** (2004) 191
- 21- Ch. Liu, *et al.*, J. Lumin. **122-123** (2007) 80-82
- 22- E.M. Goldys, *et al.*, J. Am. Chem. Soc. **128** (2006) 14498-14505
- 23- C. Louis, *et al.*, J. Solid State Chem. **173** (2003) 335-341
- 24- Ch.-Ch. Lin, K.-M. Lin and Y.-Y. Li, J. Lumin. **126** (2007) 795-799
- 25- S. Shionoya and W.M. Yen, *Phosphor Handbook*, CRC Press, Boca Raton, Florida 1999.
- 26- G. Blasse, *Chemistry and physics of R-activated phosphors*, in: L.R. Eyring (Ed.), *Handbook on the Physics and Chemistry of Rare Earths*, (1979) Vol. 4, Chap. 34, pp. 237–274. North-Holland Publishing Company, Amsterdam.
- 27- U. Özgür, *et al.*, J. Appl. Phys. **98** (2005) 041301
- 28- I. Ivanov and J. Pollmann, Phys. Rev. B **24**(12) (1981) 7275-7296
- 29- J.E. Jafee and A.C. Hess, Phys. Rev. B **48**(11) (1993-I) 7903-7909
- 30- L. Pauling, “*The Nature of the Chemical Bond*”, Cornell University Press, Ithaca, New York, (1960)
- 31- A.F. Kohan, G. Ceder and D. Morgan, Phys. Rev. B **61**(22) (2000-II) 15019-15027
- 32- A. Mang, *et al.*, Solid State Commun. **94**(4) (1995) 251-254
- 33- W.R.L. Lambrecht, Phys. Rev. B **65** (2002) 075207
- 34- M. Cardona, Phys. Rev. **129** (1963) 69
- 35- D.C. Reynolds, *et al.*, Phys. Rev. B **60**(4) (1999-II) 2340-2344
- 36- D. G. Thomas, J. Phys. Chem. Solids **15** (1960) 86-96

- 37- S.A.M. Lima, *et al.*, Int J. Inorg. Mater. **3**(7) (2001) 749–754
- 38- D. Li, *et al.*, Appl. Phys. Lett. **85**(9) (2004) 1601-1603
- 39- A.B. Djurišić, *et al.*, Nanotechnology **18** (2007) 095702
- 40- A. Janotti and C.G. van de Walle, Phys. Rev. B **76** (2007) 165202
- 41- R. Dingle, Phys. Rev. Lett. **23**(11) (1969) 579-581
- 42- N.Y. Garces, *et al.*, Appl. Phys. Lett. **81**(4) (2002) 622-624
- 43- V.A.L. Roy, *et al.*, Appl. Phys. Lett. **83**(1) (2003) 141-143
- 44- Y.G. Wang, *et al.*, J. Appl. Phys. **94**(1) (2003) 354-358
- 45- K. Vanheusden, *et al.*, J. Appl. Phys. **79**(10) (1996) 7983-7990
- 46- A. van Dijken, *et al.*, J. Phys. Chem. B **104** (2000) 1715-1723
- 47- A. van Dijken, *et al.*, J. Lumin. **90** (2000) 123-128
- 48- D.C. Reynolds, *et al.*, Solid State Commun. **101**(9) (1997) 643-646
- 49- D.C. Reynolds, *et al.*, J. Appl. Phys. **89**(11) (2001) 6189-6191
- 50- B. Lin, Z. Fu and Y. Jia, Appl. Phys. Lett. **79**(7) (2001) 943-945
- 51- Z. Wang, *et al.*, Physica E **35** (2006) 199-202
- 52- J. Jensen and A.R. Mackintosh, *Rare Earth Magnetism. Structures and excitations*, Clarendon Press, Oxford, 1991
- 53- G.S. Ofelt, J. Chem. Phys. **37**(3) (1962) 511-520
- 54- H.E. Hoefdraad, J. Solid State Chem. **15** (1975) 175-177
- 55- C. Liu, J. Liu and K.Dou, J. Phys. Chem. B **110** (2006) 20277-20281
- 56- P. Derembos, J. Phys.: Condens. Matter. **15** (2003) 8417-8434
- 57- A. Ubaldini, M.M. Carnasciali, J. Alloys Compd. (2007), doi:10.1016/J.Jallcom.2006.12.067

- 58- R.M. Moon and W.C. Koehler, *Phys. Rev. B* **11**(4) (1975) 1609-1622
- 59- C.R. Stanek, *et al.*, *Phys. Rev. B* **75** (2007) 134101
- 60- L.E. Brus, *J. Chem. Phys.* **80** (1984) 4403
- 61- E. Antic-Fidancev, *et al.*, *J. Phys.: Condens. Mater.* **15** (2003) 863-876
- 62- C. Liu and J. Liu, *J. Phys. Chem. B* **110** (2006) 20277-20281
- 63- M. Buijs, A. Meyerink and G. Blasse, *J. Lumin.* **37** (1987) 9-20
- 64- Ch.Xuenyuan, *et al.*, *J. Rare Earths* **25** (2007) 515-525
- 65- S.A.M. Lima, *et al.*, *J Alloys Comp.* **344** (2002) 280-284
- 66- Ch.-S. Park, *et al.*, *J. Lumin.* **118** (2006) 199-204
- 67- Y.C. Kang *et al.*, *J. Phys. Chem. Solids* **60** (1999) 379-384
- 68- A. Garcia-Murillo, *et al.*, *Opt. Mater.* **19** (2002) 161-168
- 69- L.Spanhel and M.A. Anderson *J. Am. Chem. Soc.* **113** (1991) 2826-2833
- 70- A. Parra, Msc. Thesis, University of Puerto Rico at Mayaguez, 2006
- 71- B.D. Cullity and S.R. Stock, *Elements of X-ray diffraction*, third edition, Prentice Hall, New Jersey (2001)
- 72- K. Brandenburg and H. Putz, Match! Phase identification from powder diffraction, crystal Impact (2003-2006) Postfach 12 51, D-53002 Bonn Germany
- 73- C.A. Arguello, *et al.*, *Phys. Rev.* **181**(3) (1969) 1351-1363
- 74- T.C. Damen, S.P.S. Porto and B. Tell *Phys. Rev.* **142** (1966) 570
- 75- K.G. Kanade, *et al.*, *Mat. Res. Bull.* **41** (2006) 590-600
- 76- X. Wang, *et al.*, *Appl. Phys. Lett.* **84**(24) (2004) 4941-4943
- 77- H.-M. Cheng, *et al.*, *J. Cryst. Growth* **277** (2005) 192-199
- 78- S.S. Ashtaputre, *et al.*, *J. Phys. D: Appl. Phys.*, **41** (2008) 015301

- 79- S. Gao, *et al.*, Appl. Phys. Lett. **89** (2006) 123125
- 80- G.H. Schoenmakers, *et al.*, J. Phys. Chem. **100** (1996) 3210-3220
- 81- W. Chen, *et al.*, J. Chem Phys. B **108** (2004) 11927-11934
- 82- M. Urban, *et al.*, J. Phys. Chem. Solids **48** (5) (1987) 475-479
- 83- N. Deliwar, *et al.*, Mater Charact (2007), doi : 10.1016/j.matchar.2007.04008
- 84- V. Pelova, *et al.*, Cryst. Res. Technol. **33** (1998) 125
- 85- P. Sharma, R. Nass and H. Schmidt, Opt. Mater. **10** (1998) 161-169
- 86- X. Gong, *et al.*, J. Phys. Chem. Solids, **61** (2001) 115-121
- 87- Y. Li and G. Hong, J. Lumin. **124** (2007) 297-301
- 88- D. Wang, *et al.*, J. Lumin. **97** (2002) 1-6
- 89- A. Son, *et al.*, Anal. Biochem. **370** (2007) 186-194
- 90- A. Grill and M. Schieber, Phys. Rev. B **1** (5) (1970) 2241-2242
- 91- R.M. Moon, *et al.*, Phys. Rev. B **5** (3) (1972) 997
- 92- L. Lou, *et al.*, Opt. Mater. **18** (2001) 331-336
- 93- M.L. Pang, *et al.*, Opt. Mater. **23** (2003) 547-558
- 94- M.P. Singh, *et al.*, Mater. Chem. Phys. **110** (2008) 337-343
- 95- N.K. Sahoo, *et al.*, Thin Solid Films **440** (2003) 155-168
- 96- T.S. Moss, Phys. Stat. Sol. (b) **131** (1985) 415